Impacts of Atmospheric Waves on Tropical Convection and the Tropical Tropopause Layer

by

Ji-Eun Kim

B.S., Ajou University, 2002

M.S., Korea Advanced Institute of Science and Technology, 2004

A thesis submitted to the
Faculty of the Graduate School of the
University of Colorado in partial fulfillment
of the requirements for the degree of
Doctor of Philosophy
Department of Atmospheric and Oceanic Sciences
2015

This thesis entitled:
Impacts of Atmospheric Waves on Tropical Convection and the Tropical Tropopause Layer
written by Ji-Eun Kim
has been approved for the Department of Atmospheric and Oceanic Sciences

Dr. M. Joan Alexander

Dr. Jeffrey B. Weiss

Date ____________________

The final copy of this thesis has been examined by the signatories, and we find that both the content and the form meet acceptable presentation standards of scholarly work in the above mentioned discipline.

Kim, Ji-Eun (Ph.D., Atmospheric Sciences)

Impacts of Atmospheric Waves on Tropical Convection and the Tropical Tropopause Layer

Thesis directed by Dr. M. Joan Alexander

Atmospheric equatorial waves play vital roles in tropical weather and climate. Tropical convective systems are often organized by waves, and at the same time convection itself generates a broad spectrum of waves propagating horizontally and vertically. Equatorial waves propagating into the stratosphere control the quasi-biennual oscillation (QBO) of equatorial stratospheric winds and are partially responsible for tropical upwelling as a part of the stratospheric Brewer-Dobson circulation. Waves in the tropical tropopause layer (TTL) affect dehydration of air entering the lower stratosphere by the formation of cirrus clouds, having significant radiative impacts on surface climate.

This thesis aims to provide an improved understanding of roles of equatorial waves on tropical convection and interaction processes between the troposphere and stratosphere. First, tropical precipitation characteristics associated with equatorial waves are studied using the TRMM satellite estimates and five reanalyses for the period of 2005-2007. Next, waves in the TTL are examined using temperatures in radiosondes and two reanalyses, ERA-interim and MERRA. Based on the results of variance difference between observations and reanalyses, we have developed a new wave parameterization scheme for simulations of the dehydration process in the TTL. We have found that, even though the mean temperature is the same, having stronger waves lowers cold-point tropopause temperatures. This finding has led to an extended, comprehensive study of this relation using historical radiosonde data. Temperatures from 23-year observations of radiosondes in the western Pacific show that a broad spectrum of waves is responsible for lowering tropopause temperature. Moreover, the wave impact on the tropopause has decadal scale variations, suggesting changes in wave activity in the TTL have important implications for cirrus clouds and stratospheric water vapor. Lastly, aircraft measurements of meteorological fields and tracers have revealed that the tracer transport is highly correlated with a fine vertical wave structure in the TTL whose scale is unresolvable in current analysis and climate models due to limited vertical resolution.

Dedication

To Joongoo & Joo-Eon, Seoksoon & Silkyung, and Sanghee & Yi-Yeon

Acknowledgements

This may sound silly. But since the beginning of my PhD study, I have wondered how I will write my thesis acknowledgements. Would I have many people to thank? Would I regret or be satisfied when I graduate? Sometimes I felt like I worried more about acknowledgements than about my thesis itself. It turned out that my PhD years have been far more awesome than I thought it would be. I loved to learn, work, and meet wonderful people.

First of all, I would like to give many thanks to my thesis advisor, Dr. M. Joan Alexander, for all her supports and opportunities she has provided. I am truly grateful for her teaching, wisdom, and help throughout the PhD years. I remember our very first meeting. I said to her something like, "To me, doing research is like playing Lego. We can make a nice story out of many small Lego pieces." Looking back my PhD journey with her, I would like to say that it was so fun to play Lego with her. She encouraged me when I was depressed, guided me when I was lost, and pushed me when I got lazy, but still she gave me enough freedom so that I could learn the joy of being a scientist.

I would like to thank my dissertation committee members, Jeffrey Weiss, Brian Toon, Rajagopalan Balaji, and Julio Bacmeister for their time and guidance for my thesis. My gratitude also goes to all professors who taught me at the university. I truly enjoyed every single lecture given by them. I thank our cheerful department staff Laurie Conway for responding promptly to any questions and requests about everything from admission to graduation.

My PhD work is supported by NASA's ATTREX mission. I would like to thank all the ATTREX team members for their hard work for successful measurements in difficult conditions. I

specially thank Eric Jensen and Lenny Pfister for giving me the opportunity to participate in the project. Their encouragement on my work meant a lot to me. It was my honor and pleasure to work with them.

During my PhD, I have attended NCAR ACD UTLS group seminars. I thank the meeting organizers Steve Massie, Laura Pan, and Bill Randel as well as all old and current members of the "donut" meeting. From all the talks and discussions, I have learned so many things that I cannot gain by reading books or journals. Also, I was impressed by their lighthearted but passionate mind toward science.

I thank NWRA/CoRA scientists and visitors. They made my time at NWRA/CoRA more enjoyable. I thank Janet Biggs, Andy Frahm, and Orion Poplawski for their administrative and computer supports.

The most valuable thing I have gained throughout my PhD study is not the degree or scientific knowledge and skills. I was very lucky to make good friends. My warm heart goes to Rei Ueyama, Johnny Luo, Tao Wang, Joowan Kim, and Stephan Fueglistaler. I am excited to share our knowledge and friendship in coming decades with these young and relatively young scientists.

I thank Jeff Williams who was my English tutor. He helped me to have confidence in speaking with people. I enjoyed our conversation sessions, and he became my dear friend and counselor.

Living as a foreigner would have been harder without Korean families around me. Especially I was lucky to have Eunsun's family next door. I deeply love my church friends and their adorable kids. My special thanks must go to Mi Jeong, Sunmin, Inha, and their families. They became like my family. They have been a big support for me and my family. Their kids brought me enormous pleasure and happiness. Seriously, they are irresistibly cute!

I am fortunate to have such great parents and in-laws. They have always supported and encouraged me to pursue my degree even though my study meant that they can hardly see their loving daughter. I thank my parents Seoksoon and Silkyung who gave me a heart to endure hardships and to appreciate what have been given to my life. I thank my parents in law Sanghee and Yi-Yeon for gladly flying all the way from Korea to here to take care of my son Joo-Eon when

I was away for field missions and conferences. I am also grateful that I have my brother Woonhak and his family. Having a brother like him makes my life brighter.

My husband Joongoo should be proud of himself for keeping his promise to my parents upon our marriage that he will make me Dr. Kim someday. He indeed brought me to Colorado and introduced “my PhD cloud” to me. In one late afternoon, he shouted to me, “Ji-Eun! Look at the sky!” A huge, white convective cumulus congestus cloud was developing rapidly in the blue Colorado sky, and that cloud mesmerized me and motivated my desire to learn about nature. Joongoo’s companionship, support, encouragement, and advice were essential to complete the degree.

Although there were some tough times, there were so many good things during the PhD years; I liked learning new things, doing research, going to conferences and field campaign deployments, and meeting many people and making friends. I should confess, however, that all my excitements filled with new experiences needed to consume my time and energy that could have been given to my boy. Yes, that was so many hours and days that I needed to spend to get the degree. I thank Joo-Eon for understanding this, and for still loving the busy mom. He is the best son ever!

Contents

Chapter

Tables

Table

Figures

Figure

Chapter 1

Introduction

Tropical waves are actively involved in interaction processes between the troposphere and stratosphere, as well as in tropospheric weather directly. Although the troposphere and stratosphere have very distinct features above and below the tropopause, waves generated in the troposphere can propagate vertically through the tropical tropopause layer (TTL) (Figure 1.1). These waves control the quasi-biennial oscillation (QBO) of stratospheric zonal wind and the large-scale stratospheric meridional transport circulation known as the Brewer-Dobson circulation. Changes in the stratospheric wind and the large-scale ascent in the tropics by the Brewer-Dobson circulation modulate the distribution of atmospheric constituents such as ozone and water vapor, regulating tropospheric temperature through radiation. Equatorial waves in the TTL also affect dehydration of air entering the lower stratosphere by the formation of cirrus clouds, which themselves have a considerable impact on the radiation budget. In addition to waves propagating upward, equatorial waves in the troposphere organize convection, which is itself a main source of a broad spectrum of waves. Due to such significant impacts of equatorial waves, it is of interest to understand the sources, propagation characteristics, and the roles of these waves on climate.

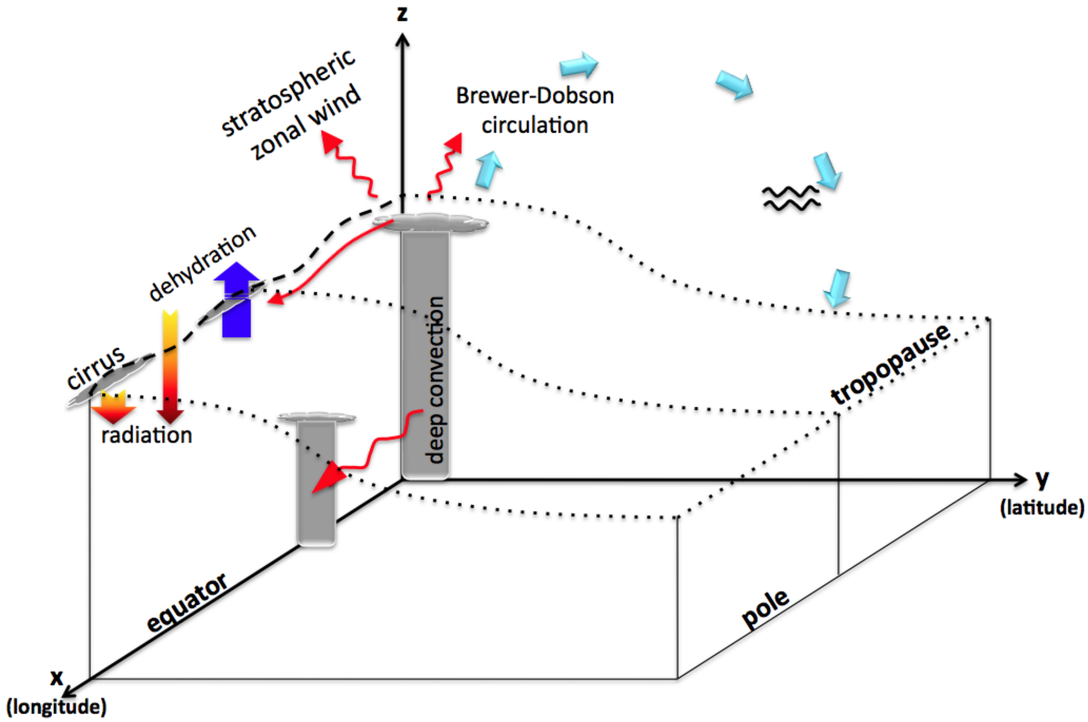

Figure 1.1: Schematic diagram of impacts of equatorial waves on weather and climate. The x-axis and y-axis are the zonal and meridional direction, respectively. The dotted lines represent the tropopause layer. Red arrows depict waves generated by tropical convection. Waves are coupled with moist convection in the troposphere. Waves propagating into the equatorial stratosphere interact with zonal wind, inducing the quasi-biennial oscillation (QBO) of the equatorial stratospheric zonal mean wind. Equatorial waves are also partially responsible for driving tropical upwelling as a tropical part of a large-scale stratospheric circulation called the Brewer-Dobson circulation (shown with series of light blue arrows). The doubled black lines indicate the extratropical wave forcing for the Brewer-Dobson circulation. Waves in the tropical tropopause layer (TTL) modulate temperature, affecting cirrus cloud formation and water vapor transport into the lower stratosphere. Clouds in the TTL and stratospheric water vapor have radiative impacts on surface climate mainly by longwave (infrared) radiation.

1.1 Convectively coupled equatorial waves

Tropical convection plays a vital role in global climate by driving large-scale circulation, releasing latent heat, modulating radiative forcing, and most importantly redistributing water in the earth system. Due to complex interactions of moist convection with dynamical, thermodynamical, and cloud processes, it is difficult to fully understand the tropical precipitation system. Over the past few decades, global observations with the advent of satellites have enabled better understanding of how tropical convection is organized and evolves. Studies about cloudiness and precipitation have revealed that tropical convective systems are often organized by equatorial waves, rather than initiated randomly (Wheeler and Kiladis, 1999; Cho et al., 2004). The equatorial waves trigger moist convection, and at the same time the tropical convection itself generates waves that propagate horizontally and vertically. These intriguing inter-dynamical responses between convection and equatorial waves occur at broad temporal and spatial scales ranging from the mesoscale to the planetary scale.

The pronounced spectral peaks in the observed equatorial waves correspond to the predicted dispersion curves (Wheeler and Kiladis, 1999), solutions of the shallow water equations on the equatorial beta plane (Matsuno, 1966) (See Figures 1.2, 1.3). As mathematically derived by Matsuno, observations have confirmed the existence of equatorial waves such as the Kelvin, mixed Rossby-Gravity (MRG), equatorial Rossby, and inertial gravity (IG) waves (Kiladis et al., 2009). In addition to these waves, the Madden-Julian Oscillation (MJO) (Madden and Julian, 1971, 1972) and tropical depression (TD)-type waves (Takayabu and Nitta, 1993) also have significant impact on tropical weather and climate by coupling with convection. The MJO is the eastward propagating convective envelope, dominating intraseasonal (30-90 days) variability with the speed of about 5 m s^{-1} (Zhang, 2005). Within the active phase of the MJO, a broad spectrum of cloud clusters coupled with waves has been identified. The tropical depression (TD)-type waves, also known as easterly waves, are westward propagating synoptic scale disturbances along the Intertropical Convergence Zone (ITCZ) with periods of 2-6 days–predominantly 3-6 days–and speeds of 5-10 m s^{-1} (Frank and Roundy, 2006; Kiladis et al., 2006; Dickinson and Molinari, 2002). This type of wave is very important for the formation of tropical cyclones (Frank and Roundy, 2006).

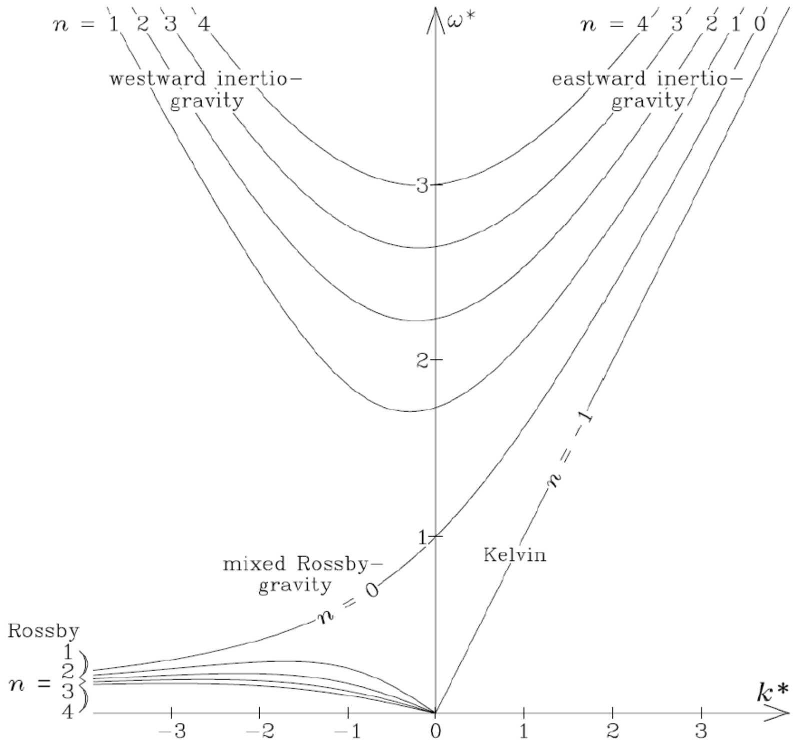

Figure 1.2: Dispersion curves for equatorial waves (up to $n = 4$) as a function of the nondimensional frequency, ω^*, and nondimensional zonal wavenumber, k^*, where $\omega^* \equiv \omega/(\beta\sqrt{gh_e})^{1/2}$, and $k^* \equiv k(\sqrt{gh_e}/\beta)^{1/2}$. Here g is the gravitational acceleration, h_e is the depth of the undisturbed layer of fluid, and n is the meridional mode number. In the shallow water equations, the Coriolis parameter is proportional to distance from the equator with the linear coefficient, β. For all but the Kelvin wave, these dispersion curves are solutions of the shallow water equations on the equatorial beta plane (Matsuno 1966). Westward propagating waves (relative to the zero basic state) appear on the left, and eastward propagating waves appear on the right. The Kelvin wave solution is labeled as $n = -1$. From Kiladis et al. (2009).

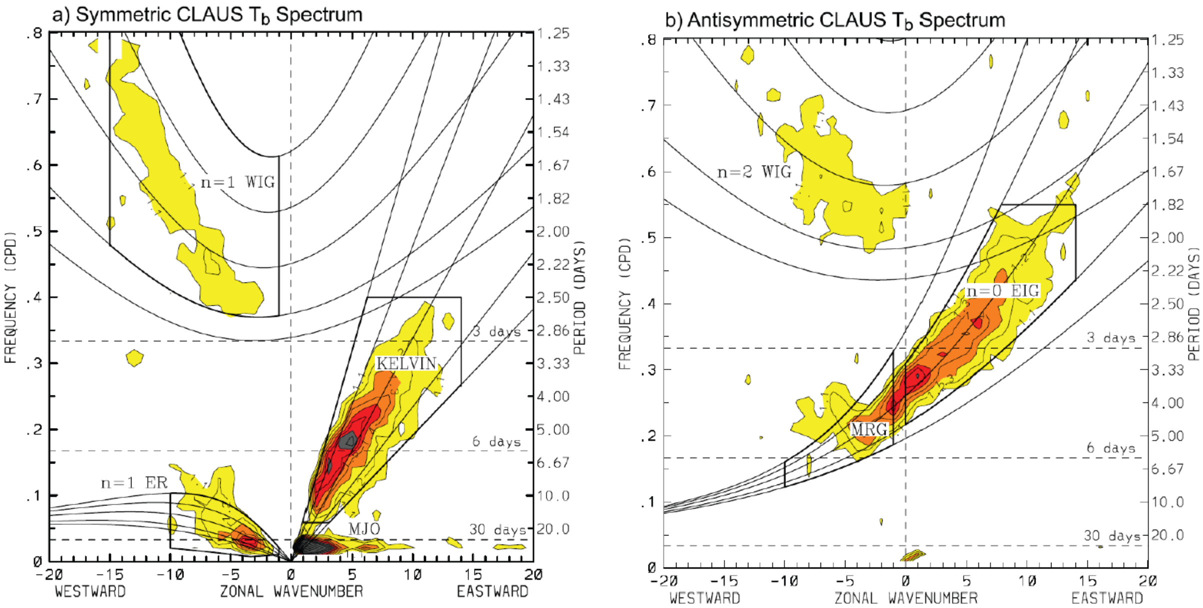

Figure 1.3: Wavenumber-frequency power spectrum of the (a) symmetric and (b) antisymmetric component of Cloud Archive User Services (CLAUS) T_b for July 1983 to June 2005, summed from 15°N to 15°S, plotted as the ratio between raw T_b power and the power in a smoothed red noise background spectrum (see Wheeler and Kiladis (1999) for details). Contour interval is 0.1, and contours and shading begin at 1.1, where the signal is significant at greater than the 95% level. Dispersion curves for the Kelvin, $n = 1$ equatorial Rossby, $n = 1$ and $n = 2$ westward inertial gravity, $n = 0$ eastward inertial gravity, and mixed Rossby-gravity waves are plotted for equivalent depths of 8, 12, 25, 50, and 90 m. From (Kiladis et al., 2009).

1.2 Waves in the stratosphere

In addition to direct impacts of convectively coupled equatorial waves (CCEWs) on tropical weather, indirect effects of convection are also significant for the tropical middle atmosphere and global climate. Observational studies of meteorological variables have discovered the existence of equatorial waves in the stratosphere (Wallace and Kousky, 1968; Yanai and Maruyama, 1966). These waves are called dry or free waves because, although they are generated by latent heating due to tropospheric moist convection, they are no longer coupled with convection as they propagate into the upper atmosphere (Holton and Lindzen, 1972). More vertically propagating waves are preferentially excited by small and transient scale convection (Alexander and Holton, 2004). The prime example of the dry wave impacts is the forcing of the stratospheric quasi-biennial oscillation (QBO), which is a quasi-periodic downward propagation of easterly and westerly zonal flows (Baldwin et al., 2001) as shown in Figure 1.4. By depositing easterly and westerly momentum in the stratosphere, vertically propagating waves modulate the background zonal wind (Alexander and Holton, 1997; Kawatani et al., 2010; Lindzen and Holton, 1968). Also, the tropical waves are partially responsible for driving the global-scale stratospheric transport circulation, called the Brewer-Dobson circulation. Redistribution of important chemical constituents such as ozone and water vapor by this circulation modulates the tropospheric and stratospheric climate (Forster and Shine, 2002; Hegglin and Shepherd, 2009; Solomon et al., 2010).

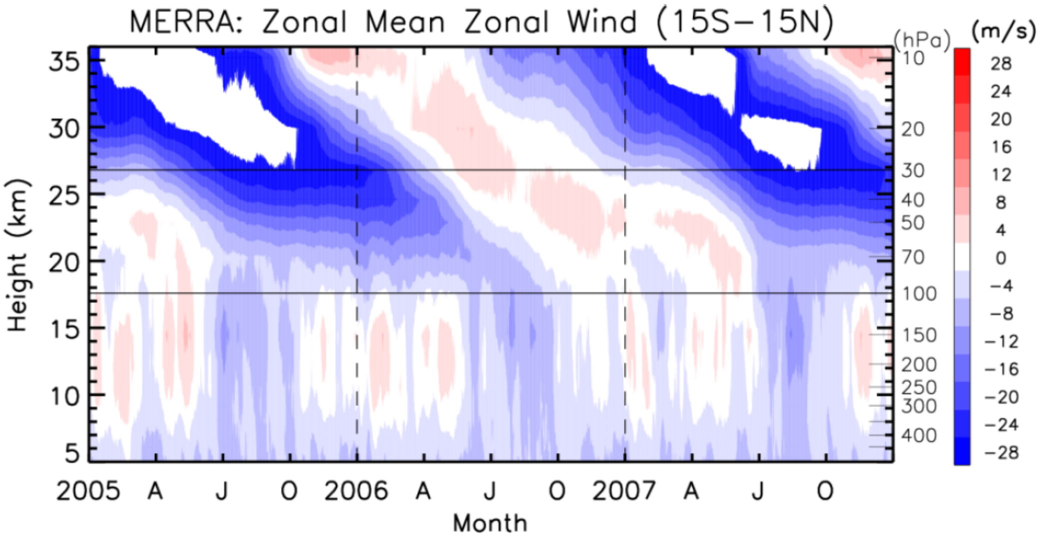

Figure 1.4: Zonal mean zonal wind averaged over 15°S-15°N for 2005-2007 from MERRA reanalysis

1.3 Waves in the tropical tropopause layer

The TTL is a transition layer between the tropical troposphere and stratosphere, vertically extending about 14 km to 18.5 km and laterally bounded by the position of the subtropical jets (Fueglistaler et al., 2009). The vertical temperature structure between the troposphere and stratosphere has a minimum in the TTL as shown in Figure 1.5. Air slowly ascends in the TTL due to radiative heating, and eventually this air is transported into the global stratosphere by a large-scale stratospheric circulation called the Brewer-Dobson circulation (See Figure 1.6.). For this reason, the TTL can be called a gateway of air from the troposphere to the stratosphere. When air passes through this gateway to the stratosphere, cloud formation and subsequent washout of soluble species due to cold temperature filter out many important atmospheric constituents such as water vapor and very short-lived substances (Brewer, 1949; Fueglistaler et al., 2009; WMO, 2011; Levine et al., 2007; Aschmann et al., 2009; Sinnhuber and Folkins, 2006). These gases have important impacts on stratospheric chemistry and radiation by affecting ozone abundances (Solomon et al., 1986; Dvortsov and Solomon, 2001). Furthermore, stratospheric water vapor itself has significant influences on surface climate (Forster and Shine, 1999, 2002; Dessler et al., 2013; Solomon et al., 2010).

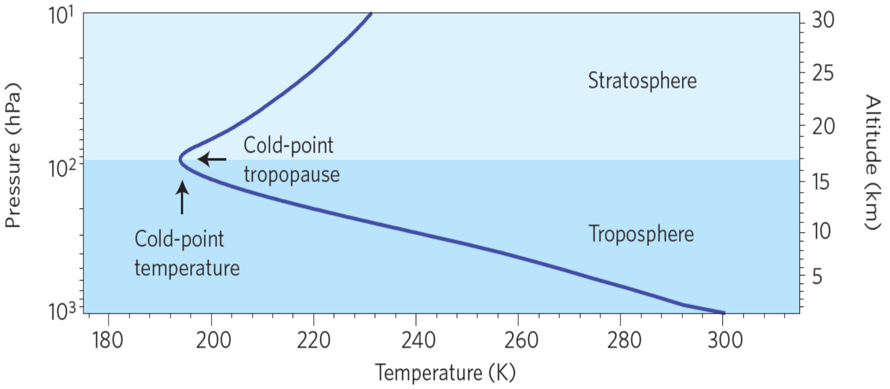

Figure 1.5: Vertical temperature profile in the troposphere and stratosphere. From Fu (2013).

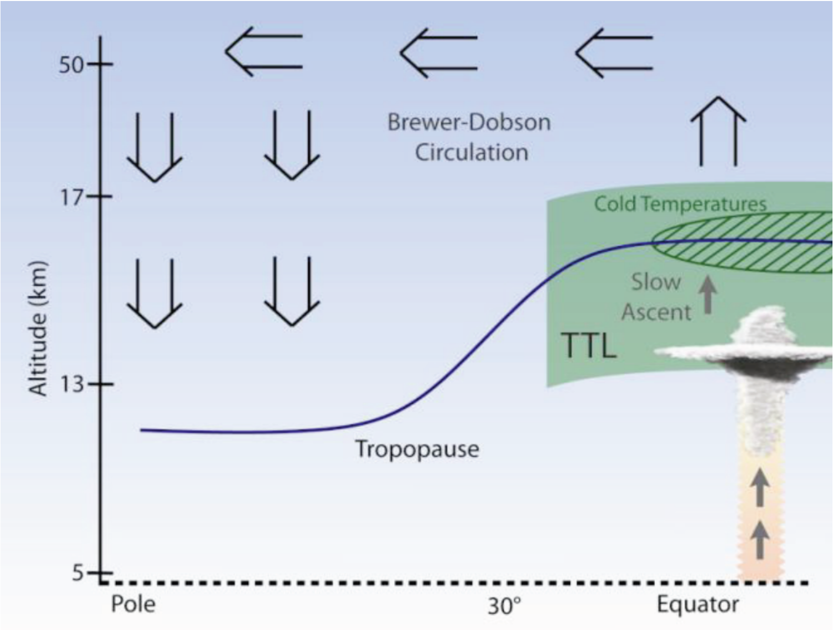

Figure 1.6: The tropical tropopause layer (TTL) in the context of the stratospheric Brewer-Dobson circulation. Air moves upward into the stratosphere through the TTL, where very cold temperatures control water vapor through condensation. Stratospheric motion is downward at high latitudes. Courtesy of Eric Jensen.

Since waves in the TTL originate from the troposphere, a spectrum of TTL waves is similar to the spectrum of convectively coupled equatorial waves (CCEWs). Like CCEWs, waves in the TTL are composed of equatorial Rossby, Kelvin, mixed-Rossby gravity, inertial gravity, and gravity waves. A broad spectrum of these waves in the TTL plays an important role in the processes in the TTL. Waves induce anomalously low temperature resulting in cloud formation and subsequent dehydration of air. Temperature oscillation characteristics determine the dehydration efficiency by modulating cloud microphysical properties. Also equatorial Rossby waves are partially responsible for driving the large-scale tropical upwelling as a shallow branch of the Brewer-Dobson circulation (Birner and Bnisch, 2011; Ueyama et al., 2013; Randel et al., 2008; Garney et al., 2011; Gerber, 2012; Boehm and Lee, 2003; Ryu and Lee, 2010; Ortland and Alexander, 2014).

1.4 Thesis outline

In order to provide a better understanding of roles of tropical waves, this thesis will consider the following questions:

- What are characteristics of precipitation variability from observations? Are tropical waves well represented in current reanalysis models?

  Tropical precipitaion characteristics are investigated using the Tropical Rainfall Measuring Mission (TRMM) 3-hourly estimates, and the result is compared with five reanalyses including ERA-interim (ERA), Modern-Era Retrospective Analysis (MERRA), National Centers for Environmental Prediction (NCEP)-National Center for Atmospheric Research (NCEP1), NCEP-Department of Energy (NCEP2), and NCEP-Climate Forecast System Reanalysis (CFSR). Precipitation characteristics are evaluated in terms of the mean, convectively coupled equatorial wave activity, frequency characteristics, diurnal cycle, and seasonality of regional precipitation variability associated with submonthly scale waves. Generally the latest reanalyses such as ERA, MERRA, and CFSR show better performances over NCEP1 and NCEP2. However, all the reanalyses are still different from observations. Besides the positive mean bias in the reanalyses, a spectral analysis revealed that the reanalyses have over-reddened spectra with persistent rainfall. MERRA has the most persistent rainfall, and CFSR appears to have the most realistic variability. The diurnal cycle in NCEP1 is extremely exaggerated compared to TRMM. The low-frequency waves with the period longer than 3 days are relatively well represented in ERA, MERRA, and CFSR, but all the reanalyses have significant deficiencies in representing convectively coupled equatorial waves and variability in the high-frequency range.

- Is there any better way of implementing waves in trajectory simulations of the dehydration process in the tropical tropopause layer?

  We have developed a new wave scheme particularly aiming to provide better temperature fields with realistic variability for trajectory modeling of dehydration processes in the TTL. The new scheme includes amplitude-phase interpolation and amplification of waves in reanalysis data. Amplification factors are based on statistical variability differences between reanalysis data and radiosonde observations at 24 tropical locations over 1997-2013. We show that conventional linear interpolation of temperatures in the vertical coordinate degrades wave amplitudes and variability. Amplitude-phase interpolation in Fourier space greatly mitigates the problem found in linear interpolation. Furthermore, amplitudes of existing waves in reanalyses were amplified to generate realistic variability. In addition to improvements in variability, the scheme gives additional improvements by lowering cold-point temperatures and raising cold-point tropopause heights. Having realistic variability with the new approach will reduce uncertainties in simulations of TTL cirrus clouds and stratospheric water vapor.

- What are impacts of waves on the tropical tropopause layer?

  Air ascending across the tropical tropopause layer, a transition layer between the tropical troposphere and stratosphere, gets freeze-dried due to extremely cold temperature. Consequently, the stratosphere is much drier than the troposphere. Despite the existence of only a small amount of stratospheric water vapor, it has significant impacts on the Earth's radiation budget and climate. Temperature in the tropical tropopause layer, especially the cold-point temperature, is a key regulator of stratospheric water vapor. Here, using observations from tropical radiosondes over 1990-2014, we show that waves in the tropical tropopause layer lower cold-point temperature by 1.6 K on average compared to a state without waves. This reduces the amount of water entering the stratosphere by about 1 ppmv, which is ∼25% of the total observed entry value, implying reduced radiative impacts on surface climate. Furthermore, wave activity in the tropical tropopause layer has not been constant over the last 2.5 decades, altering the magnitude of the wave impacts on cold-point tropopause temperature at a decadal scale. The change in the direct wave impact is partially (∼20-30%) responsible for the sudden decrease in cold-point temperature and stratospheric water vapor at the end of 2000, which has not been fully explained by changes in the Brewer-Dobson circulation.

- What do we learn about waves in the tropical tropoause layer by aircraft observations?

  One of the flights from the Airborne Tropical TRpopause EXperiment (ATTREX) mission was analyzed. The flight on February 16-17, 2014 provided unprecedented observations of the detailed time evolution of TTL waves and their impacts on tracer transport. The aircraft repeatedly climbed and dove within a horizontal area of 1°×1° centered at 145.9°E, 13.1°N close to Guam (144.8°E, 13.5°N) for about 18 hours. The measurements consist of 24 vertical profiles of meteorological fields, water vapor, and other various trace gases at altitudes between ∼13.5-18.5 km, as well as cloud observations during flight segments at high cruise altitudes. The temperature and horizontal wind data indicate a wave structure with a short vertical wavelength of ∼1.7 km. Profiles of trace gases show a strong relationship with wind anomalies associated with the waves. The observed fine vertical structure cannot be inherently resolved in current climate, analysis, and reanalysis models with a typical vertical resolution of 1 km or coarser due to the limitation of vertical resolution.

Analysis of vertical profiles of meridional wind in radiosonde and MERRA data reveals that these fine vertical, subgrid-scale waves contribute to a significant portion of variability in the TTL.

Chapter 2

Tropical precipitation variability and convectively coupled equatorial waves

Generating realistic precipitation variability and convectively coupled equatorial waves (CCEWs) in climate simulation models is a fundamental problem in correct prediction of middle atmosphere climate as well as in accurate weather forecasting. Despite its importance, precipitation in current climate simulations shows large disagreements among different models. Studies have revealed that many general circulation models (GCMs) still do not produce CCEWs properly (Lin et al., 2006; Straub et al., 2010). Moreover, most of the studies have been conducted only for intraseasonal scale variability.

Evaluation studies of precipitation have also been conducted for reanalyses (Betts et al., 2006; Bosilovich et al., 2008; Janowiak et al., 1998, 2010; Roads, 2003; Wang et al., 2012). Reanalysis datasets are produced by a frozen model with data assimilation, the process that integrates observations with model simulations, to provide a dynamically consistent analysis for an extended period of time. Unlike the state variables, which are assimilated, precipitation in reanalyses is almost entirely a model product. In some cases, precipitation is assimilated, but weighting of observational information in the analysis procedure is so low that final precipitation products still heavily depend on model physics (Rienecker et al., 2011). So, precipitation in reanalyses can be a metric of model performance in dealing with convective processes, constrained by more realistic weather and climate states than GCMs. The studies for precipitation in reanalyses have also focused on intraseasonal or longer time scales.

To investigate precipitation characteristics as a result of CCEWs and as a source of vertically propagating waves, we extracted the highest available time resolution precipitation products from five reanalyses and the Tropical Rainfall Measuring Mission (TRMM) satellite observations. The spectral analysis for fine time resolution data enables us to access precipitation variability in the context of CCEW activity. By choosing the time frame of 36 days for each spectral analysis set, we can investigate the seasonal evolution of submonthly precipitation variability in different tropical regions.

2.1 Datasets

We analyzed precipitation data for the period of January 2005 through December 2007 from five reanalyses: ERA-interim (ERA) (Dee et al., 2011), Modern-Era Retrospective Analysis (MERRA) (Rienecker et al., 2011), National Centers for Environmental Prediction (NCEP)-National Center for Atmospheric and Research (NCEP1) (Kalnay et al., 1996), NCEP-Department of Energy (NCEP2) (Kanamitsu et al., 2002), and NCEP-Climate Forecast System Reanalysis (CFSR) (Saha et al., 2010). ERA-interim is the latest reanalysis produced at the European Centre for Medium-Range Weather Forecasts (ECMWF). MERRA is generated by NASA's Goddard Earth Observing System (GEOS) atmospheric model v. 5.2.0 and data assimilation system (DAS). CFSR is the ocean-atmosphere coupled global NCEP reanalysis, an improved version of NCEP1 and NCEP2. The key features and basic information related to precipitation in the reanalyses are listed in Table 1. We used 6-hourly or 3-hourly products, if available, to capture temporal precipitation variability of high-frequency scales.

To compare with the reanalysis results, we used the 3B42 dataset from the Tropical Rainfall Measuring Mission (TRMM) (Huffman et al., 2007). The TRMM 3B42 is a 3-hourly product with the grid resolution of 0.25°x0.25° between 50°S and 50°N. Various satellite measurements were used to generate the precipitation data of 3B42. A combination of the TRMM precipitation radar (PR), the TRMM microwave imager (TMI), and microwave data from other satellites provide precipitation estimates, but there are measurement gaps due to sparse sampling. By using the infrared (IR) channel data from geostationary earth orbit satellites, precipitation estimates were adjusted and covered uniformly in space and time. The final rain products were merged with rain gauge analyses where available.

Table 2.1: Information of five reanalyses analyzed in this study.

	Model resolution	Available data resolution	Model	Convective parameterization	Reference
ERA	T255 (~79 km); L60	1.5° × 1.5°; 3-hourly	ECMWF Cy31r2	Tiedtke scheme revised by Gregory et al.	Dee et al. (2011)
MERRA	1/2° × 2/3°; L72	1/2° × 2/3°; 1-hourly	GEOS, version 5.2.0; DAS	Modified version of the relaxed Arakawa–Schubert convective scheme	Rienecker et al. (2011)
NCEP1	T62 (~210 km); L28	1.875° × 1.905°; 6-hourly	NCEP Climate DAS	Simplified Arakawa–Schubert convective parameterization scheme	Kalnay et al. (1996)
NCEP2	T62 (~210 km); L28	1.875° × 1.905°; 6-hourly	NCEP Climate DAS	Minor tuning of the same convective parameterization as in NCEP1	Kanamitsu et al. (2002)
CFSR	T382 (~38 km); L64	0.313° × 0.312°; 1.875° × 1.905°; 1~6-hourly	Atmosphere (GFS)–ocean (MOM4, Noah) coupled model (GSI for atmosphere, GODAS with MOM4 for ocean and sea ice, and GLDAS and Noah for land) was used for analyses.	Simplified Arakawa–Schubert convection with momentum mixing	Saha et al. (2010)

Although TRMM 3B42 is one of the best high-resolution precipitation datasets, and TRMM monthly precipitation is well validated, we note that it still has uncertainties on subdaily time scales. Using IR brightness temperatures where microwave measurements are unavailable would yield problems with non-convective precipitation. Furthermore, Huffman et al. (2007) described how lack of sensitivity to light precipitation over the ocean in one microwave product has resulted in lower skill in moderate and light rainfall events on subdaily time scales. Nonetheless, their results show TRMM 3-hourly products capture most of the rainfall events observed in a buoy gauge dataset in the western Pacific ITCZ. Histograms of TRMM 3B42 and radar data generally match, and the diurnal cycle of TRMM 3B42 has good agreement with gauge observations with slight phase and amplitude differences.

2.2 Methodology

We performed a spectral analysis for longitude-time cross sections to identify space-time precipitation variability. This method is especially useful for studying zonally propagating disturbances, giving the spectral dispersion in the wavenumber-frequency space. Since precipitation is spatially and temporally intermittent, a finer resolution gives higher values of power spectrum and variance. For more reliable quantitative comparisons of variance, we rebinned data in the horizontal to approximately the same resolution of about 1.875°x1.875°. Table 2.1 shows the available temporal and spatial resolutions of five reanalyses. The spatial rebinning process is not applied to NCEP1, NCEP2, and CFSR, which are already provided at relatively coarse resolution of approximately 1.875°x1.905° in the tropics. We calculate area-weighted average rain rates to rebin the different horizontal resolutions of TRMM, ERA, and MERRA into 1.875°x1.875°. Hourly data from MERRA and CFSR are averaged into the 3-hourly resolution.

Since we are interested in submonthly scale variability and its seasonal changes, the time period of 36 days was chosen for the Fast Fourier Transform (FFT) with 6-day overlap and taper. This time period will resolve westward and eastward IG waves, TD-type waves, MRG waves, most Kelvin waves, and transient parts of the Rossby wave spectrum. The disturbances longer than the monthly scale lie at zero frequency in our wavenumber-frequency spectrum. We define this as the quasi-stationary part of the spectrum. Rossby waves have stronger power at longer than 30 days, and the MJO is a 30-90 day intraseasonal oscillation. Thus, the quasi-stationary spectrum is contributed mostly by the MJO and very slowly moving Rossby waves.

Many studies for CCEWs utilize the method of symmetric and anti-symmetric decomposition against the background spectrum to identify wave signals (Hendon and Wheeler, 2008; Lin et al., 2006; Wheeler and Kiladis, 1999). In these studies, the symmetric component is defined by the average of perturbation variables between the northern and southern hemispheres, and anti-symmetric is half of the difference. Then the symmetric and anti-symmetric spectra are divided by the smoothed background spectrum. Although this method has an advantage in identifying the CCEWs and their phase speeds through the statistically significant dispersion curves in the spectrum, its resultant spectrum only shows relatively significant spectral peaks for meridionally symmetric and anti-symmetric disturbances against the background. On the other hand, the raw spectrum gives absolute variance in Fourier space so that we can compare total precipitation variance as a function of wavenumber and frequency in different datasets. In this paper, we are interested not only in CCEW signals but also in precipitation variability and frequency characteristics. Hence, to evaluate total precipitation variability depending on wavenumber and frequency, we used the raw spectrum without smoothing. To determine whether and how CCEWs are represented in reanalyses, we examine prominent lobes in raw spectra of symmetric and anti-symmetric components.

2.3 Results

2.3.1 Mean precipitation

Figure 2.1 shows the spatial distribution of 3-year mean precipitation. All reanalyses have biases in the tropics as pointed out in other studies. ERA and MERRA have almost the same mean value of 0.2 mm h^{-1}, and they share similar characteristics in mean precipitation with consistent positive biases over all tropical regions and over the time series. (See Figure 2.1-2.3) The mean of NCEP1 is 0.19 mm h^{-1}, which is close to the mean of ERA and MERRA, but it shows a more spatially uniform distribution with less precipitation in the ITCZ compared to other datasets. In contrast, NCEP2 has a significant high bias in the ITCZ. CFSR also has strong precipitation along the ITCZ, but intensified precipitation distributions in the ITCZ are very different between NCEP2 and CFSR. While the positive bias of NCEP2 is significant in the western Pacific, precipitation along the ITCZ in CFSR is exaggerated mainly in the central and eastern Pacific. In Figure 2.2, precipitation is averaged over tropical latitudes 15°S-15°N. Longitude ranges that are mostly land with more than 70% of the total are marked with the black bars in the longitude axis. The dots in the longitude axis represent land-ocean mixed regions, with 30%-70% land. The geographical precipitation patterns of ERA and MERRA look the same except in Africa. ERA and CFSR generate more rainfall than other datasets in Africa, while MERRA shows suppressed rainfall in Africa. Peaks in reanalyses on the west side of America reveal excessive orographic precipitation along the Andes. The time series of zonally averaged precipitation as a function of latitude in Figure 2.3 shows the seasonal migration of the ITCZ and the Southern Pacific Convergence Zone (SPCZ). Although there are some biases in mean precipitation (mostly in the ITCZ), all datasets generally agree on the seasonal changes: the ITCZ moves farther to the north at 7°-12°N during July-August-September, and strong precipitation in the SPCZ occurs during January-February.

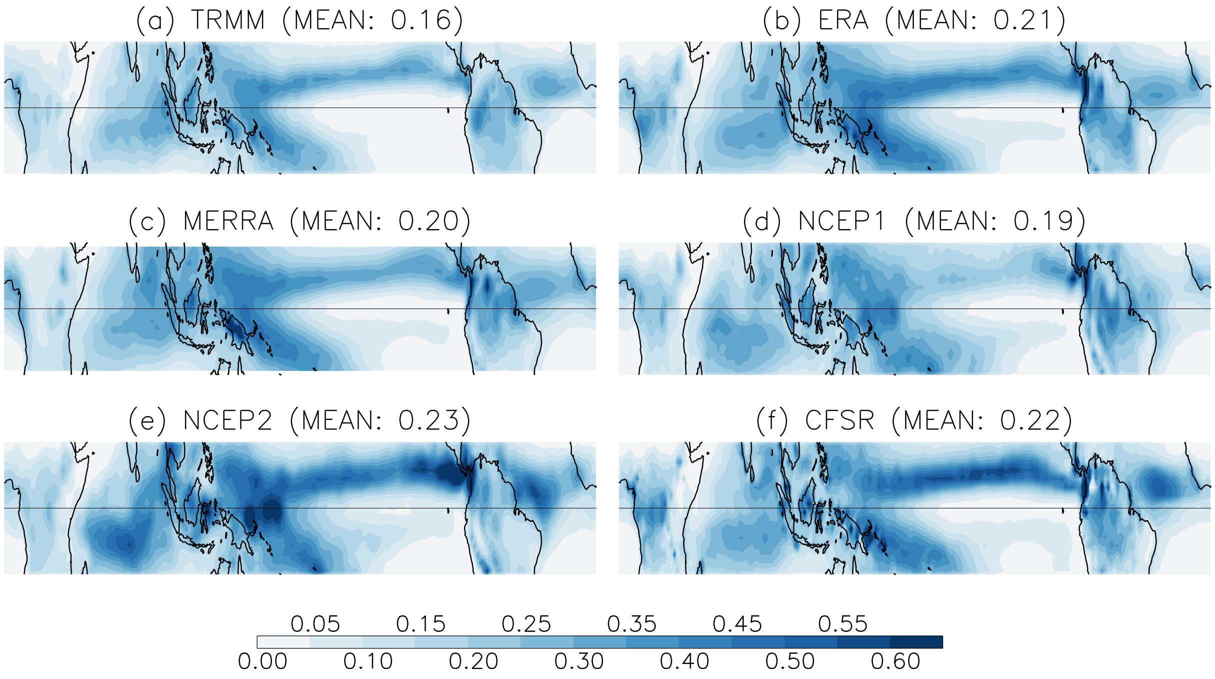

Figure 2.1: Tropical mean precipitation (mm h^{-1}) in 2005-2007 for (a) TRMM, (b) ERA, (c) MERRA, (d) NCEP1, (e) NCEP2, and (f) CFSR.

2.3.2 Longitude-time section and PDF

Figure 2.4 shows zonal propagation of precipitation at 5°N between June-September 2006. Observed TRMM precipitation in Figure 2.4a identifies the diurnal cycle and ubiquitous eastward

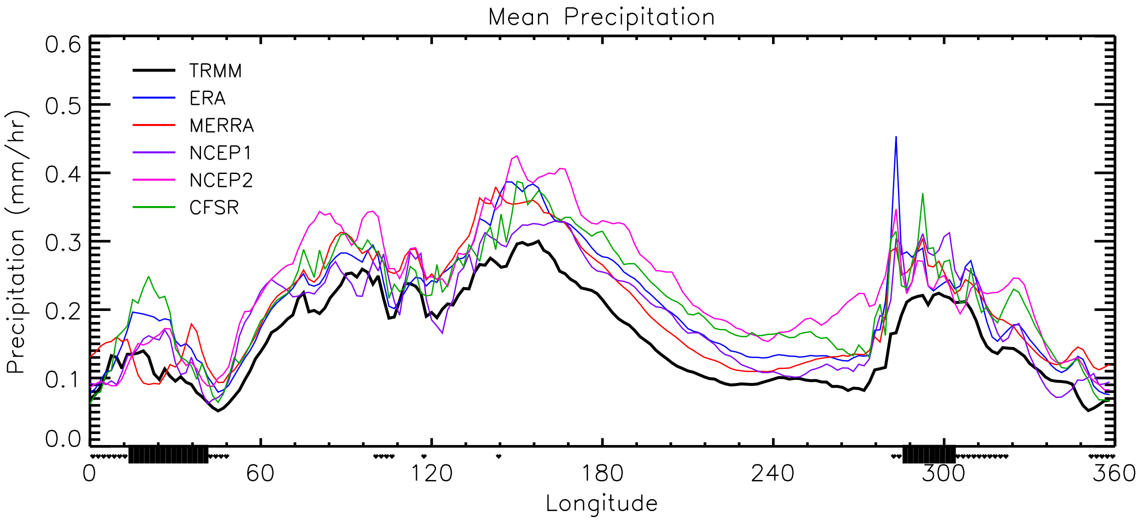

Figure 2.2: Averaged precipitation over the latitude range of 15°S-15°N. Longitude ranges that are mostly land with more than 70% of the total are marked with the black bars in the longitude axis. The dots in the longitude axis represent land-ocean mixed regions, with 30%-70% land.

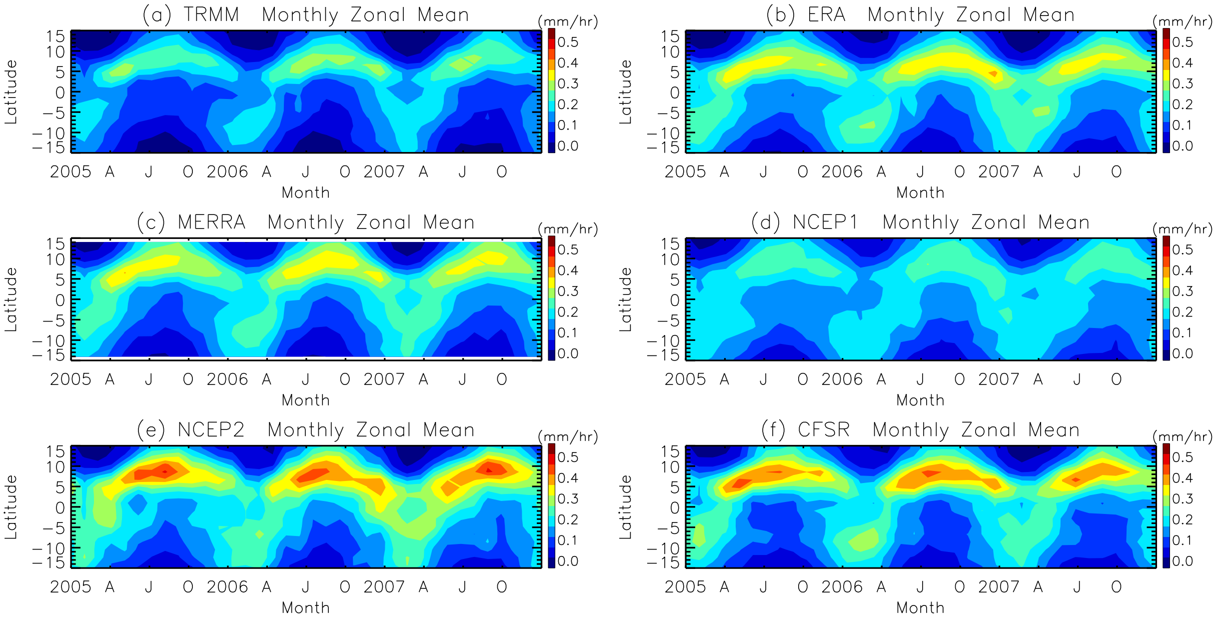

Figure 2.3: Time series of monthly zonal mean precipitation (mm h^{-1}).

and westward propagating features with different speeds. The large-scale eastward moving envelope is the MJO with the period of 30-90 days. The active phase of the MJO is initiated in the Indian Ocean and progresses through the Maritime Continent and the western Pacific at the speed of 5 m s^{-1}. There are also smaller-scale eastward and westward waves within the MJO envelope.

In Figure 2.4a, relatively faster eastward moving signals with the phase speed of about 10 m s^{-1} are Kelvin waves. Westward signals are composed of TD-type and westward IG waves. Western African rainfall is dominated by small-scale westward propagating waves, mostly triggered by the diurnal cycle, which are strongly coupled to convection. The diurnal cycle is clearly seen over the land regions.

Figures 2.4b-f show the same longitude-time cross sections for reanalyses. Precipitation patterns in ERA, MERRA, and NCEP1 are broadened in space and time. Widespread persistent, weak rainfall is a common problem in climate models. The probability density function (PDF) and the 99th percentile of 3-year precipitation in Figure 2.5 shows that intense rainfall events are highly underestimated in ERA, MERRA, and NCEP1. NCEP2, however, has more intense and less persistent precipitation patterns. Westward propagating precipitation features in NCEP2 in Figure 2.4e are very strong compared to TRMM, especially in the eastern Pacific. CFSR seems to have the most realistic variability and wave propagation characteristics. The PDF and the 99th percentile of precipitation intensity in CFSR matches the values in TRMM very well in Figure 2.5, and the spurious strong westward waves in the Pacific of NCEP2 have become more realistic in CFSR shown in Figure 2.4f. We will examine zonal propagation characteristics more closely in the following sections.

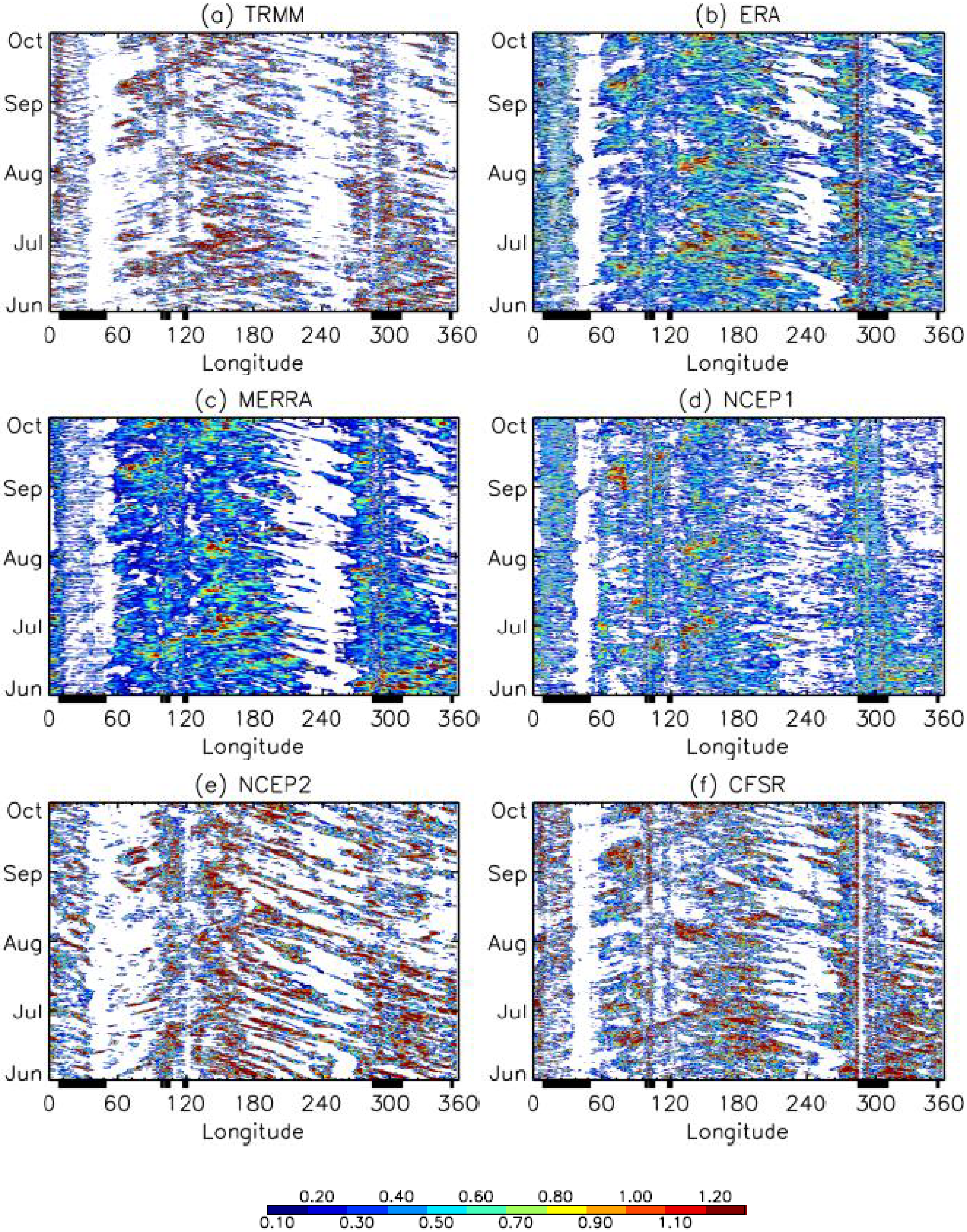

Figure 2.4: Longitude-time section of precipitation (mm h^{-1}) at the latitude of 5°N between June-September 2006. Land regions are denoted by black bars in the longitude axis.

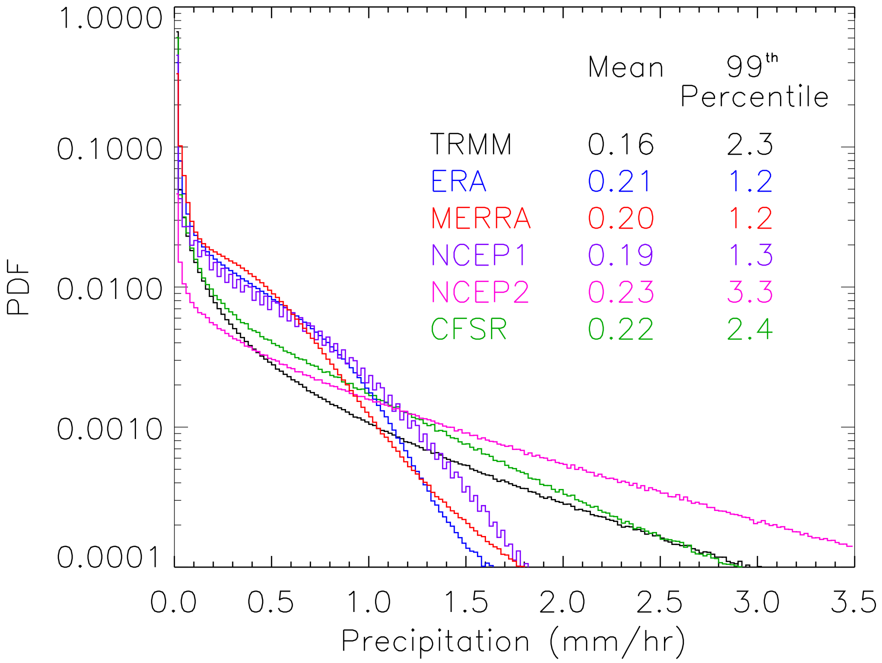

Figure 2.5: The probability density function (PDF) of precipitation between 15°S-15°N over 2005-2007.

2.3.3 Spectrum

Figure 2.6 illustrates averaged spectra, without filtering or smoothing, between 15°S-15°N over the time period of 2005-2007. These raw spectra are very *red*, which means spectral density gets higher with lower wavenumber and lower frequency. This *redness* of the spectrum is a universal property of climatic variables. It suggests that the atmospheric processes occur in the broad space and time scales, and that one scale of process is always accompanied by the other scales.

Although the redness is an apparent feature of the spectra, we can also identify wave signals in the raw spectra, following preferred lobes in each propagation direction. In Figure 2.6, the slopes (frequency/wavenumber) of dotted lines correspond to wave phase speeds, so eastward (westward) propagating disturbances compose the positive (negative) wavenumber spectrum. There is a prominent lobe in the eastward direction with a phase speed of about 14 m s^{-1}, which corresponds to the equivalent depth of 20 m, in the TRMM spectrum in Figure 2.6a. This is mostly contributed by the Kelvin waves and the eastward IG waves. In the westward direction with negative zonal wavenumbers, the preferred speed depends on the wavenumber and frequency. In the low-frequency range with periods longer than 7 days, the preferred westward phase speed is slowest and corresponds to the equatorial Rossby wave dispersion curve. As the frequency becomes higher, the preferred phase speed increases. At the higher-frequencies with periods shorter than 3 days, the prominent lobe follows along a phase speed of -18 m s^{-1} mainly due to westward IG waves. The phase speed of the westward IG wave mode is slightly faster than the value of the eastward IG wave mode. The Doppler shift by the westward zonal wind in the tropical troposphere is considered to be the cause of the directional difference in the preferred phase speeds. The intensified spectrum at the frequency of 1 cycle per day (CPD) is due to the diurnal cycle.

Low-frequency large-scale waves including Kelvin, MRG, and Rossby waves can be better illustrated in spectra of the symmetric and anti-symmetric components in Figure 2.7 and 2.8. The symmetric and anti-symmetric spectra of TRMM observations show enhanced power following theoretical dispersion curves of the equatorial shallow water equations with the equivalent depth of 20 m. Kelvin waves are prominent in the symmetric spectrum in Figure 2.7a, MRG waves have a signal in the anti-symmetric spectrum in Figure 2.8a, and Rossby waves are evident in the both spectra. As Tulich et al. (2011) have shown, observed Rossby waves in the westward spectrum are faster than the theoretical dispersion relation due to background easterlies.

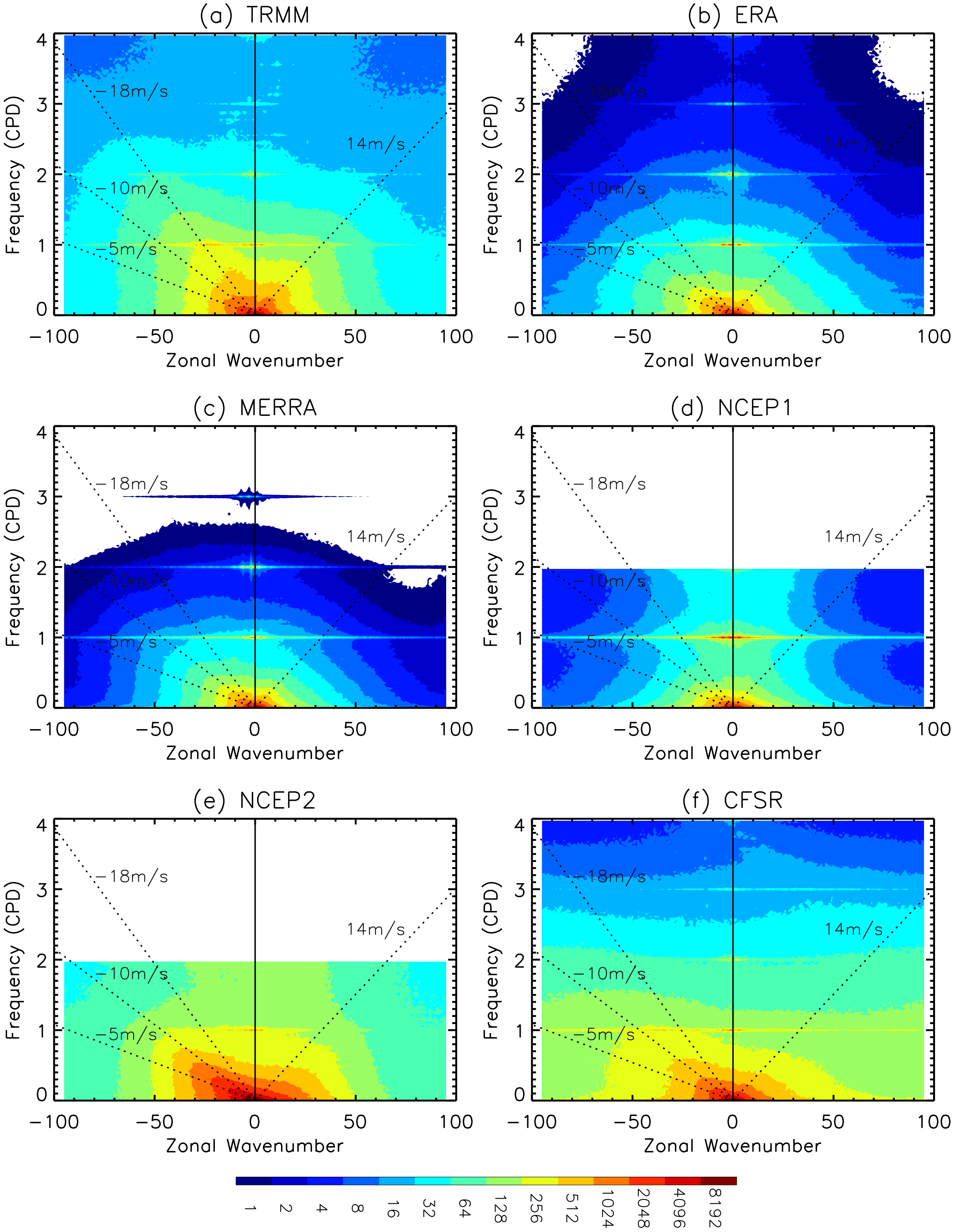

Figure 2.6: Averaged wavenumber-frequency power spectra of precipitation between 15°S-15°N over 2005-2007. Phase speed lines of -5, -10, -18, and 14 m s^{-1} are plotted with dotted lines.

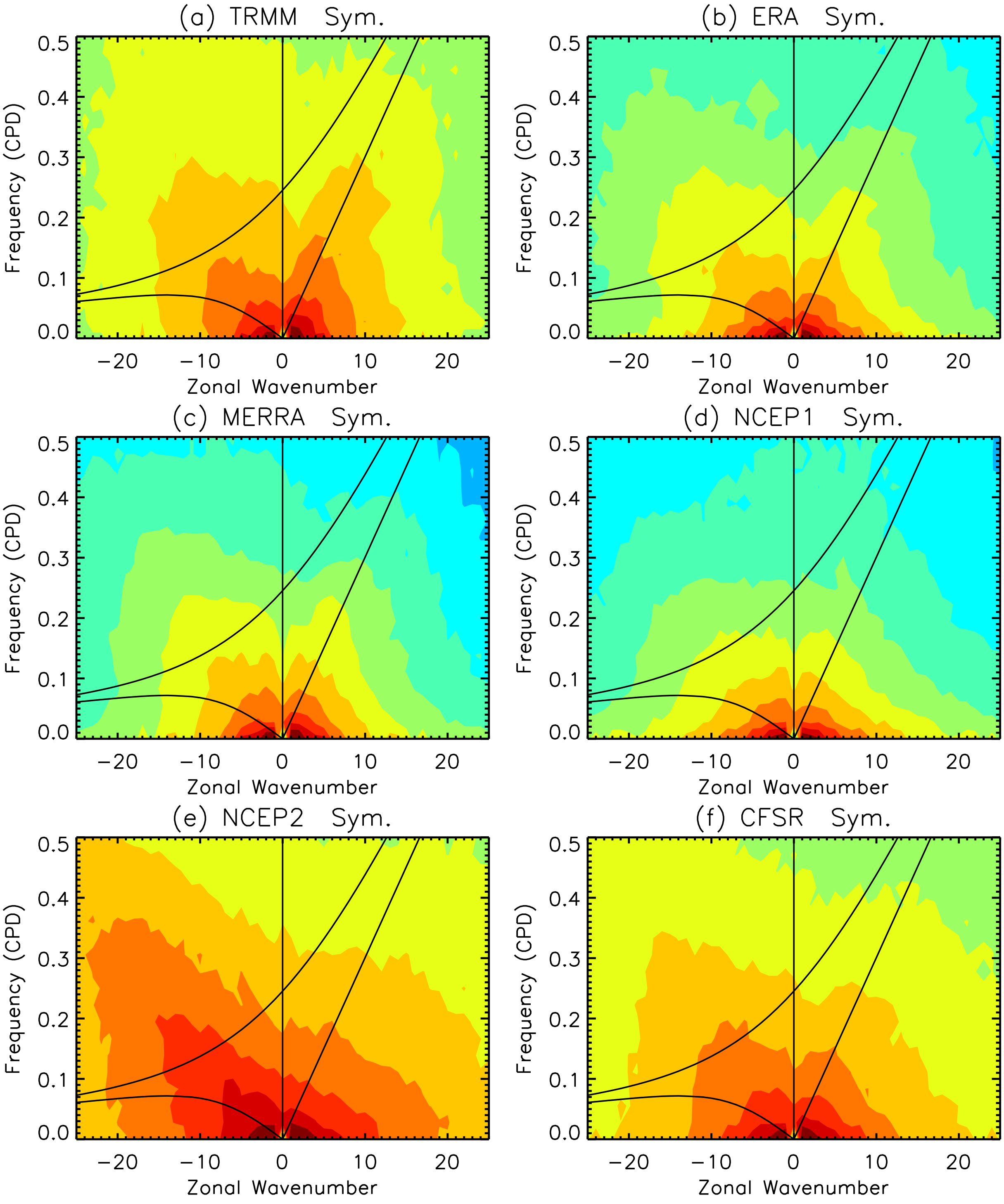

Figure 2.7: Averaged symmetric wavenumber-frequency power spectra of precipitation between 15°S-15°N over 2005-2007. The curves correspond to theoretical dispersion relations of equatorial shallow water equations with the equivalent depth of 20 m. The color scale is the same as in Figure 2.6. Note that the ranges of wavenumber and frequency are different from Figure 2.6.

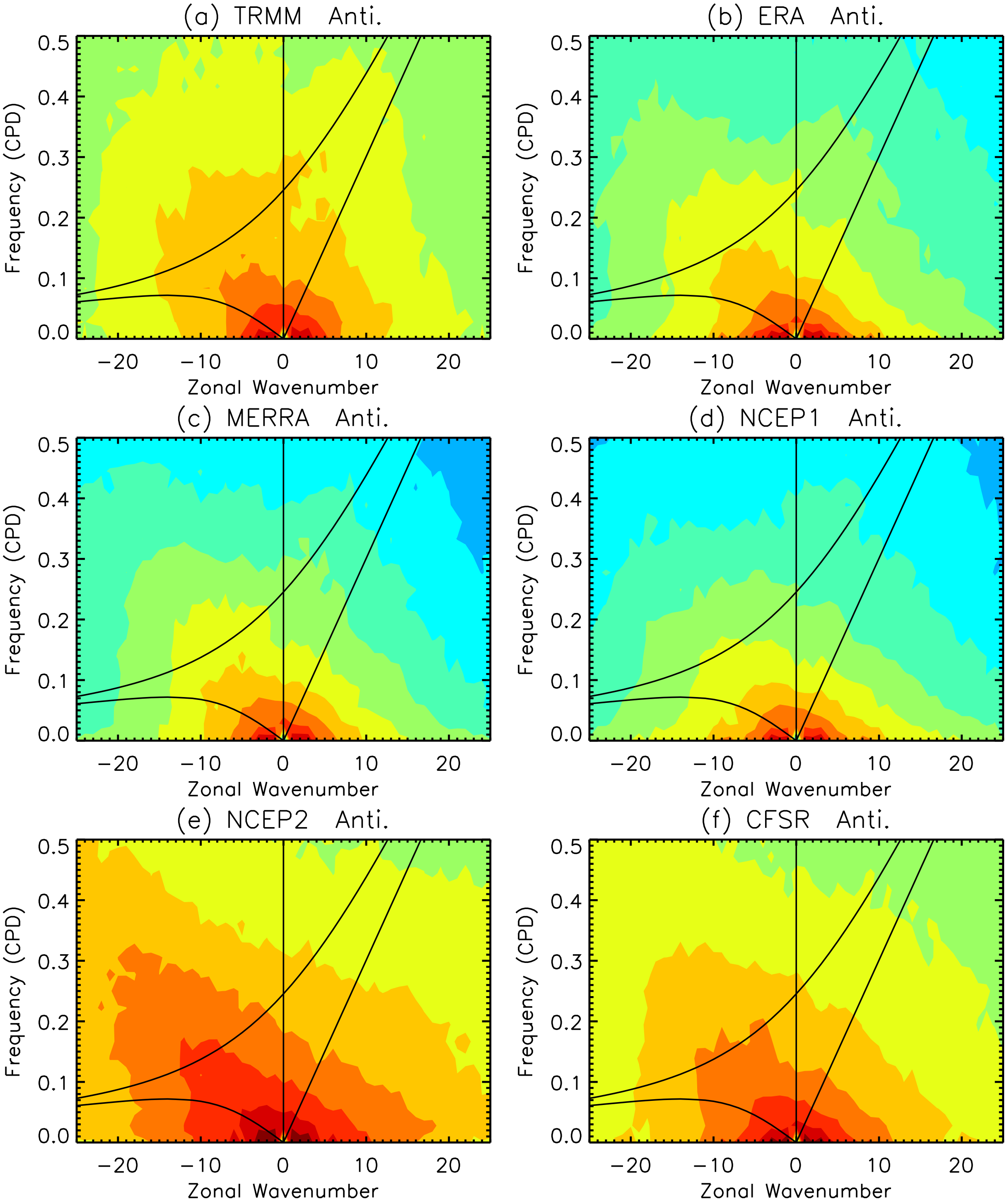

Figure 2.8: Similar to Figure 2.7, except for the anti-symmetric spectra

The spectrum of each reanalysis in Figures 2.6-2.9 reveals its own characteristics and drawbacks. As observed in the longitude-time sections in Figures 2.4b and 2.4c, spectra of ERA and MERRA are also similar in Figures 2.6b and 2.6c with weaker spectral densities compared to TRMM (see also frequency characteristics of power spectra in Figure 2.9). At lower frequencies shown in Figures 2.7b, 2.7c, 2.8b, and 2.8c, preferred phase speeds of Kelvin, MRG, and Rossby waves are the same as TRMM. This suggests that the low-frequency large-scale CCEWs are well represented in ERA and MERRA. However, they are lacking in wave signals at frequencies higher than 1 CPD.

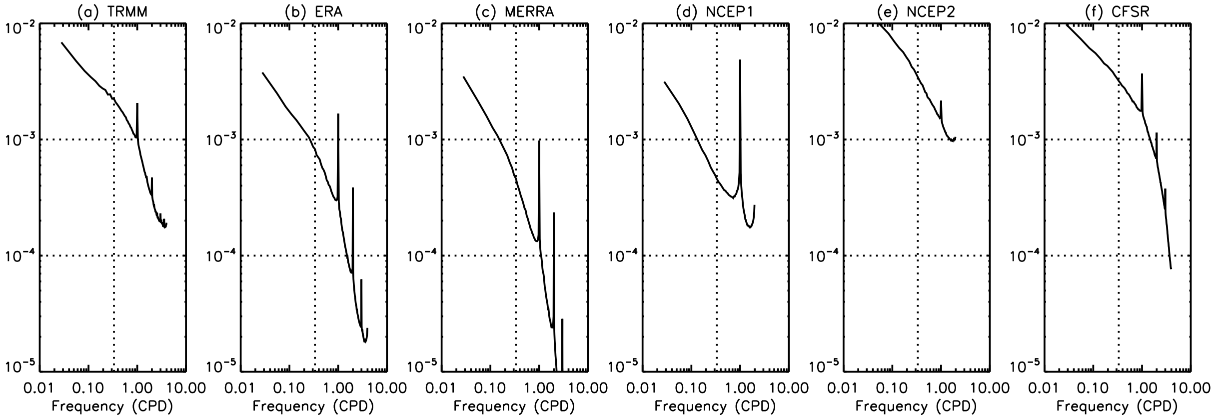

Figure 2.9: Integrated power spectra of precipitation over all wavenumbers.

NCEP1 and NCEP2 have spectra only up to 2 CPD due to the limitation of the time resolution. The striking feature of NCEP1 is the very strong diurnal cycle (Figures 2.6d-2.9d, and 2.11). Janowiak et al. (1998) reported the overly vigorous diurnal cycle in NCEP1 precipitation by comparing with the Global Precipitation Climatology Project (GPCP), which is a product that combines rain gauge and satellite-derived precipitation. As a complement to this, our spectral analysis has found that the non-migrating diurnal signal near zero wavenumber is especially high, and the migrating diurnal signals are also significant (see Figure 2.6d). The diurnal cycle is so strong that it affects the spectral shape making it difficult to see whether any preferred phase speeds exist in NCEP1. The spectral shapes at low frequencies in Figures 2.7d and 2.8d show weak CCEW signals compared to all other datasets. The spectra of NCEP2 in Figures 2.6-2.8e has strong westward signals at all frequencies less than 1 CPD and with a consistent phase speed between -5 m s^{-1} and -10 m s^{-1}. The different preferred phase speeds in the different wavenumbers and frequencies indicate the properties of dominant wave modes. In the westward direction in NCEP2, it is ambiguous to differentiate the Rossby and IG wave modes since the preferred phase speeds in Figures 2.6-2.8e look the same for these wave modes. Considering the phase speeds of 5-10 m s^{-1} in the westward direction, NCEP2 appears to have overly strong TD-type waves, resulting in weak signals on other westward waves. Moreover, MRG waves lack in the anti-symmetric spectrum in Figure 2.8e. In the positive wavenumber space in Figures 2.6-2.7e, the Kelvin and eastward IG waves are very weak with slower phase speeds than in TRMM.

The spectra of CFSR in Figures 2.6-2.9f reveals that CFSR has improved skill in producing tropical precipitation in terms of the large-scale waves and diurnal variations. Although CFSR is still lacking in wave signals at frequencies higher than 1CPD, the unrealistic strong westward signal in the low-frequency wave modes seen in NCEP2 has in CFSR become closer to the TRMM spectrum. The weak diurnal peaks in NCEP2 are also enhanced in CFSR to very reasonable values.

More quantitative comparison of diurnal variation is depicted in Figure 2.9, which shows the spectrum integrated over all wavenumbers at a given frequency. In ERA and MERRA, the diurnal peaks relative to the background spectra are overestimated compared to TRMM. The extremely exaggerated diurnal signal in NCEP1 is reduced in NCEP2 with the relative peak value less than TRMM. NCEP2 has the weakest relative diurnal peak intensity. The relative diurnal peak intensity in CFSR has a value closest to the TRMM result.

The ratio of the westward to the eastward power spectrum in Figure 2.10 shows the frequency dependence of eastward and westward wave activity. Except at periods longer than 25 days affected by the MJO, westward disturbances in TRMM are larger than eastward disturbances. At frequencies lower than 1/3 CPD, all reanalyses overestimate the westward component, suggesting strong low-frequency easterly wave activity in reanalyses. This large ratio is also partly due to the underrepresentation of Kelvin waves in NCEP1, NCEP2, and CFSR as indicated by the symmetric spectra in Figure 2.7. Tulich et al. (2012) have concluded that vertical zonal wind shear at low levels, not just the mean flow, is crucial to the direction of convective wave propagation, suggesting the westward bias at lower frequencies in models might be strongly influenced by the unrealistic background shear. At higher frequencies over 0.7 CPD, however, most reanalyses have weaker westward variance, indicating significant model deficiencies in generating high-frequency westward IG waves.

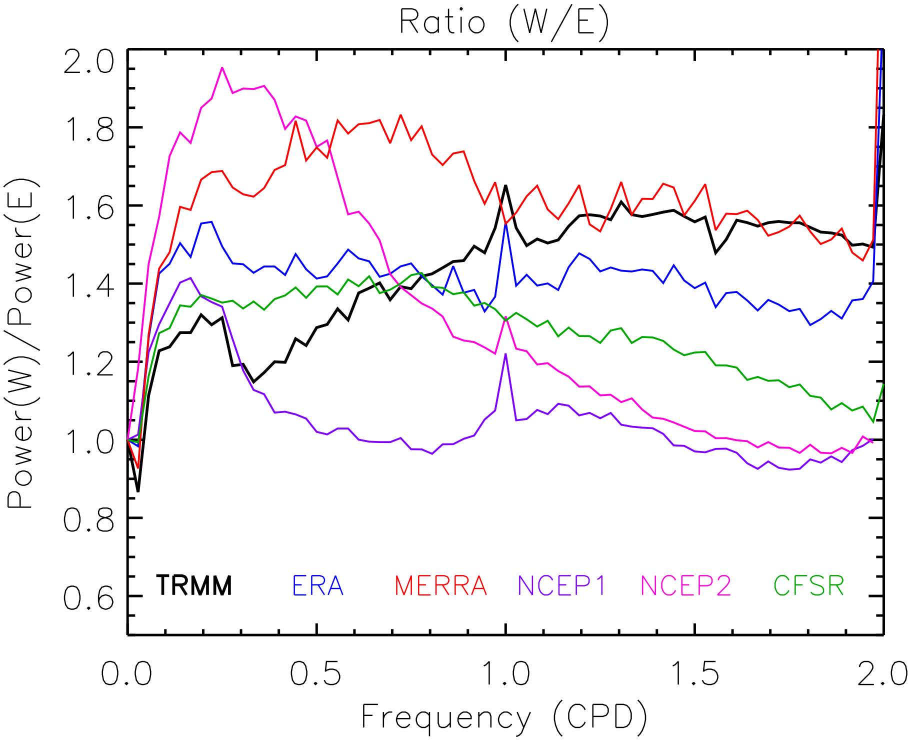

Figure 2.10: The ratio of the westward (wavenumbers <0) to the eastward (wavenumbers >0) power spectrum.

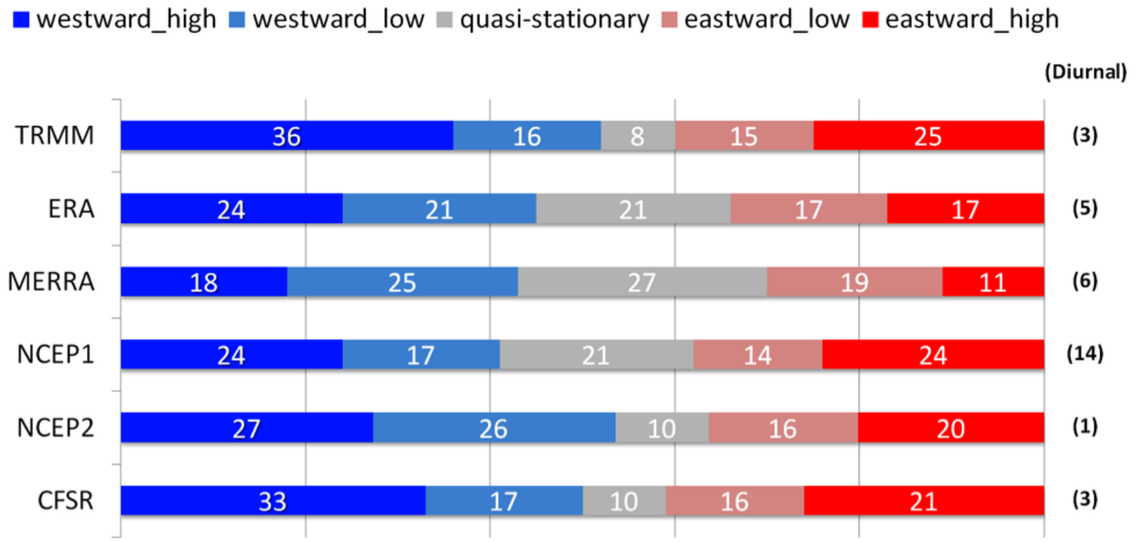

Figure 2.11: Percentage of the power spectrum categorized into five groups: quasi-stationary [eastward and westward with period >30 days], westward-high [westward with frequency >1/3 CPD (period <3 days)], westward-low [westward with frequency <1/3 CPD (period >3 days)], eastward-high [eastward with frequency >1/3 CPD (period <3 days)], and eastward-low [eastward with frequency <1/3 CPD (period >3 days)]. The contribution of the diurnal cycle is included in the high-frequency category. The number in the parenthesis is the percentage of the harmonics of the diurnal cycle, at the frequencies of 1, 2, 3, and 4 CPD, relative to the total variance.

The directional scale-dependent propagation information in precipitation can be gained by integrating spectra within desired spectral bands (Figure 2.11). Here, we divided the wavenumber-frequency spectrum into five categories:

- quasi-stationary [eastward and westward with period >30 days],
- westward-high [westward with frequency >1/3 CPD (period <3 days)],
- westward-low [westward with frequency <1/3 CPD (period >3 days)],
- eastward-high [eastward with frequency >1/3 CPD (period <3 days)], and
- eastward-low [eastward with frequency <1/3 CPD (period >3 days)].

The gray color represents the percentage of disturbances with periods longer than the monthly scale. Thus, the MJO and the slowly moving Rossby wave signals with periods longer than 30 days will be in this quasi-stationary category in our study. To the left of the gray color are the westward percentages and to the right are the eastward portions. We distinguished the high frequency from the low frequency with respect to 1/3 CPD (period of 3 days) so that the Kelvin, Rossby, MRG, and TD-type waves are included in the low-frequency category. The contribution of IG waves and the diurnal cycle is included in the high-frequency category. The number in the parenthesis is the percentage of the harmonics of the diurnal cycle, at the frequencies of 1, 2, 3, and 4 CPD, relative to the total variance.

Generally, reanalysis spectra are redder than TRMM. This means the spectral densities are more concentrated in the low wavenumbers and low frequencies. The overly red spectra imply that individual convection events are more persistent in physical space, as discussed in the studies of Ricciardulli and Sardeshmukh (2002) and Tulich et al. (2011) showing higher autocorrelation values from an over-reddened spectrum. In Figure 2.11 MERRA has the most persistent tropical precipitation. About 27% of the total variance in MERRA is contributed by disturbances at scales longer than 30 days, while only 8% of the variance from TRMM observations is from this quasi-stationary scale. Due to the persistent rainfall in MERRA, the high-frequency variance seems to be sacrificed: total eastward and westward high-frequency variance is only 29%, which is much lower than the TRMM percentage of 61%. The choice of the convective parameterization is known to mainly control the mean and variability of precipitation as well as the existence of CCEWs in model simulations. Ruane and Roads (2007) pointed out that the relaxed Arakawa-Schubert scheme tends to have a lack of high-frequency variability in spite of its better performance in interannual variability. Here, we have found the same conclusion for the relaxed Arakawa-Schubert scheme, which has been used in the MERRA GEOS v.5.2.0 assimilation system. ERA shows a better spectral distribution than MERRA, but the low-frequency disturbances are still overestimated. About 30% of the high-frequency spectrum is contributed by the diurnal cycle in NCEP1. NCEP2 and CFSR have the most reasonable fraction of precipitation variance at the quasi-stationary scale. CFSR's variance at high frequencies is the most realistic compared to other reanalyses.

2.3.4 Regional and seasonal variance

Regional distribution of precipitation variance is shown in Figure 2.12. The variance is defined by an integral of the inverse FFT of a spectrum. As suggested in the previous sections, variances in ERA, MERRA, and NCEP1 are much smaller than in TRMM. NCEP2 has strong variance along the ITCZ and SPCZ. CFSR has exaggerated variance from the central to eastern Pacific, which is also observed in mean precipitation in Figure 2.1f.

The ratio of the high-frequency variance (>1/3 CPD) to the low-frequency variance (<1/3 CPD) in Figure 2.13 illustrates regional differences in the frequency characteristics. The white color depicts regions where total integrated variance for the high frequency variance is nearly the same as the low frequency variance. A high ratio with red colors in Figure 2.13 shows that precipitation in these areas is more influenced by the high-frequency disturbances. In western Africa, TRMM shows up to four times stronger variance in the high-frequency waves than in the low-frequency waves. The convectively coupled IG waves is the largest contribution of the high-frequency variance. Generally, over land, the impact of high-frequency precipitation variability is most important: the ratio is relatively high over Africa, America and the Maritime Continent (Figure 2.13a). Although the ratio along the ITCZ is low compared to the ratio over land, high-frequency variability is still important in the ITCZ areas.

As discussed in the previous section, the high-frequency variability in ERA and MERRA is much weaker than in TRMM. The weakness of these high-frequency variances in ERA and MERRA is a problem over all tropical regions in Figure 2.13b and 2.13c. The lowest value of the mean ratio (See numbers in Figure 2.13) in MERRA indicates that MERRA has the most persistent tropical precipitation. The ratios over Africa in all reanalyses, except in CFSR, are significantly lower than the ratio in TRMM. It appears that NCEP1 shows a good regional correlation of the variance ratio with TRMM, but this is because of the strong diurnal cycle in NCEP1 (Figure 2.14). In other words, the patterns of the ratios from TRMM and NCEP1 look similar in Figure 2.13 for a different reason. Figure 2.14 indicates the location of the exaggerated diurnal cycle in each reanalysis. Compared with TRMM, the regional correlation of the diurnal cycle is most reasonable in CFSR, while NCEP2 has weaker variation.

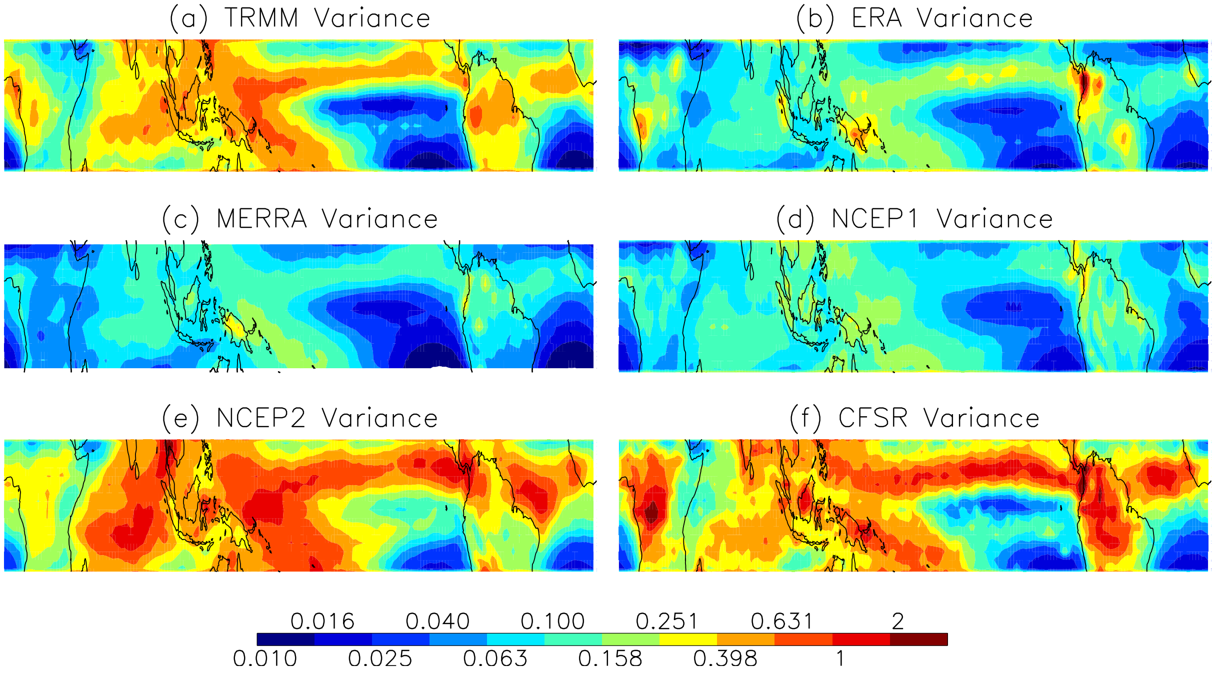

Figure 2.12: Precipitation variance (mm^2 h^{-2}) calculated from an integral of the inverse FFT of a spectrum.

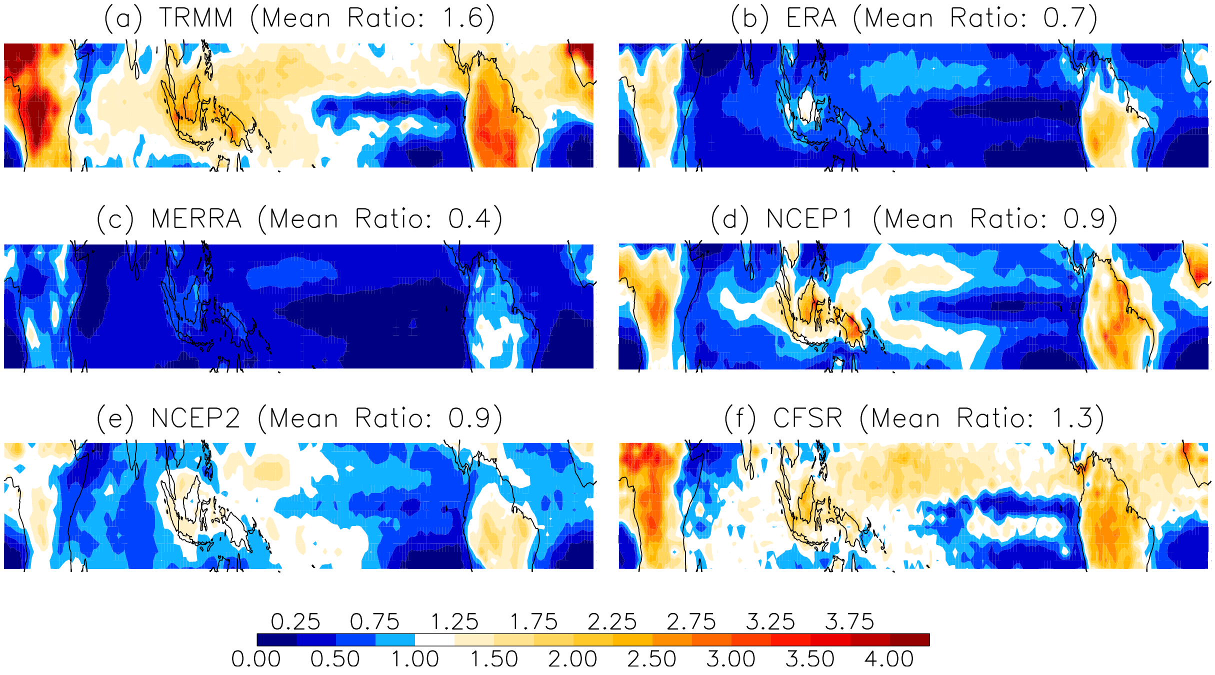

Figure 2.13: Ratio of the high-frequency (periods <3 days) variance to the low-frequency (periods >3 days) variance.

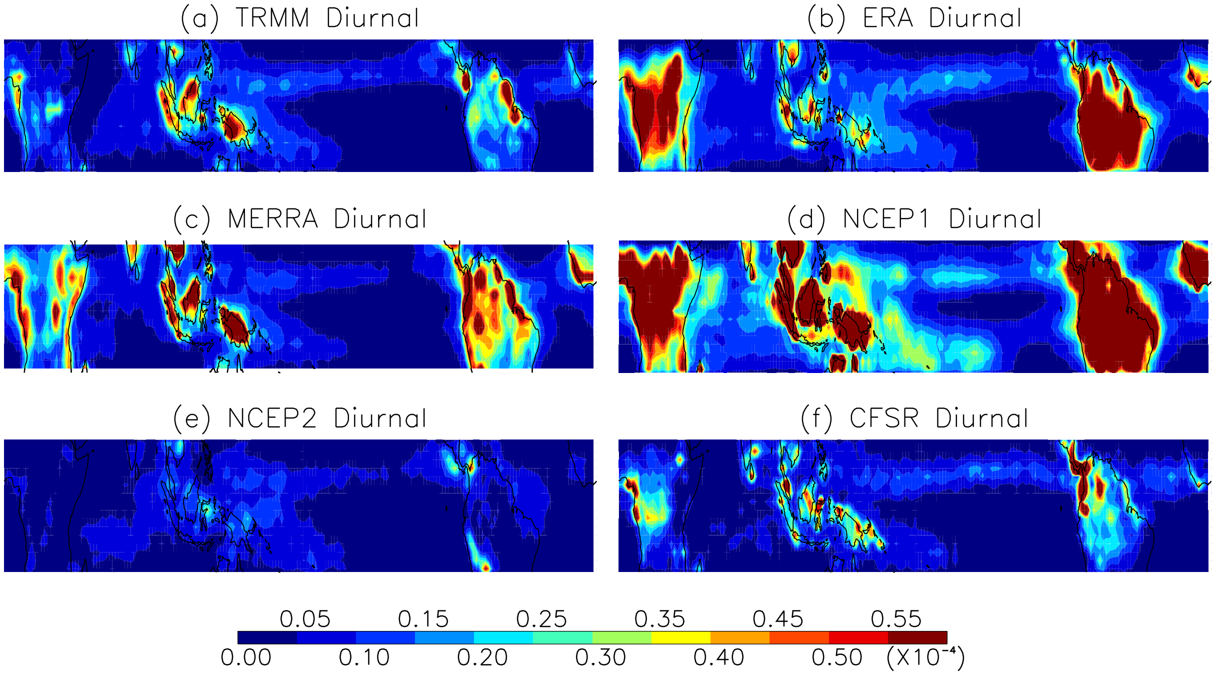

Figure 2.14: Fraction of the total variance contributed by the diurnal cycle and harmonics.

To investigate seasonality of CCEW activity in different wave modes for each tropical region, we divided the tropics into seven regions: Africa, the Indian Ocean, the Maritime Continent, the western Pacific, the eastern Pacific, America, and the Atlantic Ocean. We will mainly discuss seasonal changes in regional precipitation variability from TRMM observations, shown in Figure 2.15. Here, we have used the same five categories (quasi-stationary: green, westward-high: dark blue, westward-low: light blue, eastward-high: red, and eastward-low: orange) distinguished by the frequency and the propagation direction as used in Figure 2.11.

In TRMM observations, some regions such as Africa, the western and eastern Pacific, and America have obvious seasonal variations. Figure 2.15 reveals that westward-high variance is much more significant than variances from other wave modes over all seasons in Africa. Westward-high variance is suppressed during the dry season around December-January-February, and it gets higher for March-April. Then it is suppressed again around June-July. In August westward-high variance shows the most enhanced activity. Since TD-type waves have predominant periods of 3-6 days and IG waves have periods shorter than 3 days, we infer that the strongly enhanced westward-high variance in August corresponds to strong westward IG wave activity influenced by African easterly jet. Tulich et al. (2012) have shown that the composite evolution of TRMM rainfall associated with African mesoscale squall lines is perfectly aligned with filtered anomalies of the westward IG wave band with the phase speed of -18 m s^{-1}. His result further supports the idea that African precipitation is greatly affected by westward IG waves.

In TRMM in Figure 2.15, America and the Atlantic Ocean have different phases of seasonality from Africa, although some of westward waves in these regions originated in western Africa. It seems that the variance in the Maritime Continent is mainly characterized by the MJO, because the variances of all wave modes generally go with the quasi-stationary variance. It is well known that smaller-scale convective clusters are generated within the active phase of the MJO (Zhang, 2005). Thus we expect that strong MJO convective activity results in strong synoptic to mesoscale convective precipitation.

Westward variance dominates the seasonal changes in the western and eastern Pacific Ocean in Figure 2.15. The contributions of the eastward and westward disturbances are almost the same during the northern winter, but the westward disturbances of the northern summertime become nearly double the wintertime values. There is a phase difference of precipitation seasonality between the eastern and western Pacific Oceans. The strong westward signal remains until December in the western Pacific Ocean, but it gradually weakens as the season changes in the eastern Pacific Ocean. The dominance of westward-high variance in the Pacific Ocean implies that convection in northern summer is largely influenced by westward IG waves. In contrast to westward variances, eastward variances do not have strong seasonal variations in the Pacific regions like in Africa.

Since westward-high variance dominates the seasonal variation, we further investigate representation of westward-high variability in reanalyses. We find that seasonal enhancement of westward-high variance in different regions in reanalyses generally match the TRMM results. However, in the western Pacific, reanalyses do not reproduce the TRMM annual cycle. It seems that the mechanisms for generation and maintenance of westward-high disturbances in the western Pacific may be different from other regions, and that reanalyses do not represent these. Further studies would be needed.

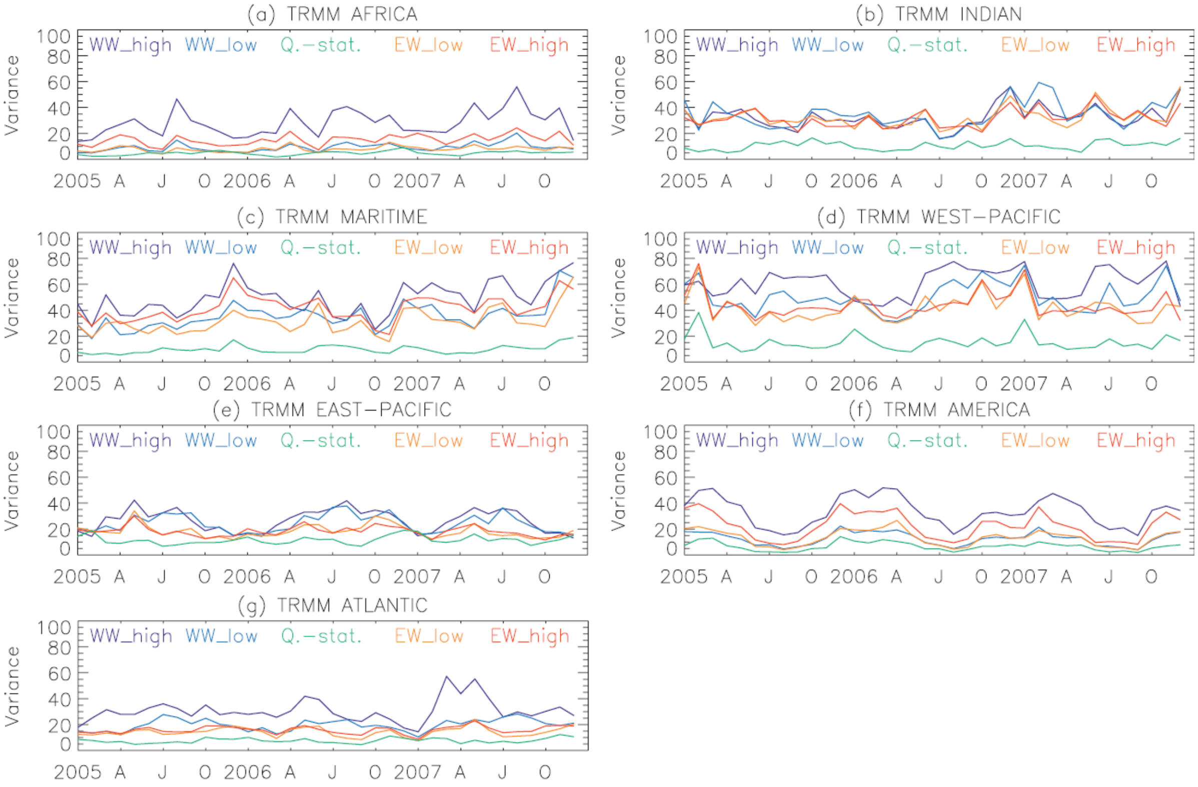

Figure 2.15: Time series of TRMM regional precipitation variance (mm^2 h^{-2}) categorized according to propagation directions and frequency (westward-high: dark blue, westward-low: light blue, quasi-stationary: green, eastward-low: orange, and eastward-high: red).

2.4 Summary and discussion

Using the space-time spectral analysis method, we evaluated submonthly scale variability and CCEW activity of tropical precipitation in five reanalyses. Three-hourly TRMM observations were used as a validation reference to compare reanalysis datasets (3-hourly for ERA, MERRA, and CFSR; 6-hourly for NCEP1 and NCEP2). Besides the common bias among reanalyses, which all show excessive tropical rainfall, the wavenumber-frequency spectrum reveals deficiencies in resolving CCEWs and high-frequency variability. The mean precipitation values and patterns in ERA and MERRA are very similar except in western Africa, and it appears that their regional distributions are close to the distribution in TRMM if the bias is subtracted. The mean of NCEP1 shows weaker rainfall along the ITCZ and more rainfall outside the ITCZ compared to the TRMM patterns. NCEP2 has the largest amount of total precipitation with intense rain along the ITCZ. CFSR produced strong precipitation along the eastern Pacific ITCZ.

The low-frequency CCEWs are relatively well represented in ERA, MERRA, and CFSR, although they have a bias toward the westward direction. The pronounced wave dispersion curves in the spectra of these reanalyses correspond to the TRMM results in the modes of Rossby, MRG, and Kelvin waves. At higher frequencies, however, all the reanalyses have no clear prominent lobes in the spectra, inferring no wave signals. The high-frequency variability in the reanalyses except in CFSR is weaker than in TRMM. Although there is no apparent signal of the convectively coupled IG waves in CFSR, the fraction of high-frequency variance is comparable to TRMM.

CFSR includes many changes since the NCEP2 reanalysis. These include the use of the atmosphere-ocean-land surface-sea ice coupled model with fine horizontal and vertical resolutions, the assimilation of satellite radiances rather than retrievals, and the direct forcing of land hydrology analysis with observed precipitation (Saha et al. 2010). In contrast to CFSR, model-generated precipitation is used for the land forcing in other reanalyses, or pentad precipitation observations are used to nudge soil moisture in NCEP2 (Kanamitsu et al. 2002; Saha et al. 2010). The improvements in precipitation variability in CFSR are likely related to the use of the coupled model with fine resolutions. In addition, improvements of the high-frequency variability and diurnal cycle especially over land suggest that the land surface model changes contribute to the better performance of CFSR. The assimilation of observed precipitation from the daily Climate Prediction Center (CPC) gauge data and pentad CPC merged Analysis of Precipitation (CMAP) datasets seems to have helped the land model performance to become more realistic, and subsequently improved the precipitation product. (Note that the precipitation product in CFSR is still model-derived (Wang et al., 2010).)

Among five reanalyses, MERRA has the most persistent weak rainfall and very red spectrum. Although MERRA's representation of precipitation climatology has been improved compared to ERA and CFSR (Rienecker et al. 2011), the use of the relaxed Arakawa-Schubert scheme in the GEOS v.5.2.0 model for MERRA seems to result in significant lack of higher-frequency variability. Ruane and Roads (2007) have found that the NCEP seasonal forecast model (SFM) reanalysis, which employs the relaxed Arakawa-Schubert convective parameterization, is also strongly biased toward low-frequency precipitation variability. Indeed, it is a general problem that climate and weather prediction models produce overly persistent light rain, resulting in an over-reddened spectrum (Lin et al., 2006; Ruane and Roads, 2007). A more realistic persistence of equatorial precipitation may be achieved by improving subgrid-scale model physics. In nature, convective and mesoscale downdrafts that occur with deep convective updrafts dry the boundary layer and the lower troposphere (Brown and Zhang, 1997; Houze and Betts, 1981; Lin et al., 2006). In consequence, the development and evolution of subsequent convective events are suppressed. The insufficient representation of this self-suppression mechanism in convective processes is considered one of the primary reasons for the persistent weak tropical rainfall with low variance. Lin et al. (2008) have shown that the use of a stronger convective trigger function also improves tropical precipitation variance. The low criterion for triggering convection entails the initiation of convection easily and generates the drizzling type of precipitation, which in turn contributes to the small variance and over-reddened spectrum.

In addition to the enhancement of the tropical precipitation variance, properly generating spectral peaks associated with CCEWs is also important to simulate the tropical climate. Recent studies have revealed that half of the analyzed GCMs have CCEW signals in the low-frequency spectra but the GCM spectra show faster phase speeds than the observed value (Lin et al., 2006). They concluded that effective static stability is not lowered enough by the diabatic heat released by convection in current GCMs. In ERA, MERRA, and CFSR, the phase speeds of low-frequency waves including Rossby, MRG, and Kelvin waves are very close to the speeds observed in TRMM measurements, but not for the high-frequency waves. It seems that ERA, MERRA, and CFSR can reproduce a realistic signal in low-frequency precipitation with the help of data assimilation of the observed state variables. Although precipitation in reanalyses is a model product, the assimilated control variables such as atmospheric temperature, wind, and humidity constrain the model to generate more realistic precipitation than the GCMs, which entirely depend on the model. At the higher frequencies, precipitation would depend more on the model than on observations due to lack of observations. Hence, the deficiency of high-frequency variability and wave signals in reanalyses may be improved by finer-scale observations and improvements in model physics. To properly resolve CCEWs in models, the rainfall type and its resultant vertical heating profile should be properly represented. Studies have shown that climate models underestimate the stratiform-type *top-heavy heating profile*, indicating condensational heating above and evaporative cooling below the melting level (Kiladis et al., 2009; Lin et al., 2004). Misrepresentation of vertical heating profiles would result in inaccurate wave responses, and triggered convection would not be realistic (Ryu et al., 2011).

It is worth of noting that NCEP2 uses a slightly modified version of the simplified Arakawa-Schubert convective parameterization scheme used in NCEP1, but NCEP2 and NCEP1 precipitation differs in many aspects. NCEP2 has enhanced variability and CCEW signals compared to NCEP1, but the phase speeds do not match TRMM presumably due to excessively strong TD-type wave activity in NCEP2. This suggests that the new approach in NCEP2 over NCEP1 is encouraging with respect to resolving equatorial waves and variability, but the model physics still needed to be improved. Unambiguous reasons for the differences in these two reanalyses are not well understood, but it seems that the convective parameterization is not the only important process for correct representation of CCEWs. There have been many attempts to investigate the reasons for lack of CCEWs and precipitation variability in climate models (Frierson et al., 2011; Lin et al., 2008, 2006; Straub et al., 2010; Suzuki et al., 2006). Most studies have concluded that the convective parameterization scheme is the most important factor that determines the existence of CCEW signals in GCMs. Our findings suggest that, along with the convective parameterization scheme, the choice for other model physics such as cloud processes, moist processes in the boundary layer, and the radiation scheme may also play important roles in CCEW activity.

Our understanding and forecasting skill for tropical precipitation processes have been greatly improved due to global observations, advanced models, and growing computer power. This study confirms that the latest reanalyses such as ERA-interim, MERRA, and CFSR have much improved performance in resolving low-frequency CCEWs and precipitation variability over NCEP1 or NCEP2. However, the improved performance in variability are not necessarily accompany with improvements in other skills: CCEW activity and variability are much enhanced in NCEP2 over NCEP1, but the phase speeds are spurious; CFSR shows the best performance in representing diurnal cycle and high-frequency variability, but regional precipitation in the central to eastern Pacific ITCZ is overestimated compared to the western Pacific. Furthermore, the new reanalyses are still very different from observations with respect to variability and CCEW characteristics at high frequencies, meaning deficiencies in short-range forecasts. Since much of tropical precipitation is affected by waves, high-frequency waves should be better represented to produce accurate short-range forecasts. It is hard to determine the relative importance of each factor that interacts with convection in numerical simulations, but we hope that our findings may give useful insights toward understanding the tropical precipitation system and toward improving model physics. Generating realistic precipitation variability especially at high frequencies in global climate models will also indirectly benefit climate prediction by exciting waves that influence feedbacks with the stratosphere.

Chapter 3

A new wave scheme for trajectory simulations of stratospheric water vapor

Small changes in stratospheric water vapor have significant impacts on global climate through radiative feedbacks (Forster and Shine, 2002; Solomon et al., 2010). The main contribution of stratospheric water vapor is the transport due to slow ascent of air in the tropical tropopause layer (TTL) (Brewer, 1949; Fueglistaler et al., 2009). During ascent in the TTL, air parcels can experience extremely cold temperatures and be subsequently dehydrated, called freeze-drying (Brewer, 1949; Jensen and Pfister, 2004). So TTL temperature acts as a regulator of stratospheric water vapor (Fueglistaler et al., 2005; Randel and Jensen, 2013). As well as the mean temperature, variability also plays important roles in the dehydration processes; waves induce anomalously cold temperatures, and temperature fluctuations due to waves determine dehydration efficiency by changing ice particle properties (Jensen and Pfister, 2004; Jensen et al., 2010; Spichtinger and Krmer, 2012). Trajectory simulations using meteorological fields from analysis or reanalysis data have successfully modeled observed stratospheric water vapor at annual and interannual scales (Schoeberl et al., 2012; Fueglistaler et al., 2013). However, there are still big uncertainties related to assumptions on cloud microphysics and temperature and wind fields in reanalyses. Here we identify problems in temperature variability for trajectory models, and suggest a new scheme to reduce uncertainties in the representation of TTL waves.

3.1 Data and Method

Temperatures over 1997-2013 were taken from 24 radiosondes in the tropics between 15°S-15°N. High vertical resolution radiosonde data at fixed locations with 12-hourly profiles provide good wave information for highly variable TTL temperatures with frequencies up to 1 CPD. Raw radiosonde temperature measurements were thoroughly inspected to remove spurious data, and interpolated to a vertical grid of 200 m. Since we are interested in variability associated with waves, we use temperature anomalies from the time-mean at each vertical grid. Thus mean temperature adjustments of inhomogeneous radiosonde data are not required in this study.

To study temperature variability in reanalyses we used ERA-interim (Dee et al., 2011) and MERRA (Rienecker et al., 2011). Although we mostly present ERA results here, our findings about variability problems and improvements with our new scheme are similar in ERA and MERRA. We have sampled reanalysis temperatures at the 24 tropical sites to compare with radiosonde observations.

In the following section, we compare variability differences between radiosonde observations and linearly interpolated temperatures from ERA. Interpolating temperatures in the vertical coordinate is a necessary procedure of trajectory calculations (Jensen and Pfister, 2004; Liu et al., 2010; Schoeberl and Dessler, 2011; Fueglistaler et al., 2013). The vertical resolution of model levels near the TTL in current reanalyses is about 1.2 km. It takes about 30 days for an air parcel to travel this distance with the ascent rate of $0.5\ \mathrm{mm\ s^{-1}}$, typical in the TTL. We investigate temperatures at interpolated levels as well as at reanalysis model levels. We follow the same procedure of linear interpolation for reanalysis temperatures in the vertical coordinate, and compare the results with radiosonde variability. Then we apply a new approach, and see improvements in variability. The details of the new method will be described in section 3.3.

3.2 Diagnosis

Figure 3.1a shows an example of the vertical profile of the standard deviation of temperature anomalies in boreal wintertime, December-January-February (DJF) from radiosondes (black) and ERA. Results are averaged over four radiosondes in the western Pacific (Koror, Chuuk, Ponape, and Majuro) for 1997-2013. The blue curve is calculated from ERA with linear interpolation of temperatures in the vertical coordinate, which is the common way of using reanalysis temperatures in current trajectory simulations. Dotted lines represent ERA model levels. The black and blue curves reveal two main problems in temperature variability.

First, waves are underrepresented at reanalysis pressure levels. Power spectra at the model levels of 96 hPa (Figure 3.1b) and 80 hPa (Figure 3.1d) show additional information on deficiency of waves in ERA. The ERA frequency spectra at the two pressure levels perfectly match radiosonde results at frequencies lower than 0.1 CPD marked by green dotted lines, which means waves with periods longer than 10 days such as Rossby and Kelvin waves are well resolved in ERA. The main contribution of the variability deficiency is for waves shorter than 10 days. These waves have weaker magnitudes of Fourier coefficients by about 20, 44, and 26% relative to radiosondes at 96, 88, and 80 hPa, respectively.

A second problem is seen at interpolated vertical levels. The blue curve in Figure 3.1 clearly shows that linear interpolation substantially degrades variability. This problem is also found with other interpolation methods such as quadratic and cubic spline. Moreover, the cubic spline method tends to give unrealistically cold temperatures at interpolated levels. Figure 3.1c shows higher-frequency wave amplitudes in ERA are only half of observed values. Moreover, even low-frequency waves such as Rossby and Kelvin waves, which are well represented at model levels, are damped due to interpolation.

The reason for this wave damping is explained in Figure 3.2. Suppose monochromatic wave-type temperature anomalies with opposite phase are observed in two adjacent reanalysis pressure levels. The horizontal axis in Figure 3.2a would be considered as the time or horizontal coordinate

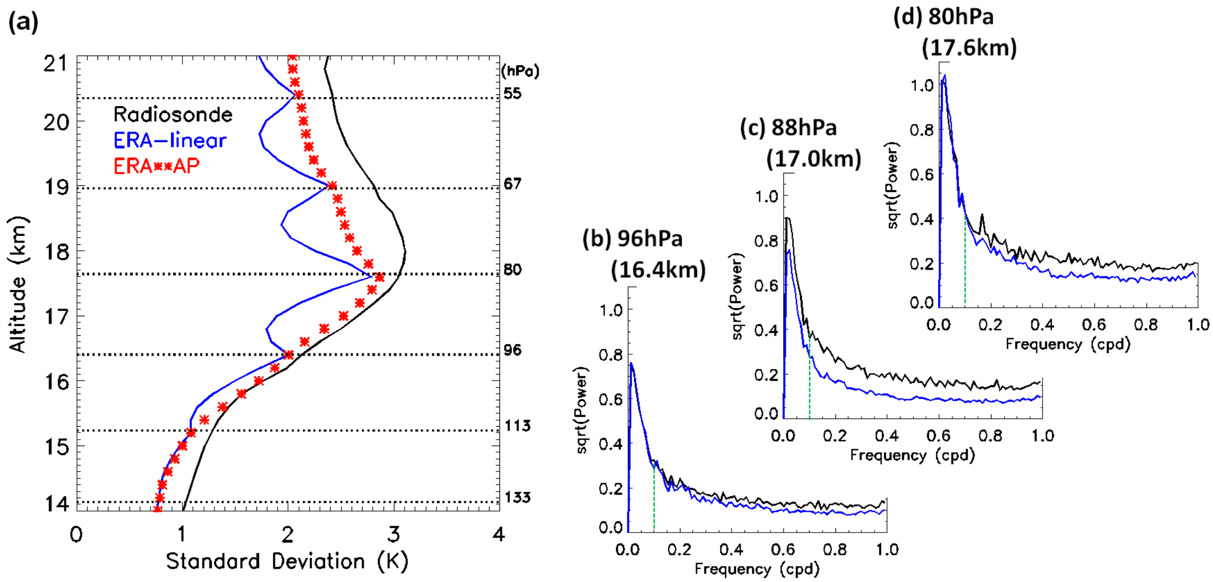

Figure 3.1: (a) Vertical profile of the standard deviation for temperature anomalies in DJF. The profile is averaged over four radiosondes in the western Pacific over 1997-2013. The black curve is for radiosonde observations, and ERA-interim results are the blue curve and red asterisks. The blue is based on linear interpolation and red asterisks are calculated from amplitude-phase interpolation. Dotted lines represent ERA model pressure levels, and we use the log-pressure altitude for both datasets. Frequency power spectra (as square root) were calculated at the pressure (b) 96 hPa, (c) 88 hPa, and (d) 80 hPa. Black curves are radiosonde results. The blue curves in (b) and (d) are power spectra at ERA model levels, and the blue in (c) is calculated from linearly interpolated ERA temperatures. Green dotted lines mark 0.1 CPD.

in real space. It may be reasonable to assume that observed temperature anomalies at the two levels are affected by the same wave, propagating vertically and maintaining its coherent structure. Then the temperature anomaly between the two levels should have the same amplitude and in-between phase as shown in the left in Figure 3.2a. In contrast to this expected temperature anomaly in the middle layer, simple interpolation of temperatures in real space does not see the existence of the wave. As a result, temperature anomalies at two pressure levels are cancelled out in the middle due to the phase difference, shown in the right in Figure 3.2a. The difference between the left and right in Figure 3.2a can also be illustrated in the complex plane in Figure 3.2b. The points of z1 and z2 represent amplitudes and phases of waves at two reanalysis levels. Linear interpolation corresponds to the mid-point L between z1 and z2 in the complex plane. On the other hand, interpolating amplitudes and phases of two complex numbers of z1 and z2 corresponds to the point AP. If the phase difference between z1 and z2 is small, L will be close to AP. This means linear interpolation is enough for waves having sufficiently long vertical wavelengths relative to the vertical resolution. However, the linear interpolation method is not appropriate for systems with non-negligible wave activity at spatial/temporal scales close to the data resolution limit. Tsuda et al. (1994) have shown that the distribution of the vertical wavelength from observed waves in the TTL is 1-4 km with higher occurrence of 2-3 km, which is close to the reanalysis vertical resolution limit of ERA and MERRA. This supports our interpretation of how linear interpolation dampens wave amplitudes in the TTL in the current reanalyses.

3.3 New wave parameterization: amplitude-phase (AP) interpolation + amplification

Now that we understand how anomalies should be represented in-between reanalysis levels from the discussion above, we apply the idea on the left in Figure 3.2a and the AP point in Figure 3.2b. We define the following step as amplitude-phase (AP) interpolation. We perform the Fourier transform for a 90-day time series of temperature anomalies at each reanalysis pressure level. Reanalysis temperatures were taken at 0 and 12Z to match radiosonde data availability. Then

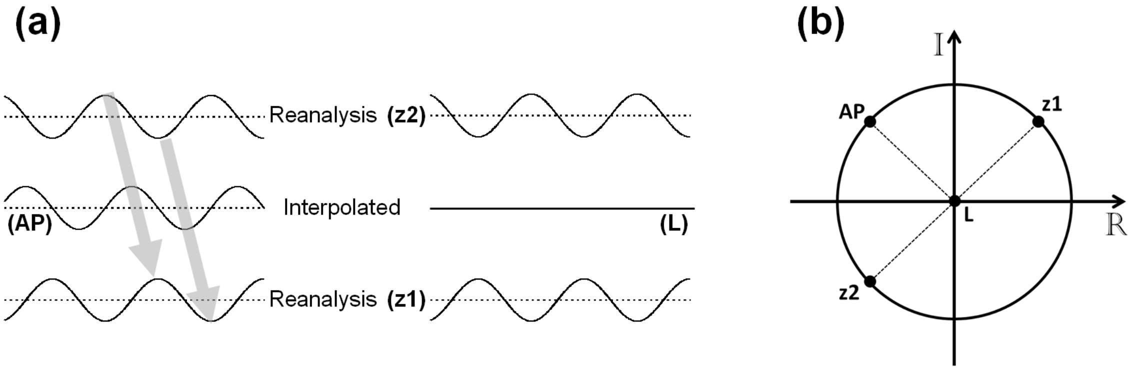

Figure 3.2: (a) Schematic of amplitude-phase interpolation (left: AP) and linear interpolation (right: L) from the existence of wave signals at two reanalysis levels of z1 and z2. Suppose two signals have the same amplitude and opposite phase. The horizontal axis may be considered as time or a horizontal direction in real space. The vertical axis corresponds to the vertical pressure coordinate. Thick gray arrows represent downward phase propagation of a wave. (b) Complex plane representation of amplitude-phase interpolation (AP) and linear interpolation (L) between two complex numbers of z1 and z2.

amplitudes and phases of complex Fourier functions at reanalysis vertical levels are interpolated into finer scale 200 m vertical grid bins to compare with radiosonde. After performing the back transform at each finer vertical grid point, we get much enhanced variability depicted by red asterisks in Figure 3.1.

Although amplitude-phase interpolation gives better representation of waves, this method alone does not generate enough variability relative to radiosonde results since waves are already weaker at reanalysis levels as pointed out in section 3.2. So we have amplified amplitudes of the complex functions to match the radiosonde power spectrum before performing the reverse transform. We define the amplification factor as the fractional difference between the square roots of power spectra from radiosonde and reanalysis data. The amplification factor was calculated at each vertical grid and frequency (Figure 3.3a-b). This way we can boost waves more where waves are less represented. The amplification factors were calculated based on statistics of 16-year data at 24 tropical radiosondes. We have found that the amplification factors are similar regardless of region and season within the same dataset. It appears that a reanalysis model generally captures regional and seasonal changes in wave activity with similar deficiency, suggesting there is model consistency in representing waves within the same model. This is particularly true for ERA, but MERRA shows regional variability in amplification factors. As shown in Figure 3.3 ERA has higher amplification factors over all frequencies, indicating temperature variability in ERA is slightly weaker than MERRA. Amplification factors in MERRA show small negative values at the low frequency range (< 0.1 CPD), suggesting these waves are slightly overestimated in MERRA compared to radiosonde results. Amplification factors for both datasets show that higher frequency waves need to be enhanced more than lower frequency waves except near the diunal frequency of 1 CPD.

3.4 Improvements

Probability distribution functions (PDFs) in Figure 3.4 show improvements in temperature anomalies at the interpolated level of 17.0 km (88 hPa) in ERA (Figure 3.4a) and at 17.8km (79 hPa,

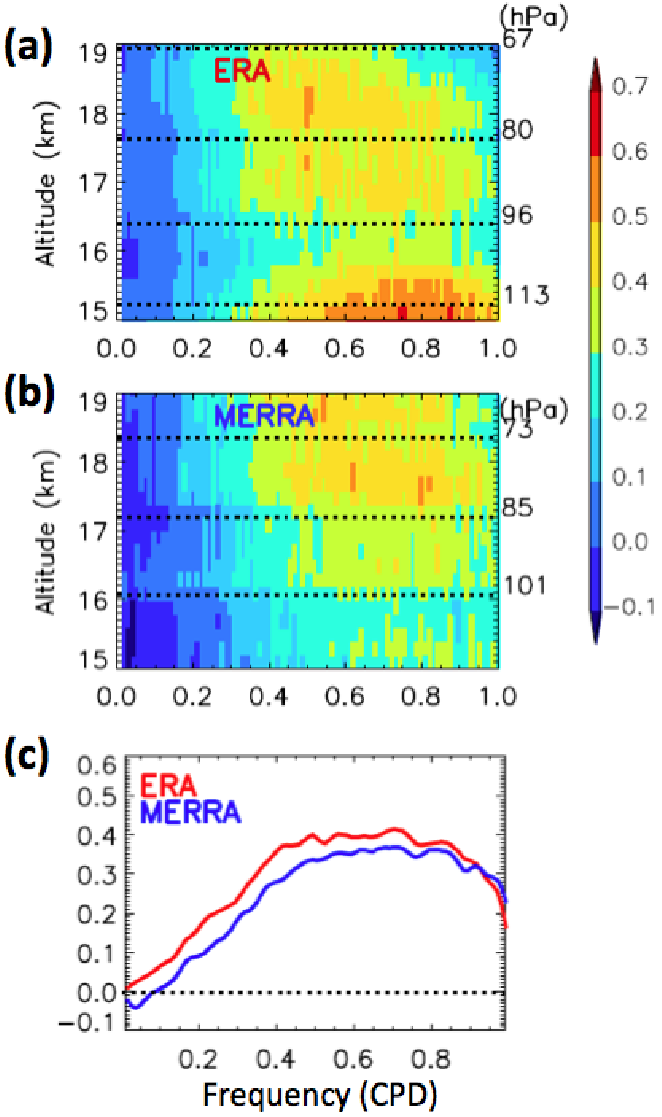

Figure 3.3: Amplification factor as a function of frequency and height in (a) ERA and (b) MERRA. (c) Average amplification factors between 15-19 km for ERA and MERRA.

a midpoint between levels) in MERRA (Figure 3.4b). The black line is for radiosonde observations and the blue is for the PDF calculated from reanalysis temperatures with linear interpolation. The incorporation of the new wave scheme with amplitude-phase interpolation and amplification has generated the red PDFs. Top panels are for total temperature anomalies, and lower four panels show results for different frequency bands. As expected from Figure 3.1, the blue PDFs from conventional linear interpolation in Figure 3.4 show weaker amplitudes at all frequencies even at longer scales. At the high-frequency scale with periods shorter than 3 days, the 99th percentile of linear interpolated ERA anomalies at 17.0 km is only 2 K, while the 99th percentile of radiosonde measurements is 4 K. PDFs in Figure 3.4 and power spectra in Figure 3.1c imply that amplitudes of high-frequency waves from ERA are only about half of realistic values at interpolated TTL layers. About 13% of the high-frequency anomalies from radiosonde observations have amplitudes higher than 2 K, which indicates a significant lack of higher-frequency waves in the reanalyses. The red PDFs in Figure 3.4 show improvements in wave amplitudes at all frequency bands. The good agreement between PDFs of radiosondes and the new scheme suggests that the new scheme can generate realistic wave intermittency as well as variability.

An example shown in Figure 3.5 clearly illustrates how ERA temperature fields were changed after applying the new method. Figure 3.5a-c are time-height sections of temperature anomalies for December 2012 - February 2013 at 171°E, 7°N from the Majuro radiosonde (a), ERA with conventional linear interpolation (b), and ERA with the new scheme (amplitude-phase interpolation followed by wave amplification) (c). The black line across the time series represents the cold point tropopause. Values of the mean cold point temperature (CPT), tropopause height (CPH), and tropopause pressure (CPP) are in the lower left corner of the plots. The new wave scheme has made fine-scale features in ERA temperatures more prominent with enhanced amplitudes similar to radiosonde anomalies. Temperature and tropopause height fluctuate as they are affected by waves as seen in radiosonde observations in Figure 3.5a. Due to the limitation of the vertical resolution and linear interpolation, the tropopause of ERA in Figure 3.5b can only occur at ERA model pressure levels. In Figure 3.5c, the new wave scheme has produced similar tropopause height fluctuations

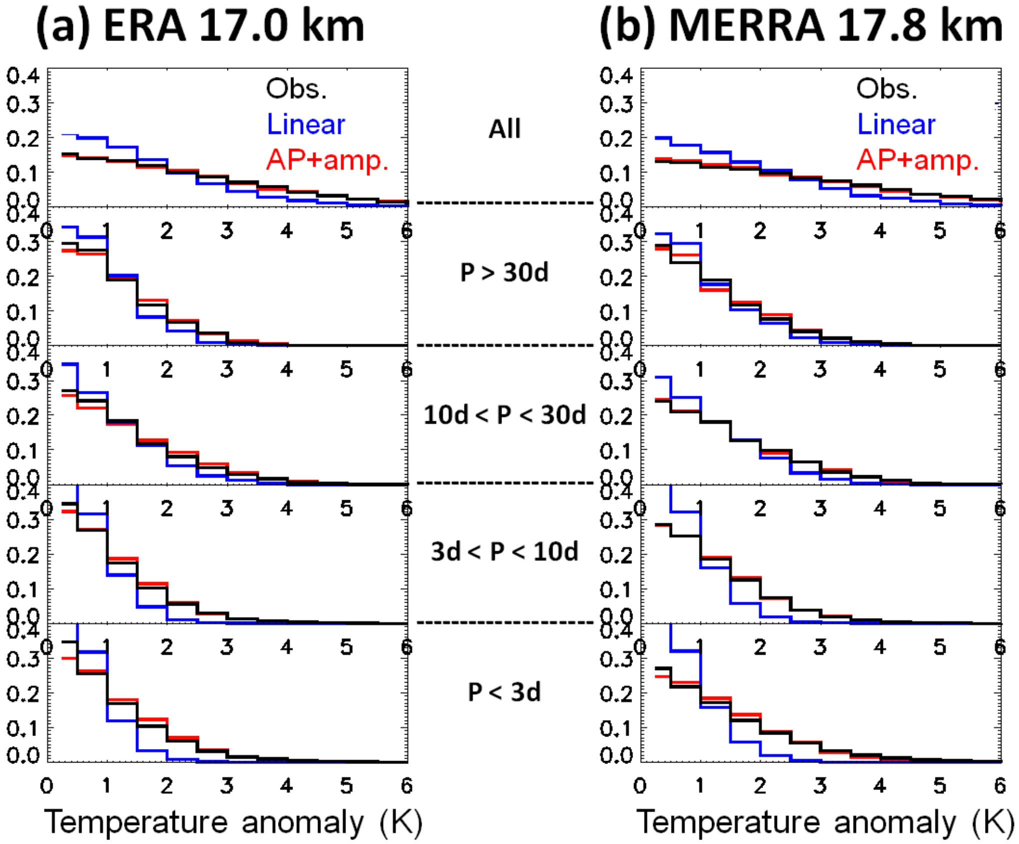

Figure 3.4: Probability distribution functions (PDFs) from temperature anomalies at interpolated vertical levels in (a) ERA 17.0 km and (b) MERRA 17.8 km for 1997-2013 DJF at four western Pacific radiosonde locations. Top panels are total anomalies, and lower panels show PDFs at different frequency bands, including ranges of 30-90, 10-30, 3-10, and <3 days. Colors represent radiosonde (black), linear interpolation (blue), and the new scheme (red) results.

to the radiosonde result in Figure 3.5a, by allowing ERA temperatures to have more realistic waves throughout all vertical layers. Furthermore, the wave scheme decreases the mean CPT and raises CPH without changing the average temperature profile in ERA, simply by improving the representation of the wave variability. The drop of the CPT potentially has a significant effect on stratospheric water vapor. Jensen and Pfister (2004) have shown that the final TTL mixing ratio is reduced by 0.4 ppmv due to the wave-driven decrease in the tropical average minimum temperature by 0.75K . Schoeberl and Dessler (2011) have also found decreased stratospheric water vapor by 0.2 ppmv by giving temperature perturbations driven by a single-frequency wave with amplitude of 0.8 K.

While radiosonde data are only available at limited locations, COSMIC GPS data provide temperatures in the whole tropics. We gridded the GPS data to calculate variability. Figure 3.6a shows standard deviation of temperature at 17 km in GPS. Linearly interpolated ERA temperatures at 17 km are sampled like GPS profiles, and standard deviation is plotted in Figure 3.6b. Figure 3.6c confirms that the new wave scheme can reproduce very similar temperature variability to that observed in GPS over the whole tropics. Furthermore, Figure 3.7 shows that stronger waves in the dataset with the wave scheme lower cold-point temperatures by about 1-2 K relative to ERA. So the warm bias in cold-point temperature in ERA in Figure 3.7b was reduced by allowing more temperature variability in Figure 3.7c. We note that the mean temperature is the same in Figure 3.7b and c.

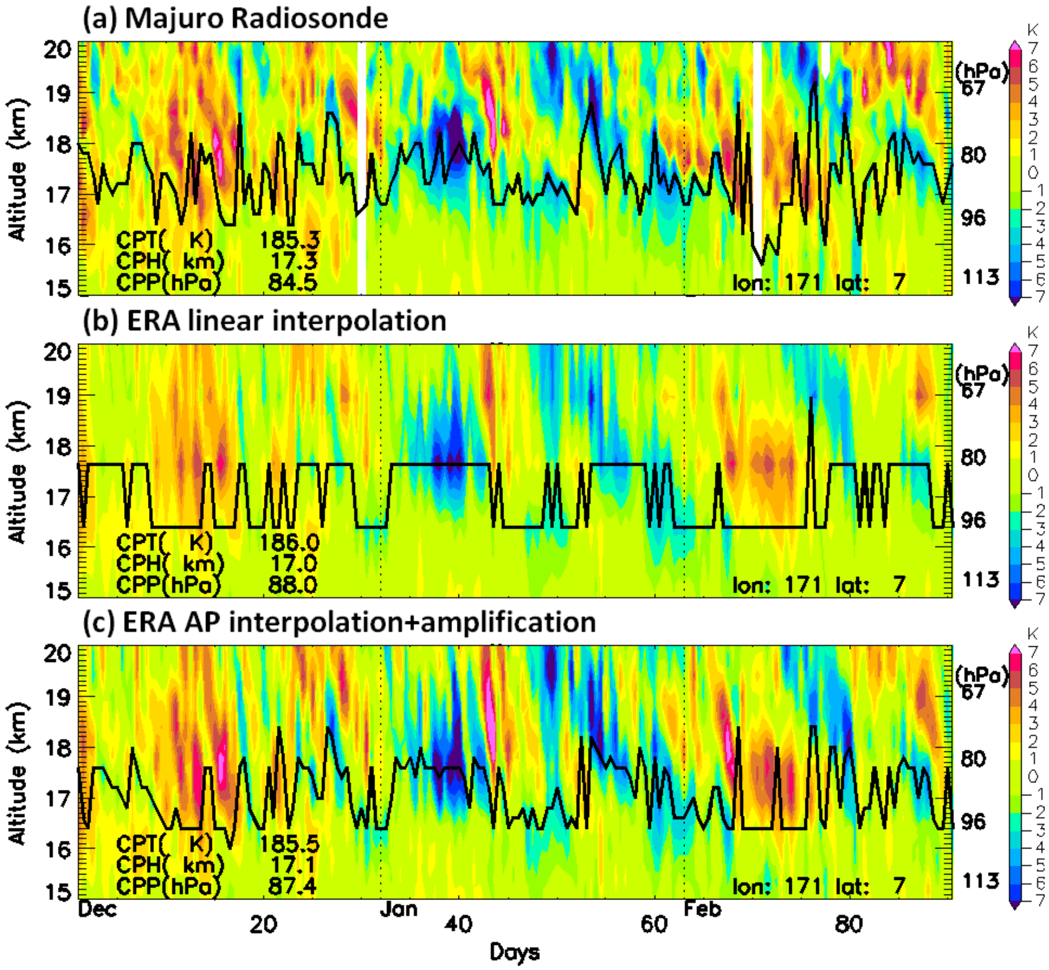

Figure 3.5: Time-height sections of temperature anomalies for December 2012 - February 2013 at 171°E, 7°N from (a) Majuro radiosonde observations, (b) ERA with linear interpolation, and (c) ERA with our new wave scheme including amplitude-phase interpolation and amplification of waves. The horizontal curve indicates cold point tropopause. CPT, CPH, and CPP represent the mean cold point temperature, tropopause height, and tropopause pressure, respectively. Numbers in the right side of the vertical axis show ERA vertical level pressures in hPa.

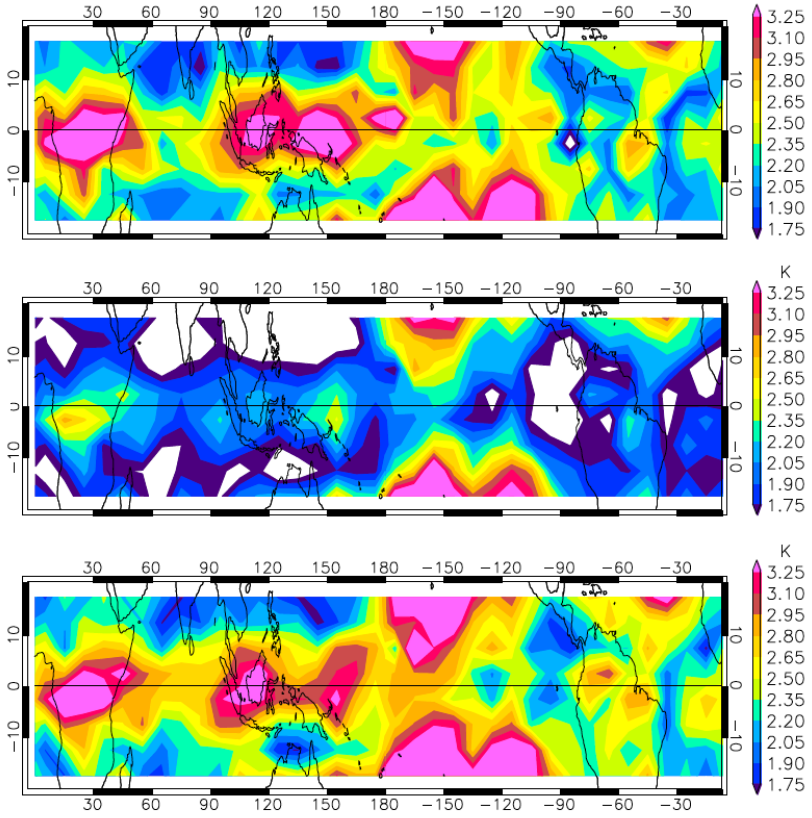

(a) COSMIC GPS obs.

(b) ERA linear interpolated at 17km

(c) ERA + New scheme

Figure 3.6: Standard deviation for temperature at 17 km for December 2012-February 2013 estimated from (a) COSMIC GPS, (b) linearly interpolated ERA-interim data (Note that this level is approximately in the middle of two model levels in ERA-interim.), (c) new ERA-interim data having overenhanced waves by our method. All temperature data used in (b) and (c) are sampled the same way as GPS temperature profiles used in (a).

(a) COSMIC GPS obs.

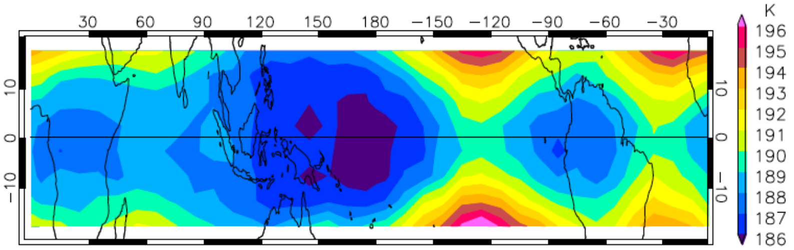

(b) ERA

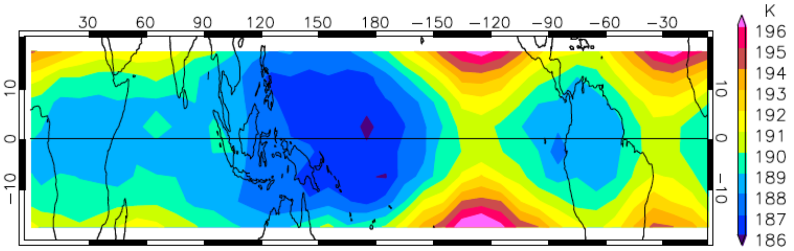

(c) ERA + New scheme

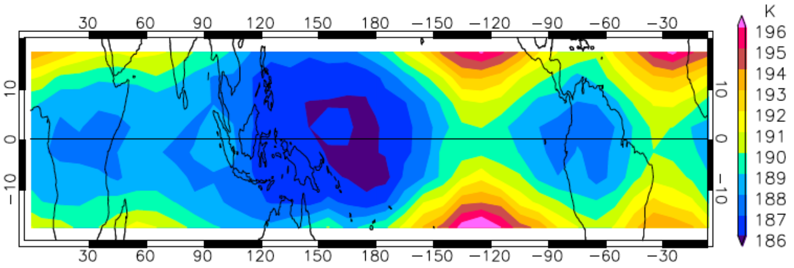

Figure 3.7: Cold-point temperatures for December 2012-February 2013 from (a) COSMIC GPS, (b) ERA-interim, (c) ERA-interim with enhanced waves by our method. The cold-point temperature is calculated by averaging coldest temperatures from individual temperature profiles at each horizontal location. Note that all temperature data used in (b) and (c) are sampled the same way as GPS temperature profiles used in (a).

3.5 Summary and discussion

To provide better temperature data for trajectory simulations of stratospheric water vapor, we diagnose problems in temperature variability in reanalyses. We have found that temperature variability is lacking in reanalyses near the TTL and above. Also, variability significantly drops where temperatures are interpolated in the vertical coordinate. We propose a new wave parameterization scheme to overcome the two main problems in temperature variability: weaker variability and damping of waves due to interpolation. The two main components of the new scheme are (1) amplitude-phase interpolation and (2) amplification of waves in Fourier space. We note that this approach has an intrinsic assumption that current reanalyses contain reliable waves to some degree although their amplitudes are relatively weak. Since we use information on the weakly resolved waves in the reanalyses, this assumption must be satisfied. It turned out this is true for current reanalyses at frequencies lower than 1 CPD for both ERA-interim and MERRA; considerable improvements in the wave representation after incorporating our method support it. Statistics on PDFs and an example of a time-height section of temperature anomalies prove that our new scheme gives very realistic wave amplitudes and lowers cold point temperatures with increased tropopause heights. Changes in these fields will have important implications for modeling results in stratospheric water vapor.

Although we present results only for temperature variability particularly designed to enhance wave representation for trajectory simulations, the new wave scheme may have broader applications in various studies on systems where waves are important. The same concepts of amplitude-phase interpolation and amplification can be applied to horizontal winds. The amplitude-phase interpolation method for winds will improve the dynamical consistency at levels between model levels. It should be reasonable to amplify waves for wind components using analogous frequency-dependent amplification factors as developed for temperatures to retain dynamical consistency with temperature. Winds affect trajectory transport pathways, so having stronger waves in modeling may result in different behavior of air parcels depending on wave types, spatio-temporal scales, and amplitudes relative to background winds. Possible changes in parcel pathways due to waves may bring changes in stratospheric water vapor, since air parcels are more efficiently dehydrated if they encounter colder temperatures in the western Pacific cold trap (Holton and Gettelman, 2001). Furthermore, the geographical distributions of convection and vertical transport rates due to radiative heating are not zonally symmetric. This means the age of stratospheric air has strong path dependence, and consequently changes in the transport path will affect the abundance of chemical constituents in the stratosphere (Bergman et al., 2012). Another possible application may be for nudging of meteorological fields in models toward reanalyses or observations. Nudging with linearly interpolated meteorological fields may reduce input variability into models and may also tend to suppress model-generated waves. Amplitude-phase interpolation may give more realistic nudging fields, so that mesoscale or high time resolution models will have better wave responses.

Chapter 4

Direct impacts of waves on tropical cold-point tropopause temperature

4.1 Introduction

Air passing throught the TTL gets dehydrated due to extreme cold temperatures. Althogh the stratosphere is much drier than the troposphere, a small amount of stratospheric water vapor has significant radiative impacts on surface climate. A study has shown that about a 10% decrease in stratospheric water vapor at the end of 2000 contributed to slowing the rate of global surface warming by about 25% compared to what was expected only by increased well-mixed greenhouse gases(Solomon et al., 2010). Stratospheric water vapor content is strongly correlated with cold-point temperature (CPT) in the TTL (Randel et al., 2004; Fueglistaler and Haynes, 2005; Randel, 2010; Randel and Jensen, 2013). Observations show that a sudden drop in CPT also occurred around the same time as the sudden drop in stratospheric water vapor (Randel, 2010; Randel and Jensen, 2013). These studies underline the importance of understanding mechanisms regulating CPT as a key to understanding stratospheric water vapor and its impact on global climate.

The mean temperature structure of the TTL is determined by radiation, convection, and adiabatic cooling due to upwelling (Fueglistaler et al., 2009; Highwood and Hoskins, 1998; Gettelman and Forster, 2002; Sherwood and Dessler, 2000; Fu, 2013; Grise and Thompson, 2013). Indeed studies have found that the sudden drop in CPT and stratospheric water vapor around the year 2000 is associated with an increased eddy forcing (Randel et al., 2006; Fueglistaler, 2012), indicating stronger mean tropical upwelling as a part of the Brewer-Dobson circulation. The studies, however, have revealed that the estimated increase in upwelling is not enough to be responsible for such a big drop of stratospheric water vapor, and a missing contribution to the drop has remained unknown. Also a trajectory study attempted to simulate water vapor over the last 3 decades with various efforts to correct biases in reanalysis mean temperatures (Fueglistaler et al., 2013). The trajectory simulations well reproduce annual to interannual variations in stratospheric water vapor, but the magnitude of the decadal change, in particular the drop in 2000, is weaker than satellite observations. These results suggest that, in addition to changes in the mean temperature associated with the mean upwelling, there might be another cause for the decadal change in CPT, which might not be well represented in reanalysis data.

So, here, rather than the traditional approach looking at changes in the mean, we consider changes in variability from observations in the tropical western Pacific where CPT has a global minimum (Kim and Son, 2012; Fueglistaler et al., 2004; Holton and Gettelman, 2001). Temperature fluctuations by waves give additional coldness to a minimum temperature at a given time. That is, CPT is directly modulated by vertically propagating waves regardless of any changes in the mean upwelling. This is because a cold-point is more sensitive to cold phases of waves than warm phases (see Figure 4.1 and Figure 4.2). To differentiate from the indirect impact referring wave-driven mean upwelling and subsequent cooling of the mean TTL temperature, we call it the direct impact of waves on CPT. The direct wave impact has been appreciated in several studies (Jensen and Pfister, 2004; Pfister et al., 2010; Schoeberl and Dessler, 2011; Kim and Alexander, 2013), but no quantitative analysis has been reported. In this study, we suggest a new way to quantify the direct wave impact. We show that the direct wave impact plays important roles in regulating CPT: waves lower CPT by 1.0-2.2 K in the tropical western Pacific, the decisive region for global stratospheric water vapor (Fueglistaler et al., 2004; Holton and Gettelman, 2001), and the direct impact is partially responsible for the decadal change in CPT and stratospheric water vapor.

4.2 Data

Temperatures over June 1990-May 2014 were taken from 5 radiosondes in the equatorial western Pacific including Koror (134°E, 7°N), Yap (138°E, 9°N), Chuuk (152°E, 7°N), Ponape (158°E,

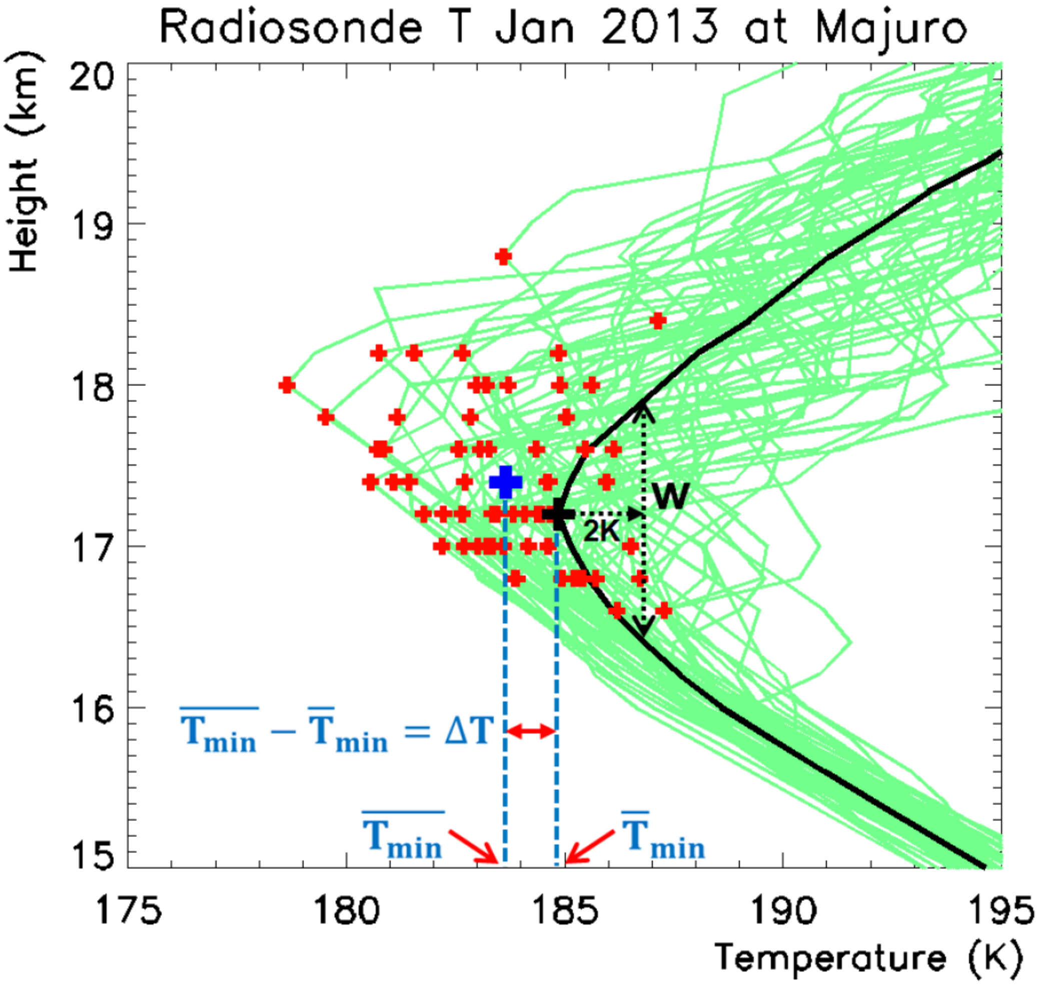

Figure 4.1: Temperatures for January 2013 from Majuro (171°E, 7°N) radiosonde. Black thick line is the mean temperature profile and green lines are all individual profiles. Red symbols are cold-point tropopauses from individual profiles. The black symbol is the coldest point of the mean temperature and the blue symbol is the average of all red symbols, that is, the blue is the mean of cold-point tropopauses. ΔT is the difference between the blue and black symbol. The TTL width w in this study is defined by the distance between the higher and lower points where the mean temperature is warmer by 2 K than $\overline{T}_{min}$.

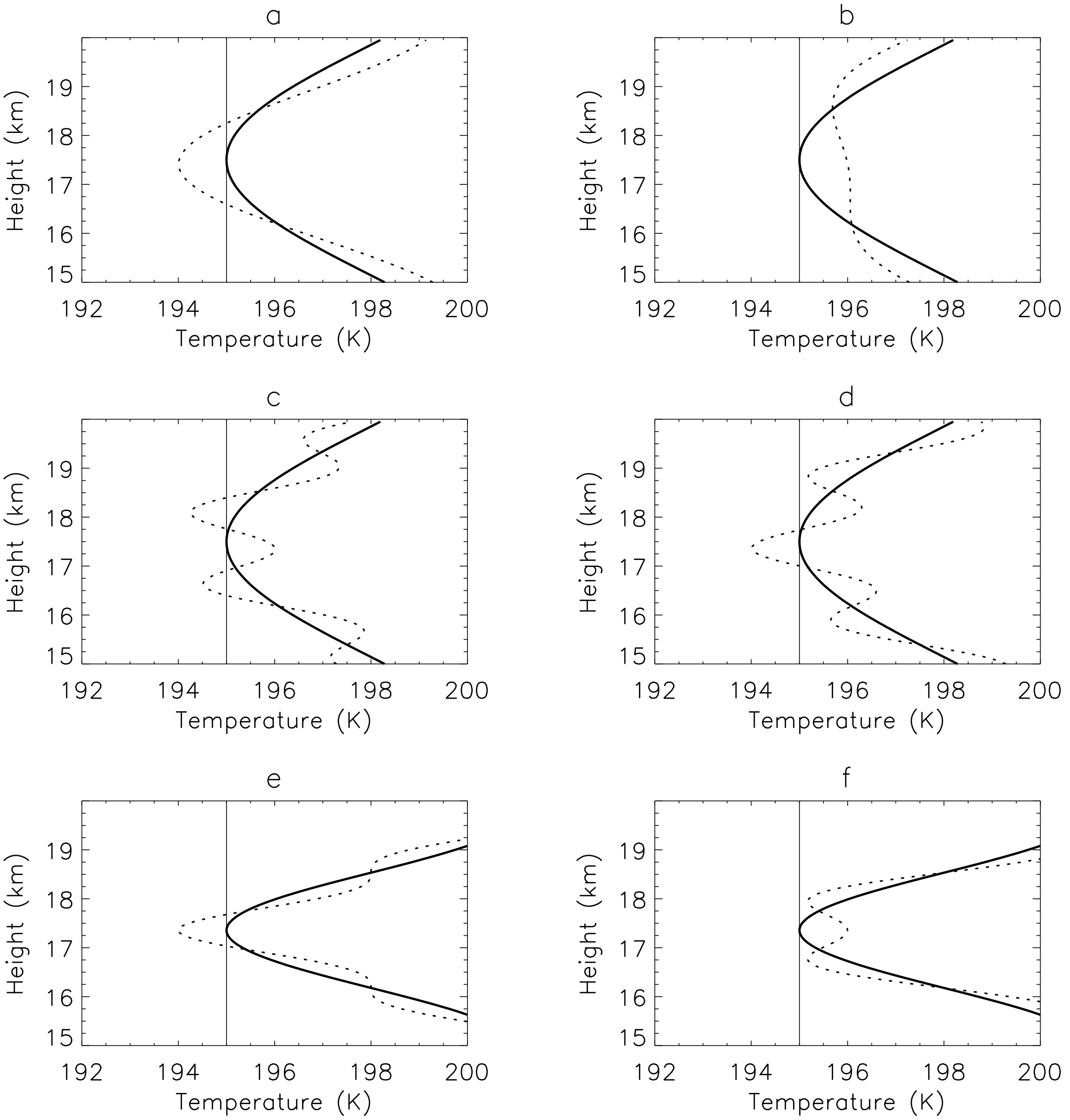

Figure 4.2: Idealized examples showing how waves affect CPT. Thick lines are the mean profile, and dotted lines are perturbed temperatures. (a-d), Comparison of a long and short vertical wavelength for the same mean TTL width. A wave with a long wavelength relative to the mean structure induces colder (a) or warmer (b) CPT depending on the phase, so the net effect is not significant in (a) and (b). In contrast, a wave with a short wavelength relative to the mean structure always makes CPT colder, resulting in the colder mean CPT in (c) and (d). (c-f) Comparison of the same vertical wavelength for the wide and sharp mean TTL width. The TTL width is too sharp to lower the mean CPT effectively in (e) and (f).

7°N), and Majuro (171°E, 7°N). Data from these radiosondes provide 12-hourly measurements giving wave frequency information up to 1 cycle per day at the fixed locations. Raw temperature profiles were carefully inspected and spurious data were removed. An average vertical resolution of measurements is 300-500 m in the TTL (see Supplementary.). Raw vertical profiles are interpolated onto a 200 m grid.

We also used COSMIC GPS radio occultation data. While radiosonde measurements are regular in time at a fixed point, GPS measurements are random in space and time. So we have gridded GPS data at $15^\circ \times 5^\circ$ in longitude and latitude to calculate the mean temperature profile.

4.3 Results

4.3.1 Definition of the direct wave impact

The concept of the direct wave impact on CPT is depicted in Figure 4.1 using temperature profiles (green lines) at Majuro radiosonde at 171°E and 7°N in January 2013. The coldest points of these individual measurements are depicted by red symbols. Taking the mean of all red symbols results in the blue symbol which is defined by $\overline{T_{min}}$, the mean of the cold points from individual profiles. The black line is the averaged temperature profile of individual green lines. The black line gives the coldest of the mean, $\overline{T}_{min}$, represented by the black symbol. This example shows that the mean of cold-points $\overline{T_{min}}$, blue symbol) is colder than the coldest point of the mean temperature ($\overline{T}_{min}$, black symbol) because waves give temperature fluctuations. This example also shows that temperature perturbations due to waves raise the mean tropopause height as well as lower the mean tropopause temperature. To quantify this direct impact, we define ΔT as the difference between $\overline{T}_{min}$ and $\overline{T_{min}}$ as shown in Figure 4.1.

4.3.2 Wave impacts from different frequencies

The direct wave impact can also be understood with Fourier-decomposed temperature perturbations in Figure 4.3. The colors indicate temperature perturbations of radiosonde temperatures at Majuro for December 2012-February 2013. The perturbations are calculated at each vertical grid. Black lines correspond to CPT tropopauses, and mean values of CPT are displayed in the figures. Higher frequency waves are gradually added from Figure 4.3a to Figure 4.3e using filtered spectral analysis. As more waves are added to the mean structure, CPT and tropopause height are modulated. The mean CPT gets colder by having more waves. In this example, ΔT is the difference between the CPT values in Figure 4.3a and Figure 4.3e, as the CPT in Figure 4.3a corresponds to $\overline{T}_{min}$ and the CPT in Figure 4.3e corresponds to $\overline{T_{min}}$ from observed temperatures including all waves. Thus the resulting ΔT is -1.7 K. In the same way, we have calculated ΔT by adding higher frequency waves to the mean temperature structure at 5 tropical radiosondes for each 90-day time segment over 1990-2014. Black squares in Figure 4.4 show that TTL waves, on average, lower CPT by about 1.6 K contributed by a broad spectrum of waves compared to a calculation based on 90-day time-mean temperature. Based on the study of the relationship between the cold point and water vapor (Randel et al., 2004), the change of -1.6 K corresponds to a change in entry water vapor of approximately -1 ppmv. Given the average entry value of about 3.85 ppmv (Dessler and Kim, 1999; Fueglistaler et al., 2005), we can conclude waves in the TTL reduce the concentration of water vapor in air entering the stratosphere by ~25%.

4.3.3 Wave impacts at annual to decadal time scales

Figure 4.5 shows the evolution of the direct wave impact ΔT over June 1990-May 2014. An individual ΔT is calculated for 90-day time segments for each season consisting of December-January-February (DJF), March-April-May (MAM), June-July-August (JJA), and September-October-November (SON). While the mean ΔT is about -1.6 K, it varies significantly annually and interannually, ranging from about -1 K to -2.2 K. As shown in Figure 4.5 with colored dots denoting the seasons, ΔT does not have a clear seasonal cycle, although SON tends to have the largest |ΔT| and MAM tends to be the smallest. DJF shows the biggest spread in ΔT giving year-to-year differences up to about 0.7 K. The orange line in Figure 4.5 is obtained from COSMIC GPS radio occultation data. The GPS ΔT is an average over the grids near the 5 western Pacific

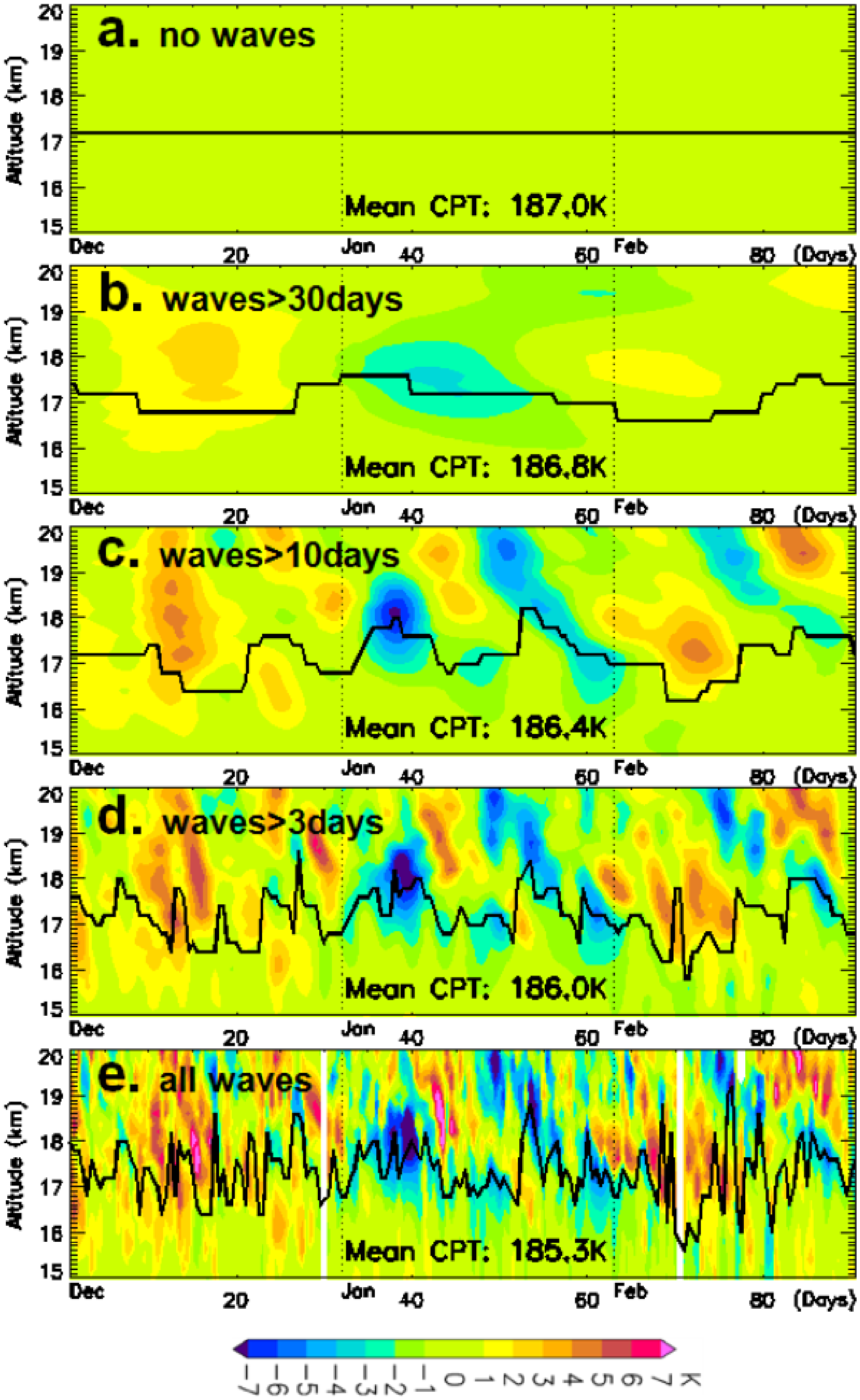

Figure 4.3: Time-height sections of temperature anomalies for December 2012-February 2013 at 171°E, 7°N from Majuro radiosonde observations. The horizontal thick black curve indicates the cold-point tropopause. Higher frequency waves are gradually added from (a), the mean temperature structure. All values should be zero in a because colors are perturbations from the mean temperature profile. Temperature perturbations with Fourier-filtered waves longer than 30 days (b), 10 days (c), and 3 days (d). All waves observed by the radiosonde are included in (e). The mean CPT temperature for each case is listed on the bottom of each panel.

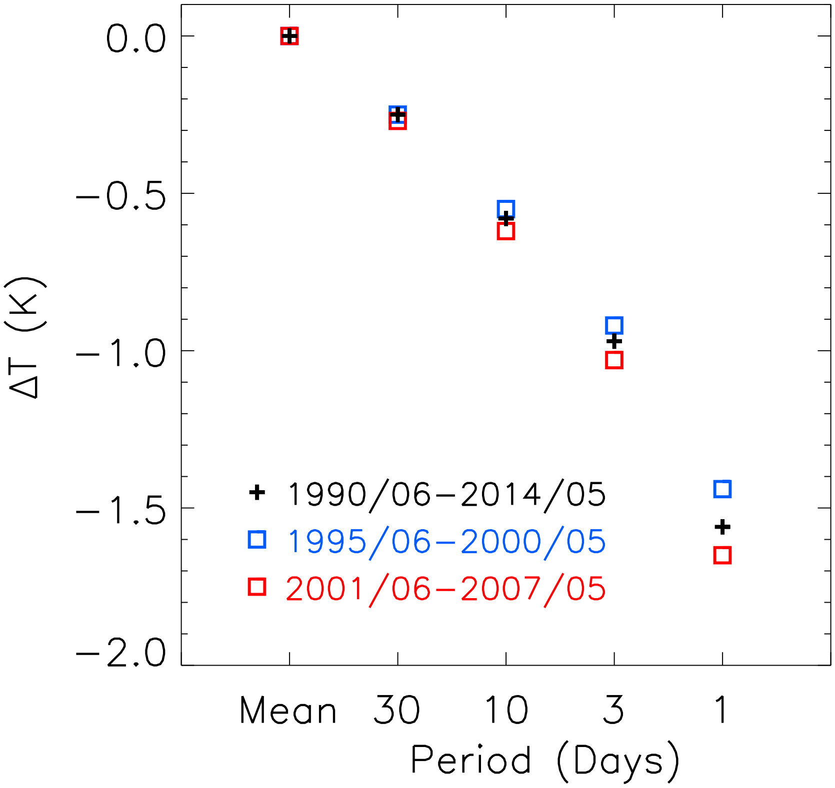

Figure 4.4: Changes in ΔT by adding higher frequency waves. Values are averaged over all seasons and 5 radiosonde sites for June 1990-May 2014 (black). The 90-day time-mean temperature profile corresponds to ΔT of zero, and adding disturbances longer than the period of 30, 10, 3, and 1 day(s) on the x-axis results in the corresponding ΔT value on the y-axis. Time periods considered for blue and red symbols are shown in the form of year/month.

radiosonde locations, and the value is shifted by -0.15 K to compare with radiosondes. We note that ΔT averaged in the tropical band between 20°S-20°N shows similar oscillation patterns, but the magnitude of the oscillation is weaker and |ΔT| is smaller than the western Pacific average. ΔT from this different source of observations shows very similar variations to radiosondes, confirming the results for ΔT are robust. Note that there are differences in calculating ΔT between radiosondes and GPS due to differences in data availability (see Methods), yielding a weaker |ΔT| and higher uncertainty in GPS. Due to relatively sparse measurements in the tropics, the GPS calculations do not resolve impacts from waves with shorter horizontal wavelengths. Also differences in ΔT values between radiosondes and GPS come from a coarser effective vertical resolution of GPS observations (Kursinski et al., 1997), limiting the representation of waves with shorter vertical wavelengths.

Interestingly, the thick line of the smoothed 2-year running mean in Figure 4.5 shows that there have been changes in the direct wave impact at a decadal time scale. The running mean of ΔT remains about -1.5 K for 1990-2000 followed by a decrease for a few years. Then ΔT increases around 2005-2010. These changes are very similar to the changes in CPT and lower stratospheric water vapor as shown in Figure 4.6 in Randel and Jensen's study (Randel and Jensen, 2013). The drop in ΔT after 2001 is about 0.2-0.3 K (statistical significance at p-value$\leq$0.025 from Student's t-test) relative to ΔT of years before 2000. This range of the drop in ΔT depends on which years are taken into account. Even though the change of ΔT looks very small, it could modulate water vapor entering the stratosphere because the dehydration process is very sensitive to CPT. One study showed that the significant drop of stratospheric water vapor around the end of 2000 is related to a drop of the mean CPT by about 1 K (Randel et al., 2006). The sudden drop could be attributed not only to the change in the mean temperature induced by increased upwelling, but also to the direct wave impacts. The difference in ΔT from years before and after 2000-2001 is responsible for approximately 20-30% of the total CPT change. Therefore, along with the wave-induced Brewer-Dobson circulation, the direct impact of waves on CPT could be also important for decadal changes in stratospheric water vapor. We further investigate contributions of waves at different frequencies to the change in ΔT around 2000. In Figure 4.4, blue corresponds to the average ΔT for June

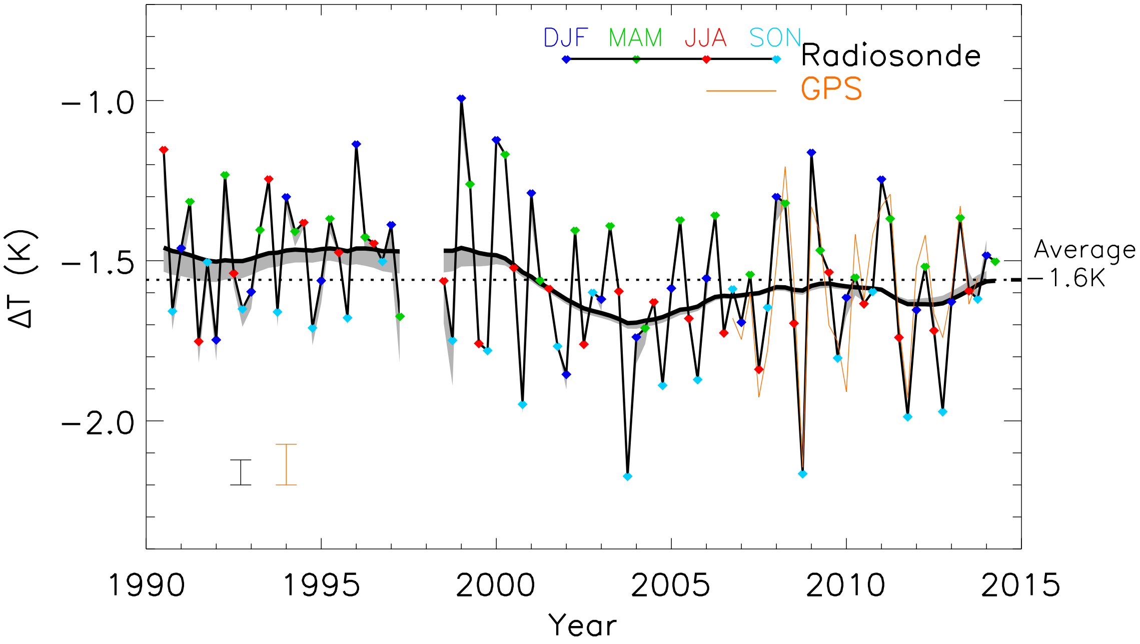

Figure 4.5: Time series of direct wave impacts averaged over 5 equatorial western Pacific radiosondes (thin black line with colored dots). Black thick line is the smoothed 2-year running mean with the shade representing a possible bias due to differences in vertical resolution of raw observations over the years. Descriptions of the bias estimation can be found in Supplementary. The orange line is calculated using COSMIC GPS temperatures near the 5 radiosonde sites. GPS ΔT is shifted by -0.15 K to compare with radiosondes (see text). Values for June 1997-May 1998 were omitted due to poor data quality. The error bars on the bottom left correspond to the averaged standard error for radiosonde (black) and GPS (orange) observations. Note that changes in the standard error of radiosondes are negligible over the years.

1995-May 2000 and red is for June 2001-May 2007. The difference between red and blue squares gradually increases as higher frequency waves are included. This suggests that a broad spectrum of waves accounts for the decadal change in the direct wave impact.

4.3.4 Why is ΔT altered?

The question arises: what determines the direct wave impact, ΔT? By the definition, it is determined by the mean thermal structure and characteristics of waves passing through the TTL. In particular, wave amplitudes and vertical wavelengths relative to the mean thermal structure of the TTL are the most important factors. Waves with larger amplitudes and shorter vertical wavelengths have a higher chance of making CPT colder (see Figure 4.2a-d). In addition to wave characteristics, the sharpness of the mean temperature structure also affects ΔT (see Figure 4.2c-f). If the mean temperature structure of the TTL has a sharp minimum, waves with long vertical wavelengths do not effectively lower CPT. In contrast, if the mean temperature structure is relatively wider than the vertical scale of waves, the chances of lowering CPT are enhanced. We investigate the relation of ΔT with the following three factors for the whole study period in Figure 4.6b: (1) the potential energy from disturbances at CPT tropopause as a proxy of wave activity (red), (2) the width, whose inversed value could be called the sharpness, of the mean temperature structure of the TTL (blue), and (3) the peak vertical wavelength where the spectrum is the strongest (green). All values in Figure 4.6b are de-seasonalized. Note that the black line in Figure 4.6b is anomalies of |ΔT| , so positive values represent stronger wave impacts on CPT. The time series of wave activity and peak vertical wavelength are calculated by spectral analysis37 of each vertical temperature profile (see Methods). The width of the mean thermal TTL is defined in Figure 4.1, and narrower width corresponds to sharper mean temperature structure. In Figure 4.6b, de-seasonalized global lower stratospheric water vapor (light blue) is reproduced from Randel and Jensen (Randel and Jensen, 2013). To compare with wave activity, the sign of the y-axis of water vapor is switched so that drier (negative) values lie above wetter (positive) values.

Wave activity (red) in Figure 4.6b shows a 2-year period signal, having stronger amplitudes

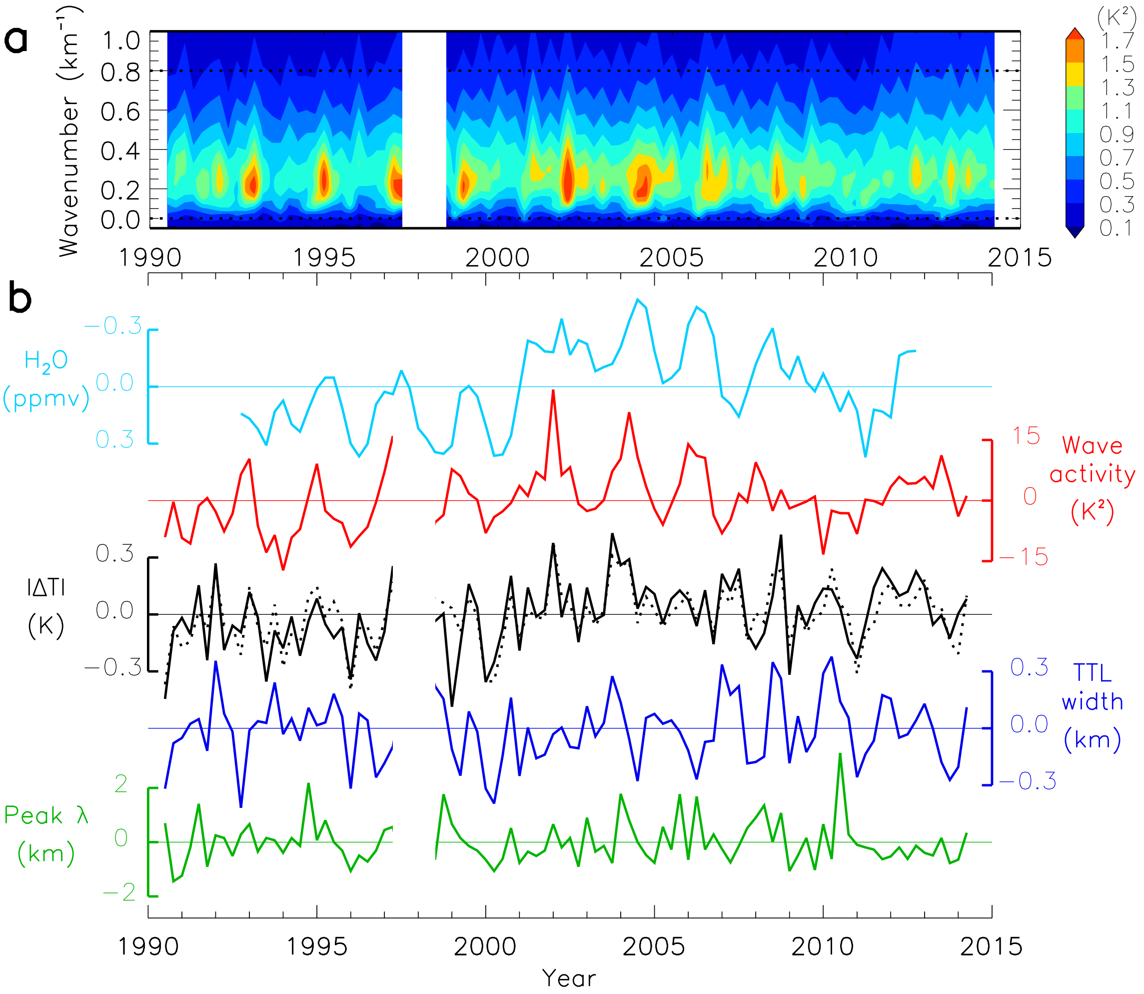

Figure 4.6: (a) Evolution of the power spectrum at the CPT tropopause for each 90-day segment as a function of vertical wavenumber, obtained from S-transform (wavelet-type spectral analysis) for vertical profiles of temperature perturbations. (b) Time series of peak vertical wavelength (green), TTL width (blue), $|\Delta T|$ (black line), wave activity (red), and lower stratospheric water vapor (light blue). The peak wavelength represents the wavelength where the power spectrum in (a) has its peak. The TTL width is defined in Figure 4.1. Wave activity is defined as the integrated power spectrum (potential energy) shown in a over wavenumbers of 0.05-0.8 km^{-1}. The dotted black line depicts reconstructed $|\Delta T|$ from a multivariate linear regression with the two variables of wave activity and TTL width. Lower stratospheric water vapor (light blue) is reproduced from Randel and Jensen (Randel and Jensen, 2013), and the sign of the y-axis is switched. Water vapor data are near-global three-month averages at 83 hPa from combined HALOE and MLS satellite measurements (Randel and Jensen, 2013). All time series are de-seasonalized.

in the easterly phase of the QBO (Baldwin et al., 2001) in the lower stratosphere, while |ΔT| do not have the clear QBO signal. Interestingly, subannual to interannual variations in wave activity are superposed on a slower, decadal time scale oscillation. Low wave activity (red) for the 1990's have increased after 2000 followed by a gradual decrease until about 2010. This slow time scale evolution resembles the one observed in |ΔT| . Meanwhile, the width of the TTL (blue) does not have the decadal scale oscillation. Although its correlation coefficient of 0.55 indicates that the TTL width and |ΔT| are correlated, the width has remained almost the same over the last 2.5 decades if subannual to interannual variations are smoothed. Lastly, the peak vertical wavelength of TTL waves also does not have the decadal scale oscillation and its correlation with |ΔT| is only 0.17. We concluded changes in |ΔT| over our study period are mainly controlled by wave activity and the TTL mean temperature structure. To confirm this, we performed a multivariate linear regression of |ΔT| with the two variables. The dotted black line is the reconstructed time series of |ΔT| using the two linear regression coefficients. The reconstructed value agrees well with observed |ΔT|, suggesting the combination of wave activity (on a decadal scale) and the mean TTL thermal structure (on shorter time scales) mostly determines the direct wave impact.

4.4 Discussion

The decadal scale oscillation of TTL wave activity has further implications on the wave-induced forcing for the Brewer-Dobson circulation. TTL temperatures are more affected by the shallow branch of the circulation than the deep branch (Birner and Bnisch, 2011; Ueyama et al., 2013). The shallow branch upwelling across the TTL is forced by equatorial planetary waves in the TTL and waves in the subtropical upper troposphere and lower stratosphere originating in the tropics and midlatitudes (Randel et al., 2008; Garney et al., 2011; Gerber, 2012; Boehm and Lee, 2003; Ryu and Lee, 2010; Ortland and Alexander, 2014). Although the net TTL upwelling is determined by details of wave dissipation, stronger wave activity might yield stronger dissipation rate inducing stronger upwelling. Indeed, TTL wave activity (red) and lower stratospheric water vapor (light blue) in Figure 4.6b are surprisingly similar at annual (not shown) to interannual and decadal time scales, supporting this idea. Therefore, as pointed out in the beginning, waves play crucial roles in regulating stratospheric water vapor in two ways: by inducing the mean upwelling (indirect) and by perturbing the mean temperature structure (direct). While decadal scale changes in stratospheric water vapor can be traced back to changes in wave activity, it is not clear why there have been the decadal changes in wave activity. Wave sources may have changed with time, or wave propagation may have changed. The generation and maintenance of tropical waves are strongly coupled with the zonal distribution of convection, which is affected by surface temperature (Fu, 2013; Garfinkel et al., 2013). The static stability and mean wind profiles can change wave propagation. These source and propagation issues are highly coupled and inseparable, so understanding the causes of the wave activity change will require further study in the future.

4.5 Supplementary

4.5.1 Vertical spectral analysis

A wavelet-type analysis, specifically S-transform (Stockwell et al., 1996), has been performed to look into wave characteristics in the TTL. The vertical structure of waves can be obtained by S-transform analysis for each vertical profile of temperature perturbation. To calculate a temperature perturbation profile, the mean temperature profile of a corresponding 90-day time segment was subtracted from each temperature profile. Thus our results include disturbances at time scales shorter than 90 days. Vertical levels above 35 km to 100 km are zero-padded to minimize wrap-around effects at the top and bottom of the profiles. A power spectrum as a function of height and vertical wavenumber is calculated for each season. Figure 4.6a shows the time series of the power spectrum at the mean CPT tropopause for each 90-day segment as a function of vertical wavenumber. Then we calculate the time series of de-seasonalized anomalies of the integrated power spectrum over wavenumbers of 0.05-0.8 km^{-1}, shown with a red line in Figure 4.6b. The minimum wavenumber for the integration is set 0.05 km^{-1} to exclude artificial effects due to the zero-padding. Also we set the maximum wavenumber of 0.8 km^{-1} to avoid effects of different vertical resolutions over the years.

4.5.2 S-transform spectrum

Figure 4.7a displays the averaged power spectrum over 1990-2014. The vertical axis is adjusted relative to the mean CPT tropopause for each 90-day segment. The power spectrum shows that temperature variability is the strongest near the TTL and lower stratosphere. In Figure 4.7b, The cross section of the power spectrum at the CPT tropopause shows that the spectrum peaks at the vertical wavenumber of 0.24 km^{-1}, equivalent to the vertical wavelength of 4.16 km. This indicates waves with vertical wavelengths near 4.16 km have the greatest impact on TTL temperature variability. We note that the peak wavelength depends on which wave periods are included in the calculation. Our estimation includes all waves shorter than 90 days.

4.5.3 Uncertainties due to changes in vertical resolution of radiosonde data

ΔT, by definition, would be sensitive to how much of the wave spectrum are captured in radiosonde observations. This means ΔT could be affected by vertical resolution, that is, the number of raw measurements as a balloon ascends. To look into the effect of vertical resolution, we have counted the number of measurements within a 2 km range of the TTL from each balloon. Since vertical resolution near the CPT tropopause is important for ΔT, and CPT tropopause is not a fixed quantity, we first calculate the CPT tropopause for each 90-day time segment. Then we count the number of measurements for each balloon within the range of 1 km above and 1 km below the CPT tropopause. As shown in Figure 4.8, vertical resolutions of measurements over 1990-1998 were slightly coarser than years after 1999. In our all analyses, data for early 1990 and around 1998 were not included because of too-coarse vertical resolution and fewer recorded profiles than other years. The number of 6 on the y-axis in Figure 4.8 corresponds to vertical resolution of 333 m.

To estimate a possible bias in ΔT due to different vertical resolution, raw data within the 2 km TTL range from each balloon measurements were intentionally removed. By removing measurement points, we calculate ΔT as a function of an average number of vertical measurements for each 90-

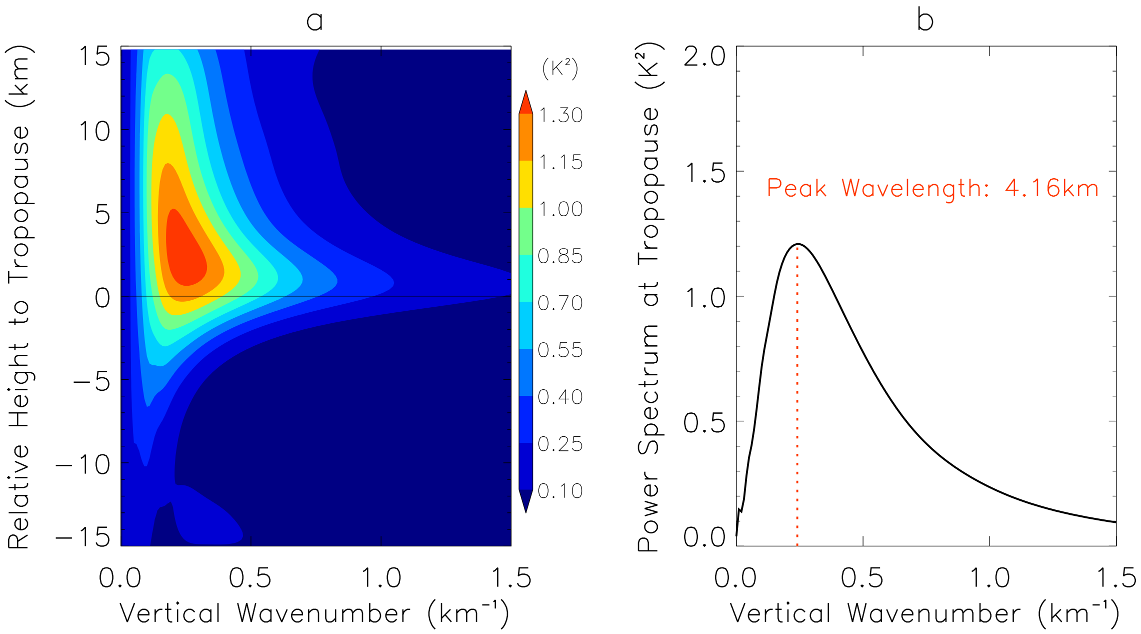

Figure 4.7: (a) Average power spectrum from S-transform analysis of temperature profiles over 1990-2014 as a function of vertical wavenumber and relative height to the CPT tropopause. The CPT tropopause is calculated for each 3-month period. (b) Cross section of the power spectrum in a at the CPT tropopause.

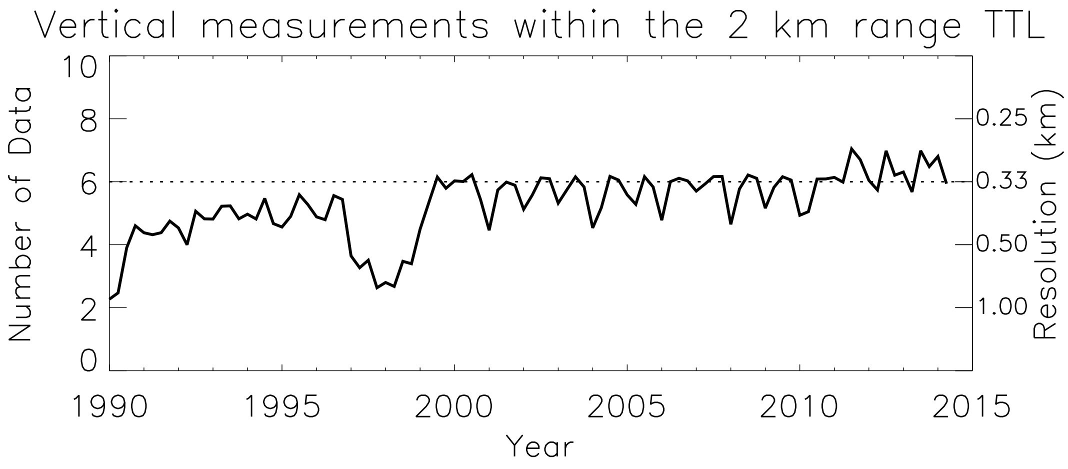

Figure 4.8: Average vertical resolution of raw radiosonde data in the TTL. To calculate vertical resolution, the averaged number of measurements per balloon launch is counted between 1 km above and below the CPT tropopause for each 3-month period.

day period. The calculations over 1999-2014 show that one fewer vertical measurement points in the TTL tends to yield a smaller |ΔT| value by 0.054 K. The bias shown in Figure 4.5 is based on this value and observed number of vertical measurements. The uncertainty value is a relative bias to the measurement number of 6 corresponding to the vertical resolution of 333 m. We also looked at the correlation between the number of measurements near the TTL and the CPT on a profile-to-profile basis. In this approach, we collected all $T_{min} - \overline{T_{min}}$ and the number of vertical measurements within the 2 km range of the TTL over 1999-2010 when the average vertical resolution remained almost the same. This approach yielded a correlation of 0.056 K/measurement between |ΔT| and the number of vertical measurement points, almost the same result of the first approach.

4.5.4 Do changes in the number of observed profiles affect ΔT?

In addition to uncertainties related to vertical resolution changes, we have also considered changes in the number of recorded temperature profiles over the years. Since the radiosonde measurements are taken twice a day, the total number of profiles should be 180 for a 90-day period if all measurements are perfect. We have found that the numbers of profiles for early years are slightly lower than recent years. To examine a possible bias due to this issue, we randomly discarded some profiles if measured profiles exceed 126 profiles (70% of 180) for each 90-day segment. The resulting ΔT remains almost the same even though we only take 126 temperature profiles for our calculation, so we can conclude changes in the number of measured profiles over the years do not give any significant bias on the estimation of ΔT.

Chapter 5

Aircraft observations of waves and tracers in the tropical tropopause layer

5.1 Introduction

The Airborne Tropical TRopopause EXperiment (ATTREX) mission is a field campaign aiming to understand physical, chemical, and radiative processes in the TTL (Jensen et al., 2013). A NASA Global Hawk (Figure 5.1), an unmanned high-altitude aircraft, flew in the TTL over the central to eastern Pacific from the NASA Armstrong Flight Research Center, California, for October-November 2011 and February-March 2013, and over the western Pacific from Guam for February-March 2014. The aircraft was installed with various instruments measuring meteorological fields, radiative fluxes, cloud properties, water vapor, numerous chemical species, and tracers such as CO, CO_2, CH_4, N_2O, SF_6 and O_3.

5.2 Flight details

Among many ATTREX flights, this study focuses on the flight on February 16-17, 2014. During this flight communication with the satellite Inmarsat was inoperative, so the aircraft was not allowed to go anywhere except a small area near Guam. The aircraft repeatedly climbed and dove within a horizontal area of $1^\circ \times 1^\circ$ centered at 145.9°E, 13.1°N close to Guam (144.8°E, 13.5°N) for about 18 hours. Figure 5.2a shows the horizontal flight path depicted by the red line, and the blue square represents the Guam radiosonde site. Figure 5.2b shows the aircraft vertical path. As a result, the flight observations provide continuous radio/dropsonde-like profiles at a nearly fixed location. As there are about 24 vertical profiles during 18 hour measurements, an average

Figure 5.1: NASA Global Hawk used in the ATTREX mission. From www.nasa.gov.

time resolution is about 0.5-1 hours. Note that typically 3-hourly radiosonde observations from a field campaign are considered as high time resolution measurements, so our measurements are unprecedented high time resolution data.

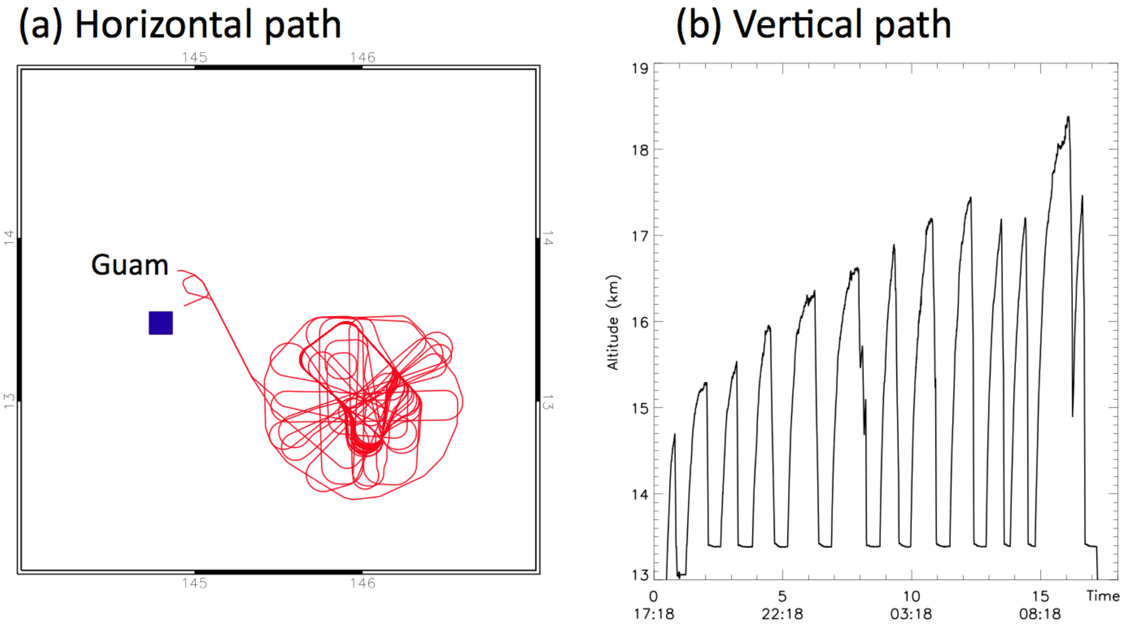

Figure 5.2: (a) The horizonal and (b) vertical path of the Global Hawk aircraft for the flight on February 16-17, 2014 during the ATTREX deployment in Guam. The blue square in (a) represents the Guam radiosonde location.

5.3 Large-scale meteorological conditions

Figure 5.3 shows the mean temperature and winds at 100 hPa for December 2013-February 2014 from MERRA reanalysis. The mean conditions show a typical pattern of temperature and winds in boreal winter time. This pattern is due to the Gill-type wave response to tropical convection (Matsuno, 1966; Gill, 1980). Guam is near the center of the northern Rossby wave gyre, showing no strong winds near the area. However, temperature in the TTL above Guam is near the edge of the coldest region in the western Pacific, so we expect that there are ubiquitous cirrus clouds. Figure 5.4a-f show time evolution of temperature and wind anomalies for 10 days. Day 0 denotes the measurement day, February 17, 2014 at 0Z. The anomaly plots in Figures 5.4a-b indicate that a strong cyclonic Rossby wave circulation was propagating eastward near the Guam area before the flight day. On the measurement day (Day 0) in Figure5.4d, there were no strong large-scale disturbances in Guam. Then, right after the measurement day, a Rossby wave anti-cyclonic motion developed and propagated eastward near Guam, as shown in Figure 5.4e-f. Thus the flight day was right in the middle between strong, large-scale cyclonic and anti-cyclonic motions. This is consistent with radiosonde observations as shown in Figure 5.5. The aircraft vertical path is depicted by a thin purple line around February 17. Although the MERRA meteorological fields indicate a weak large-scale motion on the measurement time and location, the radiosonde profiles in Figure 5.5 suggest that an interesting vertical structure exists near the flight area and time.

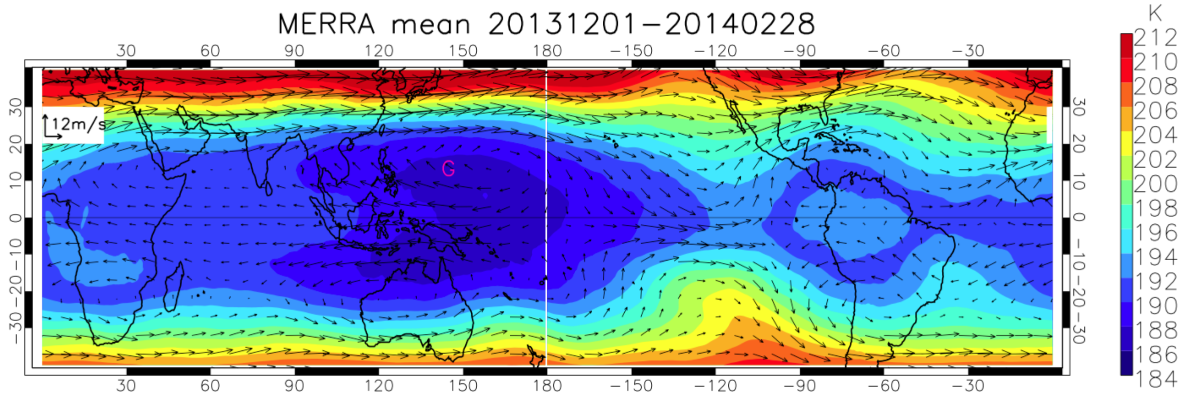

Figure 5.3: The mean temperature (colors) and horizontal winds (arrows) for December 2013-February 2014 in MERRA. The pink G letter indicates Guam.

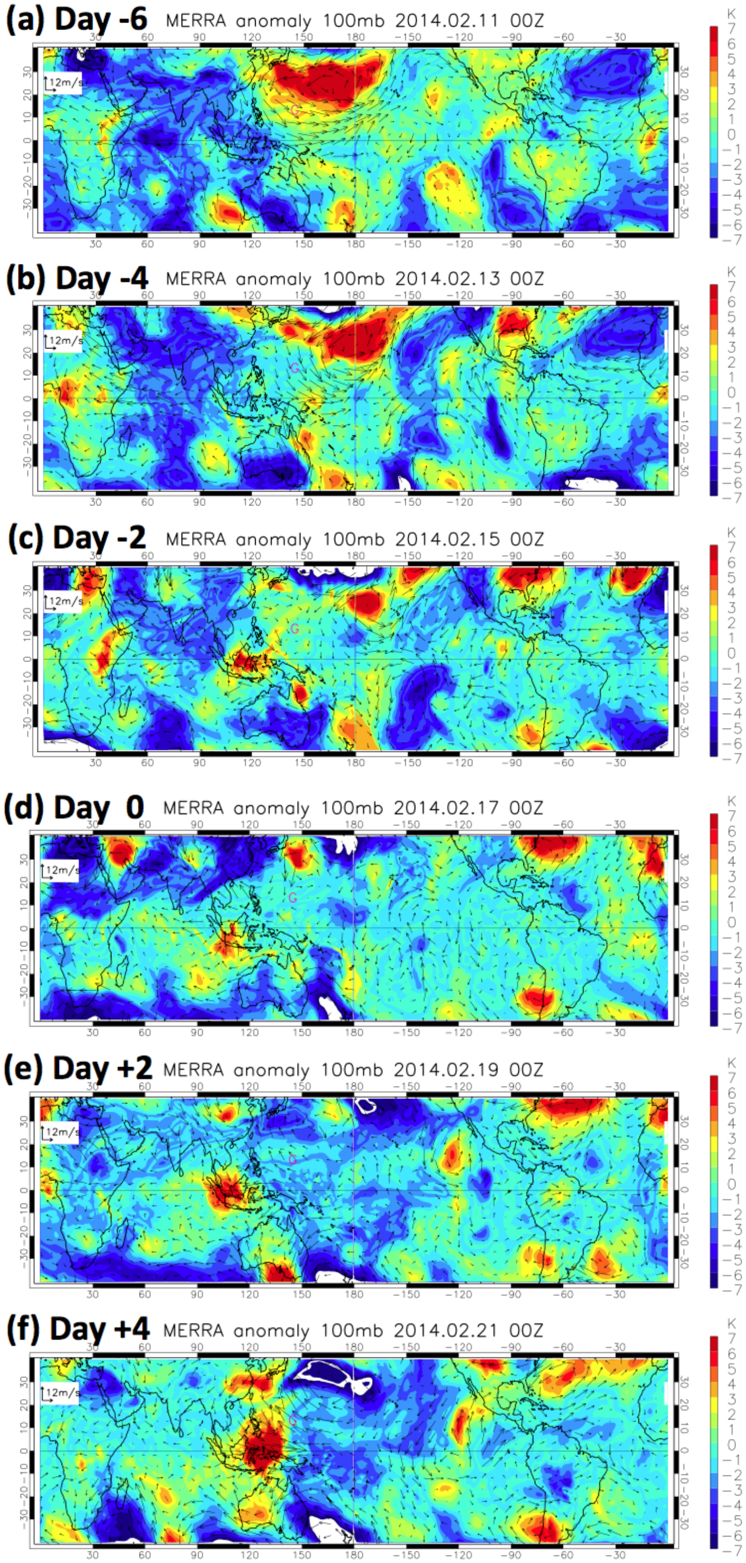

Figure 5.4: The evolution of temperature and wind anomalies from February 11-21, 2014. The anomaly is defined by perturbation against the time mean value at each horizontal grid point.

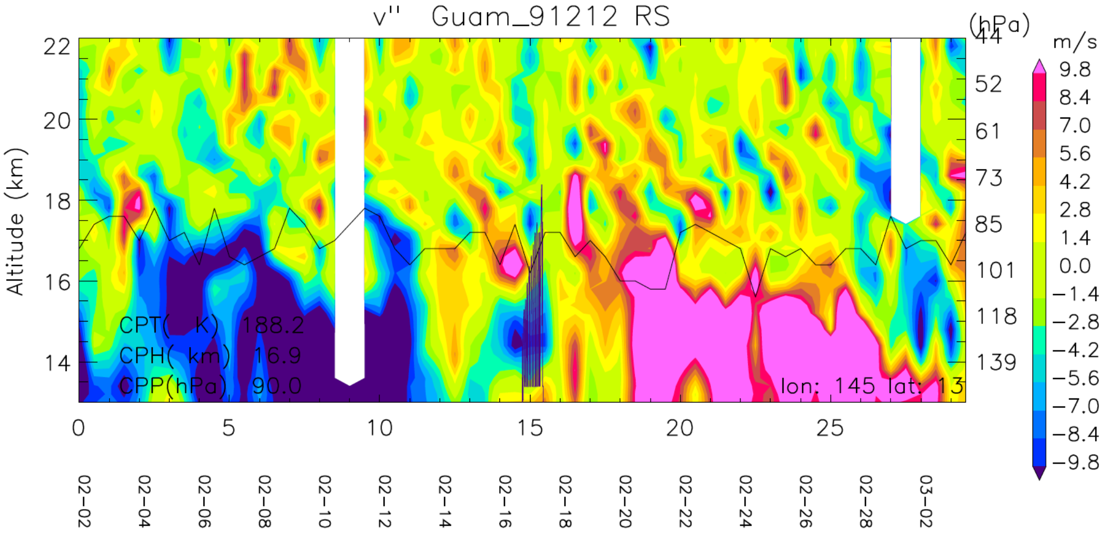

Figure 5.5: Guam radiosonde profiles of 30-day meridional wind anomalies centered on the flight time. The thin purple line between 02-16 and 02-18 is the flight path, and the black line represents the cold-point tropopause.

5.4 ATTREX aircraft measurements

5.4.1 Meteorology

Figure 5.6 show the time evolution of vertical profiles of temperature, zonal wind, and meridional wind observed by the aircraft in the TTL for about 18 hours. All three fields show a fine vertical structure with small changes over time. Figure 5.7 shows relationships of zonal and meridional winds from each vertical profiles. The two wind components oscillate with an elongated elliptical shape for the aircraft elapsed time between ∼4.4-14.7 hours. Estimation of a vertical wavelength and a vertical phase propagation speed from the measurements in Figure 5.6 yields an approximate period of 44 hours. The inertial period at the latitude of 13.1°N is 53 hours. Based on the period of the waves and oscillation characteristics between zonal and meridional winds in Figure 5.7, we can conclude the observed waves are inertial gravity waves.

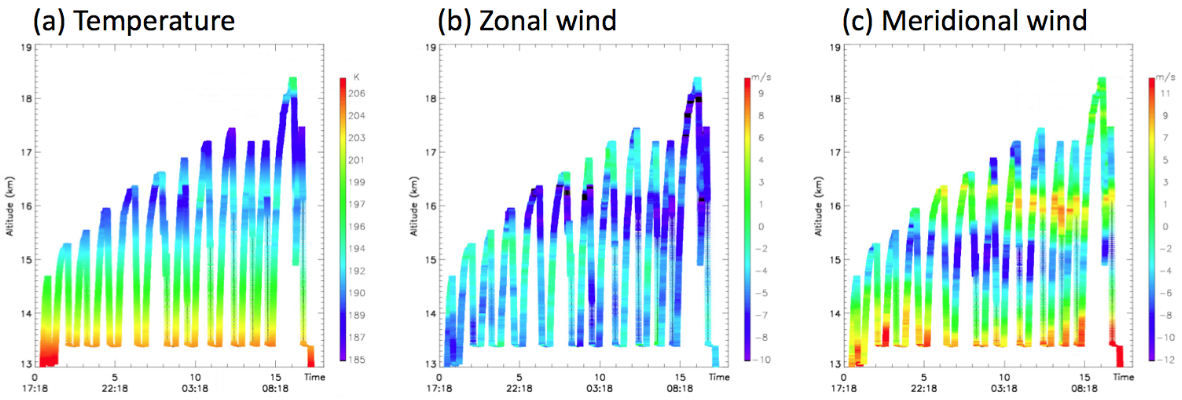

Figure 5.6: Aircraft measurements of (a) temperature, (b) zonal wind, and (c)meridional wind.

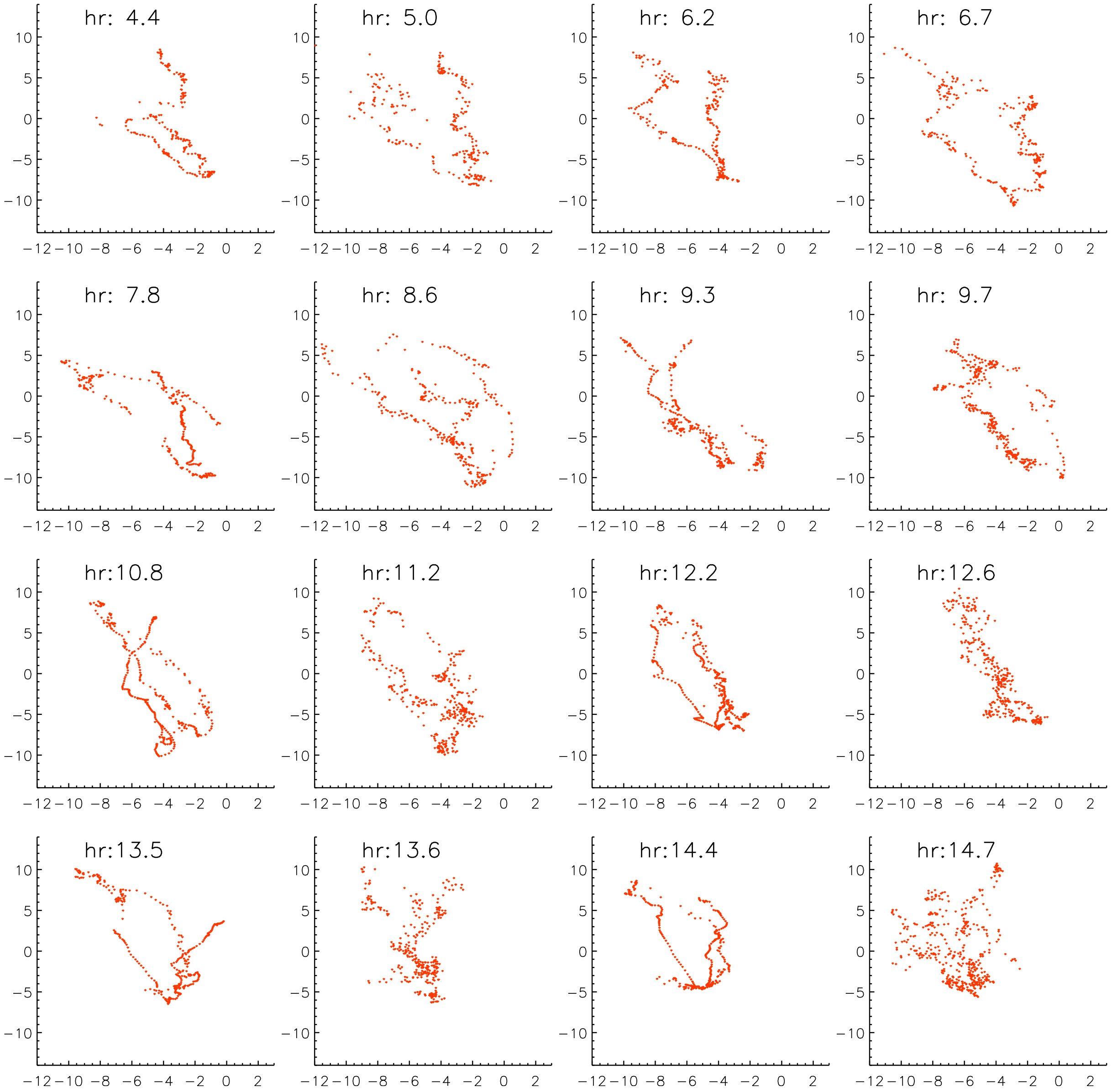

Figure 5.7: Relationships between zonal and meridional winds from each vertical profiles. The starting measurement time for each profile is shown on the top of panels. The x-axis is for zonal and y-axis is for meridional wind, and both units are m s^{-1}.

The fine vertical structure is more clearly shown in Figure 5.8. Vertical temperature profiles in Figure 5.8 have a double tropopause structure, and wind profiles in Figures 5.8b-c show an opposite phase of zonal and meridional wind. The vertical wavelength of the wave structure is about 1.7 km. This fine vertical structure cannot be resolved in models, since current analysis/reanalysis model can only resolve waves at scales longer than 2.4 km at most due to limited vertical resolution near the TTL. We confirm that the observed double tropopause and wind oscillations are completely missing in GFS analysis in Figure 5.9. ERA and MERRA also do not have the observed structure (not shown).

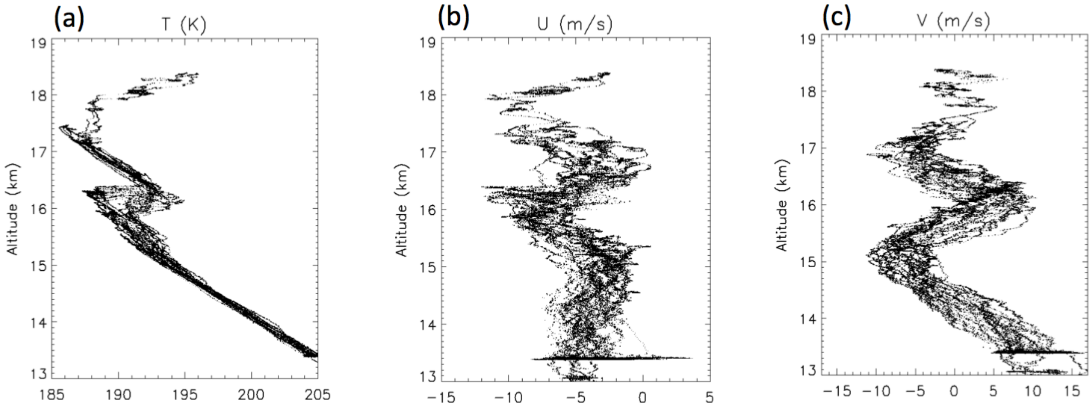

Figure 5.8: Vertical profiles from all measurement points during the flight.

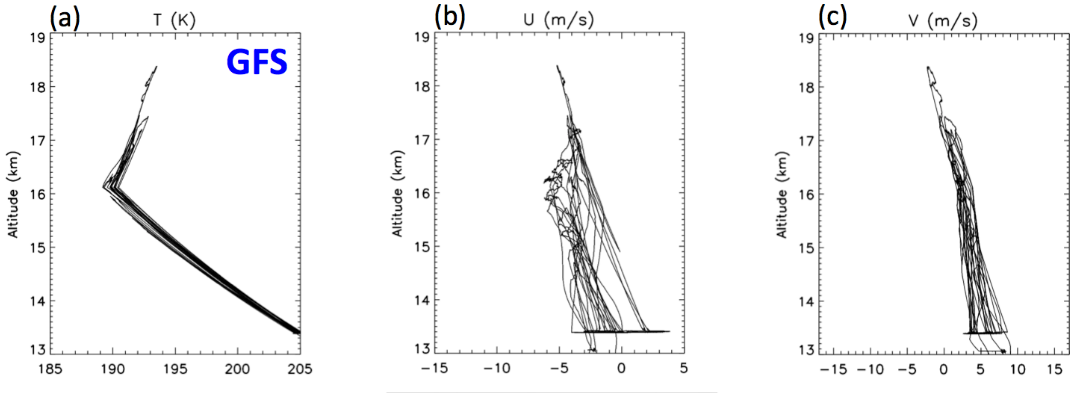

Figure 5.9: Vertical profiles sampled from GFS analysis data at the flight location and time.

5.4.2 Tracers

The advantage of the aircraft measurements over a typical, operational radiosonde is measurements of various atmospheric constituents. Among various tracer gases, we plot CH_4, CO_2, CO, and O_3 in Figure 5.10 to look into the evolution of tracers. These tracers surprisingly follow the evolution of the meteorological fields, especially meridional wind. CH_4 shows enhanced concentration within a thin layer of less than 1 km at about 15 km, and the shape of this higher CH_4 resembles the negative meridional wind field. The same time evolution of this structure near 15 km is also observed in CO_2 and CO concentration. The high O_3 concentration also shows a downward propagation between 16 km to 15 km, following the same characteristics of the meridional wind propagation over the measurement period.

Water vapor observations in Figure 5.11 shows the similar time evolution to meridional wind. The cloud imagery from CPL in Figure 5.12 indicates there were layers of cirrus clouds over Guam. The highest cloud occurred near 15 km, and we assume this is the highest dehydration level. Therefore we can expect positive wind below 15 km will transport moist air from the tropics to the subtropics, while positive wind above 15 km will transport dry air from the tropics to the subtropics. This is consistent with the time evolution of higher water vapor below 14 km and the lower value above 16 km in Figure 5.11.

5.5 Short vertical scale waves in radiosonde and MERRA data

We further investigate how often these waves with short vertical wavelengths exist in the TTL using radiosonde data. Figure 5.13 shows an example of 10 vertical profiles of meridonal wind anomailies on December 2-6, 2013 at Guam radiosonde and MERRA. The MERRA profiles are sampled at the Guam radiosonde location. While many fine vertical structures above the upper troposphere are shown in the radiosonde profiles, MERRA shows limitation of vertical resolution in the upper layer. For more quantitative estimation we performed a wavelet-type analysis (S-

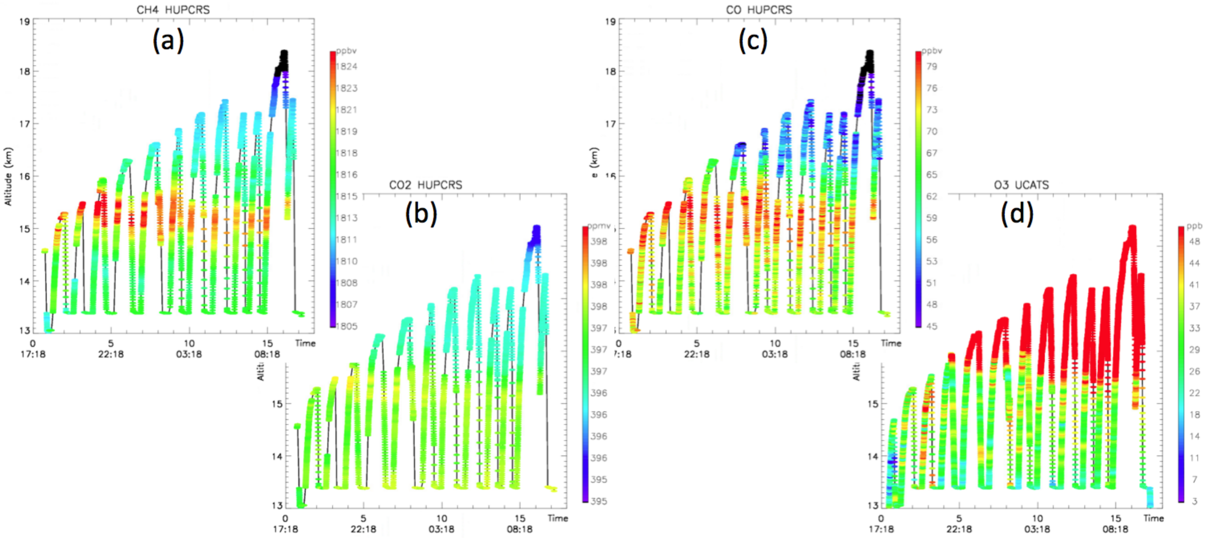

Figure 5.10: Aircraft measurements of (a) CH_4, (b) CO_2, (c) CO, and (d) O_3.

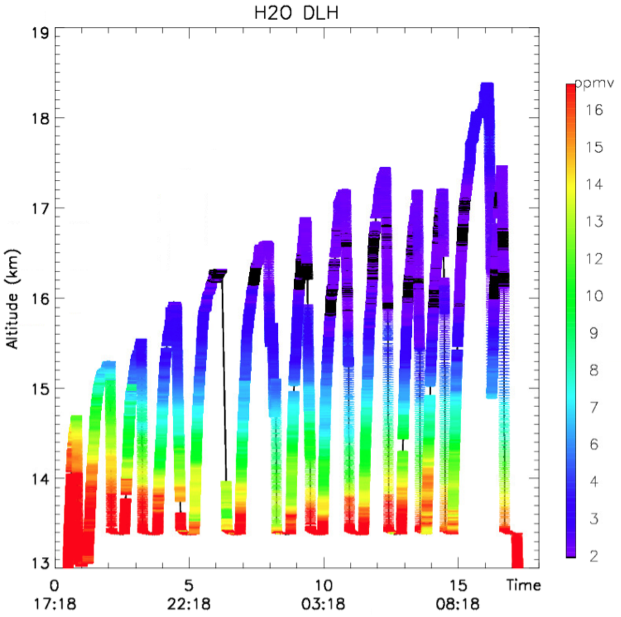

Figure 5.11: Aircraft measurements of water vapor.

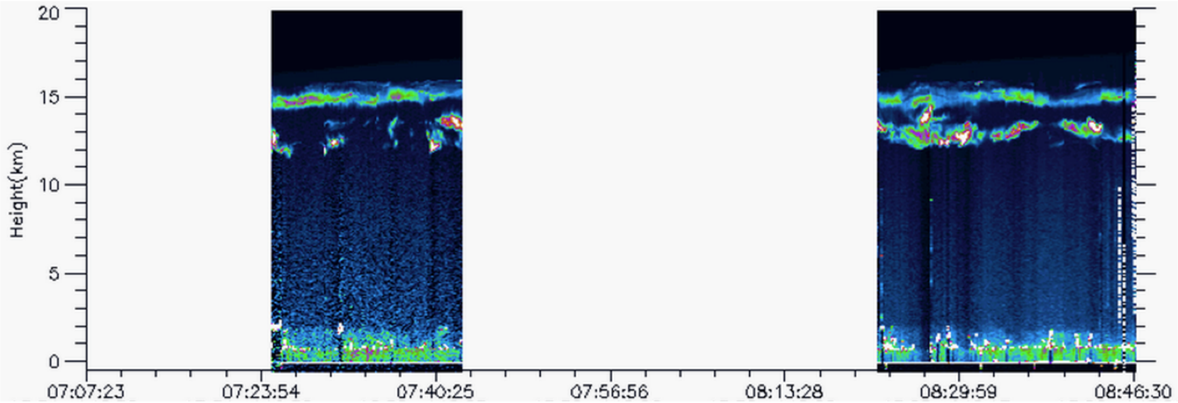

Figure 5.12: Backscattering at 532 nm from the Cloud Physics Lidar (CPL) for a segment of the flight

transform) for all radiosonde vertical profiles of meridional wind anomalies in Guam for December 2013-February 2014. Figures 5.14a-b are the S-transformed power spectra as a function of vertical wavenumber and height for radiosonde and MERRA data. Figure 5.14c shows an integrated value for the TTL from 15 km to 19 km (Note that here we use log-pressure altitude calculated from pressure). The S-transform result shows strong variability in the TTL with the peak vertical wavenumber of 0.2 km^{-1} equivalent to the vertical wavelength of 4.8 km. Also the spectrum at higher vertical wavenumbers is still significant in radiosonde observations. The MERRA spectrum reveals striking deficiency at higher vertical wavenumbers as expected due to its vertical resolution of about 1.2 km in the TTL. Figure 5.14 also reveals that the MERRA spectrum even at vertical wavelengths of 2.4-6 km are significantly less than the radiosonde spectrum.

5.6 Discussion

The aircraft measurements of temperature, winds, and tracers prove that the tracer transport is clearly affected by the fine, vertical wave motion. Also, radiosonde observations show that a significant portion of TTL disturbances is attributed to these waves whose scales cannot be resolved in current analysis/reanalysis and climate models due to coarse vertical resolution of models. A wavelet S-transform analysis of radiosonde data also reveals that waves even at scales longer than 2.4 km are still significantly underestimated in MERRA. These results suggest that models will misrepresent consequences induced by these waves in the TTL. For example, trajectory simulations heavily rely on meteorological fields from analysis or reanalysis data. Stratospheric water vapor and TTL cloud formation are mainly determined by temperature. Parcel paths are determined by horizontal winds. So uncertainties in temperature would lead to uncertainties in simulations of dehydration in the TTL, and uncertainties in wind variability would result in uncertainties in trajectory calculations of the origin of air transported into the stratosphere. From the ATTREX observations, we have identified waves with the amplitude of ~2-3 K in temperature, ~5 m s^{-1} in zonal and ~10 m s^{-1} in meridional wind. This temperature perturbation is big enough to affect in-situ cirrus cloud formation depending on wave frequency and ambient conditions of temperature

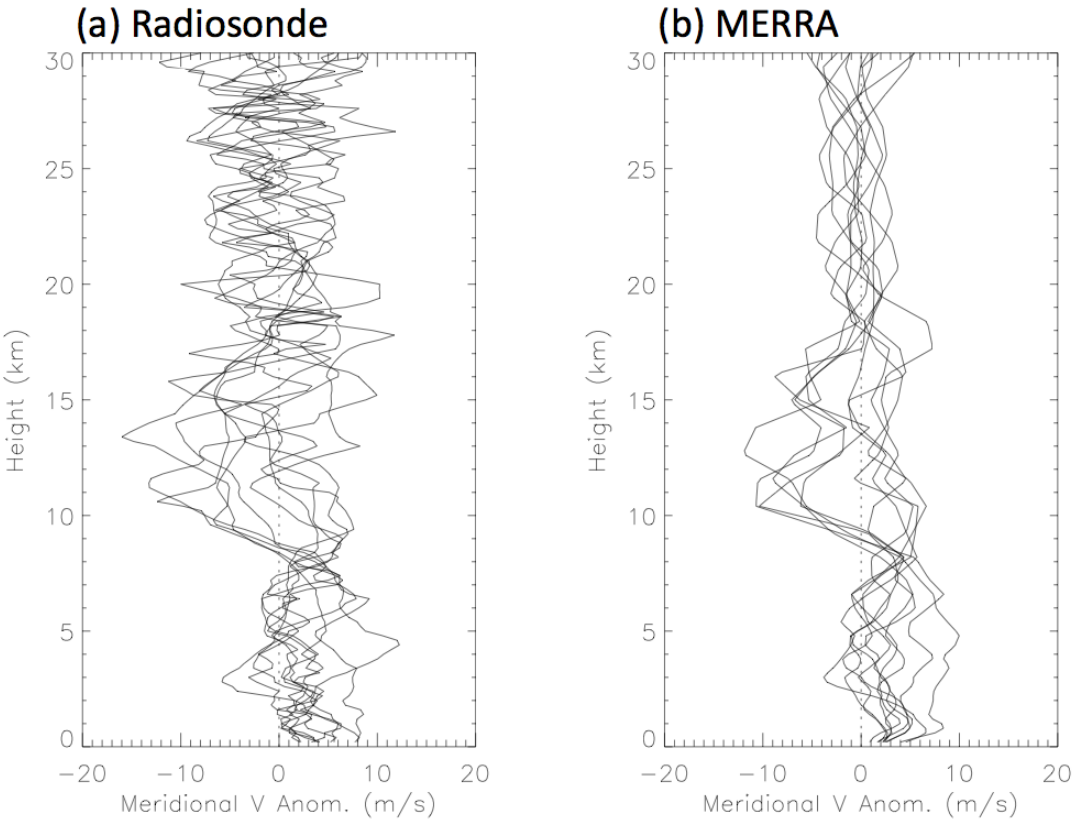

Figure 5.13: Vertical profiles of meridional wind anomalies in (a) radiosonde and (b) MERRA data in Guam for December 2-6, 2013.

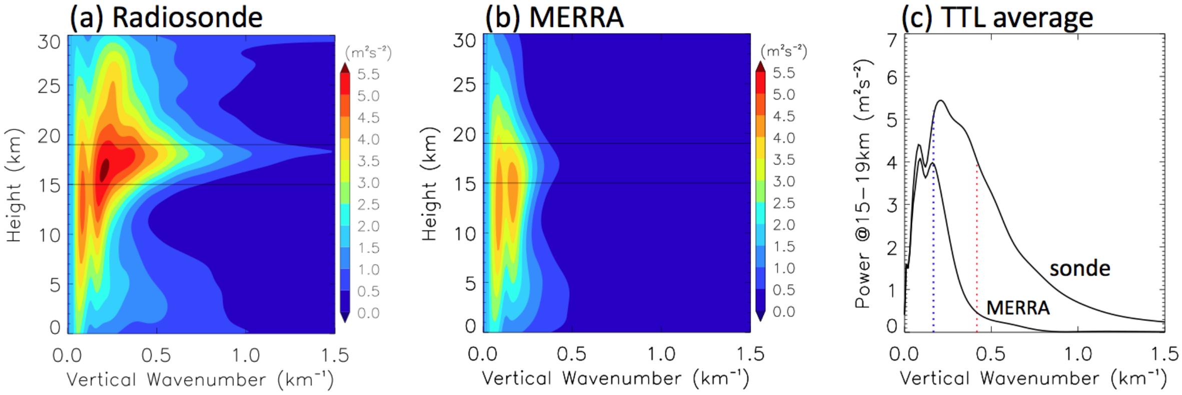

Figure 5.14: S-transform spectrum of meridional wind anomalies for December 2013-February 2014 from (a) radiosonde (b) MERRA data in Guam. (c) Spectrum averaged over 15-19 km. The blue and red dotted line represents the wavelength of 6 km and 2.4 km, respectively.

and humidity. Considering the order of the mean zonal (∼10 m s^{-1}) and meridional (∼0-1 m s^{-1}) wind in the TTL, we can expect perturbations to meridional wind will have significant impacts on latitudinal transport of air. More comprehensive studies will be required to understand the fine vertical scale of waves in the TTL and their impacts on transport and cloud formation, as their general horizontal and frequency characteristics are not well known.

Chapter 6

Conclusions

This thesis studies roles of tropical waves in weather and climate focusing on tropical convection and physical processes in the tropical tropopause layer (TTL). To provide insights into improving models and a better understanding of equatorial waves, we have studied the following: (1) Convectively coupled equatorial waves (CCEWs) in tropical precipitation from observations and reanalysis data, (2) Representation of TTL waves in reanalysis data and a new wave scheme developed for trajectory simulations of stratospheric water vapor, (3) Direct wave impacts on cold-point tropopause temperature, and (4) Aircraft measurements of waves and tracers in the TTL.

6.1 Summary

First, tropical precipitation characteristics as a result of CCEWs and as a source of vertically propagating waves are studied using the TRMM satellite estimates and five reanalyses including NCEP-NCAR, NCEP-DOE, MERRA, ERA-interim, and NCEP-CFSR for the period of 2005-2007. Spectral analysis shows unique space-time variability in tropical precipitation coupled with Kelvin, equatorial Rossby, mixed-Rossby gravity, inertial gravity, and tropical depression-type waves. All reanalysis models produce more rainfall relative to TRMM but their variability is much weaker at higher frequencies. This lack of high frequency precipitation suggests that waves would not be well represented in the TTL and stratosphere since tropical convection is a main source of waves propagating into the upper atmosphere.

Second, waves in the TTL were examined using temperatures at 24 tropical radiosonde locations and compared with results in two reanalyses, ERA-interim and MERRA. Temperature variability in reanalyses is weaker at higher frequencies with periods shorter than 10 days, while lower frequency waves are relatively well represented. Based on the results, we have developed a new wave parameterization scheme for trajectory simulations of stratospheric water vapor and TTL cirrus clouds. The new scheme interpolates wave amplitudes and phases in Fourier space instead of in real space to avoid artificial degradation of wave amplitudes in-between reanalysis vertical model levels. Then amplitudes of waves are amplified to match radiosonde results. Temperatures from COSMIC GPS measurements confirm the new approach generates realistic temperature variability throughout the tropics. We have found that, even though the mean temperature is the same, having stronger waves lowers the cold-point tropopause temperature.

Next, our finding of the relation between wave activity and cold-point tropopause temperatures has led to an extended, comprehensive study of this relation using historical radiosonde data. Temperatures from 23-year observations of radiosondes in the western Pacific show that a broad spectrum of waves lowers mean cold-point temperatures by 1.6 K on average. Moreover this direct wave impact has seasonal, interannual, and decadal scale variations, suggesting changes in wave activity in the TTL have important implications for the transport of upper tropospheric water vapor into the lower stratosphere.

Lastly, aircraft measurements in the TTL from the ATTREX mission were analyzed. The flight on February 16-17, 2014 has provided unprecedented measurements of waves and tracers in the TTL. Continuous vertical profiling in the TTL for about 18 hours in the confined horizontal area within $1^\circ \times 1^\circ$ near Guam serves as very high vertical and time resolution radiosonde-like data. Our analysis shows that the time evolution of a fine vertical wave structure with the vertical scale of $\sim$1.7 km has a strong correlation with the changes in the tracer distribution. Radiosonde observations of meridional wind in Guam suggest that these fine vertical scale disturbances in the TTL are ubiquitous, but they are completely missed by analysis/reanalysis models.

6.2 Perspectives

Atmospheric equatorial waves have a broad impact on tropical weather and global climate by coupling with tropical convection, by modulating temperature in the TTL, and by interacting with winds in the stratosphere. Global weather forecast models have been greatly improved over the past decades due to improvements in model physics, global observations of assimilation fields, and increasing computer power enabling high model resolution simulations. Based on observations of tropical convection and temperature variability in the TTL, this thesis confirms that the latest global reanalysis models for MERRA and ERA-interim well represent equatorial waves at time scales longer than about a few to ten days. However, shorter time scale waves are still missed or underrepresented in models.

Although we have provided a wave parameterization method to reduce uncertainties associated with waves in trajectory simulations of the dehydration process in the TTL, our method works only for waves that are resolved in models to a certain degree. Waves that are completely missed in reanalysis models cannot be recovered by our wave parameterization scheme. Results from aircraft and radiosonde measurements showed that vertically unresolved waves have significant contribution to the total variance in the TTL. These fine vertical scale waves have impacts on the dehydration and transport of air in the TTL. This thesis also emphasized the importance of waves in the TTL by showing that changes in wave activity affects changes in cold-point tropopause temperature, that would result in changes in stratospheric water vapor at a decadal time scale.

Current analysis/reanalysis and climate models have limited ability to capture equatorial waves. One of the critical origins of the problem is related to proper representation of tropical convection as a main source of wave generation. Even accurate sources of equatorial waves will not ensure accurate wave propagation and wave-induced impacts in the upper atmosphere in current models. One of the fundamental problems of prohibiting representations of waves in the TTL and stratosphere can be inferred from our findings in this thesis; limited vertical resolution of models in the TTL and lower stratosphere does not allow proper propagation of waves.

Waves can propagate horizontally and vertically with time variations. This means waves have a four dimensional structure: two in the horizontal, one in the vertical, and one in the time. Power spectra at horizontal and temporal scales are *red*, meaning that their spectral curves always decrease with wavenumber/frequency. This is a universal property for any meteorological parameter in any region. Since the horizontal and temporal spectra follow the universal power law, a spectrum beyond the scale of the model limitation of resolution would not be significant compared to the total spectrum. The power spectrum in the vertical space, however, has a different shape; its spectrum does not peak at the lowest wavenumber. The peak vertical wavenumber differs at different altitudes. In general, the peak is at a wavelength of near 4 km in and above the TTL, while longer in the troposphere. As shown in this thesis, observations of meteorological fields indicate that significant variability is from the scales that current models cannot resolve due to limited vertical resolution. This implies that waves at shorter vertical scales in models cannot propagate into the upper atmosphere. This problem would cause a series of problems. Wave-induced temperature perturbations in the TTL cannot be resolved, affecting the radiation budget through cirrus clouds and stratospheric water vapor. Wave-induced circulations cannot be properly represented in models, affecting the distribution of ozone and other important chemical constituents. Wave energy at the fine vertical scales are prohibited from propagating upward. Misrepresenting waves in the upper atmosphere also has impacts on the troposphere. Weather and climate simulations have shown that gravity wave parameterization and the inclusion of the stratosphere in simulations increased model accuracy in the troposphere. Therefore, accompanied with efforts in improving model physics such as convective parameterization, increasing vertical resolution near the TTL should be a future direction towards improvements in tropical weather and global climate.

Bibliography

Alexander, M. J. and J. R. Holton, 1997: A model study of zonal forcing in the equatorial stratosphere by convectively induced gravity waves. *J. Atmos. Sci.*, **54**, 408–419.

Alexander, M. J. and J. R. Holton, 2004: On the spectrum of vertically propagating gravity waves generated by a transient heat source. *Atmos. Chem. Phys.*, **4**, 923–932.

Aschmann, J., B. M. Sinnhuber, E. L. Atlas, and S. M. Schauffler, 2009: Modeling the transport of very short-lived substances into the tropical upper troposphere and lower stratosphere. *Atmos. Chem. Phys.*, **9**, 9237–9247.

Baldwin, M. P., et al., 2001: The Quasi-Biennial Oscillation. *Rev. Geophys.*, **39**, 179–229.

Bergman, J. W., E. J. Jensen, L. Pfister, and Q. Yang, 2012: Seasonal differences of vertical-transport efficiency in the tropical tropopause layer: On the interplay between tropical deep convection, large-scale vertical ascent, and horizontal circulations. *J. Geophys. Res.*, **117**, D05 302.

Betts, A., M. Zhao, P. Dirmeyer, and A. Beljaars, 2006: Comparison of ERA40 and NCEP/DOE near-surface data sets with other ISLSCP-II data sets. *J. Geophys. Res.*, **111**, D22S04.

Birner, T. and H. Bnisch, 2011: Residual circulation trajectories and transit times into the extratropical lowermost stratosphere. *Atmos. Chem. Phys.*, **11**, 817–827.

Boehm, M. T. and S. Lee, 2003: The implications of tropical rossby waves for tropical tropopause cirrus formation and for the equatorial upwelling of the brewer-dobson circulation. *J. Atmos. Sci.*, **60**, 247–261.

Bosilovich, M., J. Chen, F. Robertson, and R. Adler, 2008: Evaluation of global precipitation in reanalyses. *J. Appl. Meteor. Climatol.*, **47**, 2279–2299.

Brewer, A. W., 1949: Evidence for a world circulation provided by the measurements of helium and water vapor distribution in the stratosphere. *Q. J. R. Meteorol. Soc.*, **75**, 351–363.

Brown, R. and C. Zhang, 1997: Variability of midtropospheric moisture and its effect on cloud-top height distribution during toga coare. *J. Atmos. Sci.*, **54**, 2760–2774.

Cho, H., K. Bowman, and G. North, 2004: Equatorial waves including the Madden–Julian oscillation in TRMM rainfall and OLR data. *J. Climate*, **17**, 4387–4406.

Dee, D., et al., 2011: The ERA-interim reanalysis: configuration and performance of the data assimilation system. *Quart. J. Roy. Meteor. Soc.*, **137**, 553–597.

Dessler, A. E. and H. Kim, 1999: Determination of the amount of water vapor entering the stratosphere based on halogen occultation experiment (haloe) data. *J. Geophys. Res.*, **104**, 30 605–30 607.

Dessler, A. E., M. R. Schoeberl, T. Wang, S. M. Davis, and K. H. Rosenlof, 2013: Stratospheric water vapor feedback. *PNAS*, **110 (45)**, 18 087–18 091.

Dickinson, M. and J. Molinari, 2002: Mixed Rossby-gravity waves and western pacific tropical cyclogenesis. *J. Atmos. Sci.*, **59**, 2183–2196.

Dvortsov, V. L. and S. Solomon, 2001: Response of the stratospheric temperatures and ozone to past and future increases in stratospheric humidity. *J. Geophys. Res.*, **106**, 7505–7514.

Forster, P. and K. Shine, 2002: Assessing the climate impact of trends in stratospheric water vapor. *Geophys. Res. Lett.*, **29**, 1086.

Forster, P. M. d. F. and K. P. Shine, 1999: Stratospheric water vapour changes as a possible contributor to observed stratospheric cooling. *Geophys. Res. Lett.*, **26**, 3309–3312.

Frank, W. and P. Roundy, 2006: The role of tropical waves in tropical cyclogenesis. *Mon. Wea. Rev.*, **134**, 2397–2417.

Frierson, D., D. Kim, I. Kang, M. Lee, and J. Lin, 2011: Structure of AGCM-simulated convectively coupled kelvin waves and sensitivity of convective parameterization. *J. Atmos. Sci.*, **68**, 26–46.

Fu, Q., 2013: Bottom up in the tropics. *Nature Clim. Change*, **3**, 957–958.

Fueglistaler, S., 2012: Stepwise changes in stratospheric water vapor. *J. Geophys. Res.*, **117**, D13 302.

Fueglistaler, S., M. Bonazzola, P. H. Haynes, and T. Peter, 2005: Stratospheric water vapor predicted from the lagrangian temperature history of air entering the stratosphere in the tropics. *J. Geophys. Res.*, **110**, D08 107.

Fueglistaler, S., A. E. Dessler, T. J. Dunkerton, I. Folkins, Q. Fu, and P. W. Mote, 2009: Tropical tropopause layer. *Rev. Geophys.*, **47**, RG1004.

Fueglistaler, S. and P. H. Haynes, 2005: Control of interannual and longer-term variability of stratospheric water vapor. *J. Geophys. Res.*, **110**, D24 108.

Fueglistaler, S., H. Wernli, and T. Peter, 2004: Tropical troposphere-to-stratosphere transport inferred from trajectory calculations. *J. Geophys. Res.*, **109**, D03 108.

Fueglistaler, S., et al., 2013: The relation between atmospheric humidity and temperature trends for stratospheric water. *J. Geophys. Res.*, **118**, 1052–1074.

Garfinkel, C. I., D. W. Waugh, L. D. Oman, and M. M. Hurwitz, 2013: Temperature trends in the tropical upper troposphere and lower stratosphere: Connections with sea surface temperatures and implications for water vapor and ozone. *J. Geophys. Res.*, **118**, 9658–9672.

Garney, H., M. Dameris, W. J. Randel, G. E. Bodeker, and R. Deckert, 2011: Dynamically forced increase of tropical upwelling in the lower stratosphere. *J. Atmos. Sci.*, **68**, 1214–1233.

Gerber, E. P., 2012: Stratospheric versus tropospheric control of the strength and structure of the brewer-dobson circulation. *J. Atmos. Sci.*, **69**, 2857–2877.

Gettelman, A. and P. M. d. F. Forster, 2002: A climatology of the tropical tropopause layer. *J. Met. Soc. Japan*, **80**, 911–924.

Gill, A. E., 1980: Some simple solutions for heat-induced tropical circulation. *Quart. J. Roy. Meteor. Soc.*, **106 (449)**, 447–462.

Grise, K. M. and D. W. J. Thompson, 2013: On the signatures of equatorial and extratropical wave forcing in tropical tropopause layer temperatures. *J. Atmos. Sci.*, **687**, 1084–1102.

Hegglin, M. and T. Shepherd, 2009: Large climate-induced changes in ultraviolet index and stratosphere-to-troposphere ozone flux. *Nat. Geosci.*, **2**, 687–691.

Hendon, H. H. and M. C. Wheeler, 2008: Some space-time spectral analyses of tropical convection and planetary-scale waves. *J. Atmos. Sci.*, **65 (9)**, 2936–2948.

Highwood, E. J. and B. J. Hoskins, 1998: The tropical tropopause. *Quart. J. Roy. Meteor. Soc.*, **124**, 1579–1604.

Holton, J. R. and A. Gettelman, 2001: Horizontal transport and the dehydration of the stratosphere. *Geophys. Res. Lett.*, **28**, 2799–2802.

Holton, J. R. and R. S. Lindzen, 1972: An updated theory for the quasi-biennial cycle of the tropical stratosphere. *J. Atmos. Sci.*, **29**, 1076–1080.

Houze, R. and A. Betts, 1981: Convection in gate. *Rev. Geophys.*, **19**, 541–576.

Huffman, G. J., et al., 2007: The TRMM multisatellite precipitation analysis (TMPA): Quasi-globa l, multiyear, combined-sensor precipitation estimates at fine scales. *J. Hydrometeor.*, **8**, 38–55.

Janowiak, J., P. Bauer, W. Wang, P. Arkin, and J. Gottschalck, 2010: An evaluation of precipitation forecasts from operational models and reanalyses including precipitation variations associated with MJO activity. *Mon. Wea. Rev.*, **138**, 4542–4560.

Janowiak, J., A. Gruber, C. Kondragunta, R. Livezey, and G. Huffman, 1998: A comparison of the NCEP-NCAR reanalysis precipitation and the GPCP rain gauge-satellite combined dataset with observational error considerations. *J. Climate*, **11**, 2960–2979.

Jensen, E. and L. Pfister, 2004: Transport and freeze-drying in the tropical tropopause layer. *J. Geophys. Res.*, **109 (D02207)**.

Jensen, E. J., L. Pfister, T.-P. Bui, P. Lawson, and D. Baumgardner, 2010: Ice nucleation and cloud microphysical properties in tropical tropopause layer cirrus. *Atmos. Chem. Phys.*, **10**, 1369–1384.

Jensen, E. J., et al., 2013: Ice nucleation and dehydration in the tropical tropopause layer. *PNAS*, **110 (6)**, 2041–2046.

Kalnay, E., et al., 1996: The NCEP/NCAR 40-year reanalysis project. *Bull. Amer. Meteor. Soc.*, **77**, 437–471.

Kanamitsu, M., W. Ebisuzaki, J. Woollen, S. Yang, J. Hnilo, M. Fiorino, and G. Potter, 2002: NCEP-DOE AMIP-II reanalysis (R-2). *Bull. Amer. Meteor. Soc.*, **83**, 1631–1643.

Kawatani, Y., S. Watanabe, K. Sato, T. J. Dunkerton, S. Miyahara, and M. Takahashi, 2010: The roles of equatorial trapped waves and internal inertia-gravity waves in driving the Quasi-Biennial oscillation. Part I: Zonal mean wave forcing. *J. Atmos. Sci.*, **67 (4)**, 963–980.

Kiladis, G., C. Thorncroft, and N. Hall, 2006: Three-dimensional structure and dynamics of african easterly waves. Part I: Observations. *J. Atmos. Sci.*, **63**, 2212–2230.

Kiladis, G., M. Wheeler, P. Haertel, K. Straub, and P. Roundy, 2009: Convectively coupled equatorial waves. *Rev. Geophys.*, **47**, RG2003.

Kim, J. and S.-W. Son, 2012: Tropical cold-point tropopause: Climatology, seasonal cycle, and intraseasonal variability derived from cosmic gps radio occultaion measurements. *J. Climate*, **25**, 5343–5360.

Kim, J.-E. and M. J. Alexander, 2013: A new wave scheme for trajectory simulations of stratospheric water vapor. *Geophys. Res. Lett.*, **40**, 5286–5290.

Kursinski, E. R., G. A. Hajj, J. T. Schofield, R. P. Linfield, and K. R. Hardy, 1997: Observing earth's atmosphere with radio occultation measurements using the global positioning system. *J. Geophys. Res.*, **102**, 23 429–23 465.

Levine, J. G., P. Braesicke, N. R. P. Harris, N. H. Savage, and J. A. Pyle, 2007: Pathways and timescales for troposphere-to-stratosphere transport via the tropical tropopause layer and their relevance for very short lived substances. *J. Geophys. Res.*, **112**, D04 308.

Lin, J., M. Lee, D. Kim, I. Kang, and D. Frierson, 2008: The impacts of convective parameterization and moisture triggering on AGCM-simulated convectively coupled equatorial waves. *J. Climate*, **21**, 883–909.

Lin, J., B. Mapes, M. Zhang, and M. Newman, 2004: Stratiform precipitation, vertical heating profiles, and the Madden–Julian oscillation. *J. Atmos. Sci.*, **61**, 296–309.

Lin, J.-L., et al., 2006: Tropical intraseasonal variability in 14 IPCC AR4 climate models. Part I: Convective signals. *J. Climate*, **19**, 2665–2690.

Lindzen, R. S. and J. R. Holton, 1968: A theory of the Quasi-Biennial Oscillation. *J. Atmos. Sci.*, **25**, 1095–1107.

Liu, Y. S., S. Fueglistaler, and P. H. Haynes, 2010: Advection-condensation paradigm for stratospheric water vapor. *J. Geophys. Res.*, **115**, D24 307.

Madden, R. A. and P. R. Julian, 1971: Detection of a 40-50 day oscillation in the zonal wind in the tropical Pacific. *J. Atmos. Sci.*, **28**, 702–708.

Madden, R. A. and P. R. Julian, 1972: Description of global-scale circulation cells in the tropics with a 40-50 day period. *J. Atmos. Sci.*, **29**, 1109–1123.

Matsuno, T., 1966: Quasi-geostrophic motions in the equatorial area. *J. Meteor. Soc. Japan*, **44**, 25–42.

Ortland, D. A. and M. J. Alexander, 2014: The residual-mean circulation in the tropical tropopause layer driven by tropical waves. *J. Atmos. Sci.*, **71**, 1305–1322.

Pfister, L., H. B. Selkirk, D. O. Starr, K. Rosenlof, and P. A. Newman, 2010: A meteorological overview of the tc4 mission. *J. Geophys. Res.*, **115**, D00J12.

Randel, W. J., 2010: *The Stratosphere: Dynamics, Transport and Chemistry.* Geophysical Monograph Series 190, American Geophysical Union,, 123-135 pp.

Randel, W. J., R. Garcia, and F. Wu, 2008: Dynamical balances and tropical stratospheric upwelling. *J. Atmos. Sci.*, **65**, 3584–3595.

Randel, W. J. and E. J. Jensen, 2013: Physical processes in the tropical tropopause layer and their roles in a changing climate. *Nat. Geosci.*, **6**, 169–176.

Randel, W. J., F. Wu, S. J. Oltmans, K. H. Rosenlof, and G. E. Nedoluha, 2004: Interannual changes of stratospheric water vapor and correlations with tropical tropopause temperatures. *J. Atmos. Sci.*, **61**, 2133–2148.

Randel, W. J., F. Wu, H. Vmel, G. E. Nedoluha, and P. Forster, 2006: Decrease in stratospheric water vapor after 2001: Links to changes in the tropical tropopause and the brewer-dobson circulation. *J. Geophys. Res.*, **111**, D12 312.

Ricciardulli, L. and P. D. Sardeshmukh, 2002: Local time- and space scales of organized tropical deep convection. *J. Climate*, **15**, 2775–2789.

Rienecker, M. M., et al., 2011: MERRA: NASA's Modern-Era Retrospective Analysis for Research and Applications. *J. Climate*, **24**, 3624–3648.

Roads, J., 2003: The NCEP-NCAR, NCEP-DOE, and TRMM tropical atmosphere hydrologic cycles. *J. Hydrometeor.*, **4**, 826–840.

Ruane, A. and J. Roads, 2007: 6-hour to 1-year variance of five global precipitation sets. *Earth Interactions*, **11(11)**, 1–29.

Ryu, J.-H., M. J. Alexander, and D. A. Ortland, 2011: Equatorial waves in the upper troposphere and lower stratosphere forced by latent heating estimated from trmm rain rates. *J. Atmos. Sci.*, **68**, 2321–2342.

Ryu, J.-H. and S. Lee, 2010: Effect of tropical waves on the tropical tropopause transition layer upwelling. *J. Atmos. Sci.*, **67**, 3130–3148.

Saha, S., et al., 2010: The NCEP climate forecast system reanalysis. *Bull. Amer. Meteor. Soc.*, **91**, 1015–1057.

Schoeberl, M. R. and A. E. Dessler, 2011: Dehydration of the stratosphere. *Atmos. Chem. Phys.*, **11**, 8433–8446.

Schoeberl, M. R., A. E. Dessler, and T. Wang, 2012: Simulation of stratospheric water vapor and trends using three reanalyses. *Atmos. Chem. Phys.*, **12**, 6475–6487.

Sherwood, S. C. and A. E. Dessler, 2000: On the control of stratospheric humidity. *Geophys. Res. Lett.*, **27**, 2513–2516.

Sinnhuber, B.-M. and I. Folkins, 2006: Estimating the contribution of bromoform to stratospheric bromine and its relation to dehydration in the tropical tropopause layer. *Atmos. Chem. Phys.*, **6**, 4755–4761.

Solomon, S., R. R. Garcia, F. S. Rowland, and D. J. Wuebles, 1986: On the depletion of antarctic ozone. *Nature*, **321**, 755–758.

Solomon, S., K. Rosenlof, R. Portmann, J. Daniel, S. Davis, T. Sanford, and G. Plattner, 2010: Contributions of stratospheric water vapor to decadal changes in the rate of global warming. *Science*, **327**, 1219–1223.

Spichtinger, P. and M. Krmer, 2012: Tropical tropopause ice clouds: a dynamic approach to the mystery of low crystal numbers. *Atmos. Chem. Phys.*, **12**, 28 109–28 153.

Stockwell, R. G., L. Mansinha, and R. P. Lowe, 1996: Localization of the complex spectrum: The s transform. *IEEE Trans. Signal Processing*, **44**, 998–1001.

Straub, K., P. Haertel, and G. Kiladis, 2010: An analysis of convectively coupled Kelvin waves in 20 WCRP CMIP3 global coupled climate models. *J. Climate*, **23**, 3031–3056.

Suzuki, T., Y. Takayabu, and S. Emori, 2006: Coupling mechanisms between equatorial waves and cumulus convection in an AGCM. *Dyn. Atmos. Oceans*, **42**, 81–106.

Takayabu, Y. N. and T. Nitta, 1993: 3-5 day-period disturbances coupled with convection over the tropical pacific ocean. *J. Meteor. Soc. Japan*, **71**, 221–246.

Tsuda, T., Y. Murayama, H. Wiryosumarto, S. W. B. Harijono, and S. Kato, 1994: Radiosonde observations of equatorial atmosphere dynamics over indonesia 2. characteristics of gravity waves. *J. Geophys. Res.*, **99**, 10 507–10 516.

Tulich, S. N., G. N. Kiladis, and A. Suzuki-Parker, 2011: onvectively coupled Kelvin and easterly waves in a regional climate simulation of the tropics. *Clim. Dyn.*, **36**, 185–203.

Ueyama, R., E. P. Gerber, J. M. Wallace, and D. M. W. Frierson, 2013: The role of high-latitude waves in the intraseasonal to seasonal variability of tropical upwelling in the brewer-dobson circulation. *J. Atmos. Sci.*, **70**, 1631–1648.

Wallace, J. M. and V. E. Kousky, 1968: Observational evidence of Kelvin waves in the tropical stratosphere. *J. Atmos. Sci.*, **25**, 900–907.

Wang, J., W. Wang, X. Fu, and K.-H. Seo, 2012: Tropical intraseasonal rainfall variability in the CFSR. *Clim. Dyn.*, **38**, 2191–2207.

Wang, W., P. Xie, S.-H. Yoo, Y. Xue, A. Kumar, and X. Wu, 2010: An assessment of the surface climate in the ncep climate forecast system reanalysis. *Clim. Dyn.*, **37**, 1601–1620.

Wheeler, M. and G. Kiladis, 1999: Convectively coupled equatorial waves: Analysis of clouds and temperature in the wavenumber-frequency domain. *J. Atmos. Sci.*, **56**, 374–399.

WMO, 2011: Scientific assessment of ozone depletion: 2010, global ozone research and monitoring project report 52. *World Meteorological Organization.*

Yanai, M. and T. Maruyama, 1966: Stratospheric wave disturbances propagating in the equatorial Pacific. *J. Meteor. Soc. Japan*, **44**, 291–294.

Zhang, C., 2005: Madden–Julian oscillation. *Rev. Geophys.*, **43 (RG2003)**.